DSE - Final Report

DREAM

M.D.C. Arons	4306511	S. Menon	4048997
R.W.E. van den Brink	4278895	J.E. Span	4279603
C.C.J. van Diën	4217667	M.N. Stavreva	4207823
T.R. Gritter	4208250	T. Steegman	4082532
T.A. Janssens	4002008	J.L. Westin	4283198
L.A. Lugtenborg	4195663		

Hovering Machine

Design Synthesis Excercise

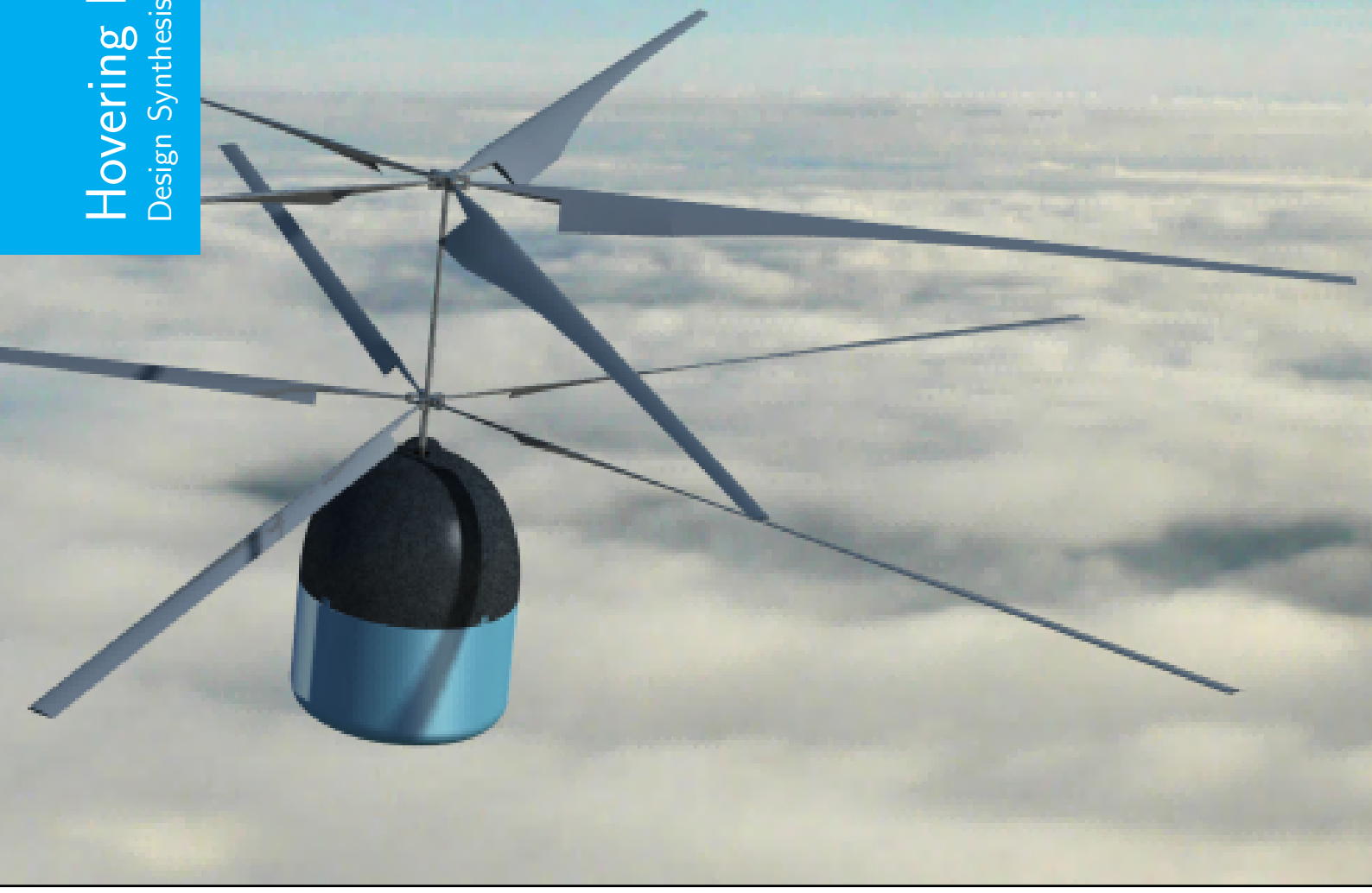

TU Delft Delft University of Technology

Aerospace Engineering

January 31, 2017

This page intentionally left blank.

Preface

This report is the final report of the Hover Team, which is a group of eleven Bachelor students at the faculty of Aerospace Engineering commissioned with designing a rotorcraft that can hover for a continuous period of 24 hours. Not only does the project test the technical knowledge and skills procured by the students during their study, but it also challenges the limits of technology and design, as no existing rotorcraft has been able to achieve this yet. This report will describe the steps taken and the process of designing the envisioned rotorcraft. The reports preceding this were the Mid-term Report, Baseline Report and Project Plan, where the project was defined, planned and some technical details were analysed.

We would like to thank our coaches Abishek K. Sahai and Wim Verhagen and our tutor Mark Voskuijl for all their support and guidance during the project. In addition, we would like to express our appreciation to Professor Rao and Ir. Verhagen who provided us with valuable information. Last but not least, we would like to thank all the committee members of the DSE for helping us with the organisational process and for providing the facilities.

The Hover Team
Delft, November 2016

Contents

List of Figures

List of Tables

List of Symbols and Abbreviations

List of Symbols

Roman

a_0	average blade flapping		$[rad]$
a_{1_s}	Longitudinal flapping		$[rad]$
A	Area		$[m^2]$
A_1	Lateral cyclic pitch		$[rad]$
A_2	Longitudinal cyclic pitch		$[rad]$
A_b	Blade Area		$[m^2]$
A_r	Rotor Disk Area		$[m^2]$
A_u	Upper Rotor Disk Area		$[m^2]$
$A_{l,in}$	Lower Rotor Area Inside of Wake		$[m^2]$
$A_{l,out}$	Lower Rotor Area Outside of Wake		$[m^2]$
b	Number of blades		$[-]$
b_{1_s}	Lateral flapping		$[rad]$
c	Chord length		$[m]$
C	Control input		$[-]$
c_d	Drag coefficient 2-dimensional		$[-]$
C_{D0}	Profile drag coefficient		$[-]$
C_{D0}	Horizontal rotor force coefficient		$[-]$
c_l	Lift coefficient 2-dimensional		$[-]$
C_{L_α}	Lift gradient		$[1/rad]$
c_m	Moment coefficient 2-dimensional		$[-]$
C_T	Thrust coefficient		$[-]$
ds	Length of cross section		$[m]$
d_{rotors}	Vertical distance between rotors		$[m]$
E	Young's modulus		$[N/m^2]$
e	Hinge offset		$[m]$
f	Equivalent flat plate area		$[m^2]$
F	Force		$[N]$
g	Gravitational acceleration		$[m/s^2]$
G	Centrifugal force		$[N]$
G	Shear modulus		$[Pa]$
H	H-force		$[N]$
h_m	Vertical c.g.-rotor separation		$[m]$
I	Area moment of inertia		$[m^4]$
I	Mass moment of inertia		$[kgm^2]$
J	Polar moment of inertia		$[m^4]$
J	Geometry Factor		$[-]$
k	Spring stiffness		$[N/m]$
k_o	Profile Power Factor	4.5	$[-]$
K_0	Overload Factor		$[-]$
K_s	Size Factor		$[-]$
K_m	Load Distribution Factor		$[-]$
K_0	Overload Factor		$[-]$
K_v	Dynamic Factor		$[-]$
k_p	Parasitic Power Factor	0.016	$[-]$
K	Induced velocity distortion factor		$[-]$
L	Length		$[m]$
m	Mass		$[kg$
$\dot{m}$	Mass flow		$[kg/s]$
M	Pitching moment		$[Nm]$
n_b	Number of blades		$[-]$

N	Number of teeth	$[-]$
N_T	Turbine Speed	$[rpm]$
N_{opt}	Turbine Speed at Continuous Power	$[rpm]$
P_e	Engine power	$[W]$
P_{hov}	Hover power	$[W]$
P_i	Induced Power	$[W]$
P_o	Profile Power	$[W]$
P_p	Parasitic Power	$[W]$
P_{tot}	Total Power	$[W]$
P_{opt}	Maximum Continuous Power	$[kW]$
Q	Torque	$[Nm]$
q	Shear Flow	$[N/m]$
q	Pitching rate	$[rad/s]$
R	Radius	$[m]$
R	Rolling moment	$[Nm]$
r	Radial position	$[m]$
r	Gear ratio	$[-]$
s	Eigenvalue	$[1/s]$
S	Shear force	$[N]$
SFC	Specific Fuel Consumption	$[kg/kW/hr]$
SPL	Sound Pressure Level	$[dB]$
t	Endurance	$[hr]$
t	Thickness	$[m]$
T	Thrust	$[N]$
T_{opt}	Torque at Continuous Power	$[N]$
T	Torque	$[Nm]$
U_P	Perpendicular velocity component	$[m/s]$
U_R	Radial velocity component	$[m/s]$
U_T	Tangential velocity component	$[m/s]$
V	Velocity	$[m/s]$
V_c	Climb Rate	$[m/s]$
v_i	Induced velocity	$[m/s]$
v_u	Induced velocity upper rotor	$[m/s]$
v_l	Induced velocity lower rotor	$[m/s]$
v_L	Local induced velocity	$[m/s]$
v_w	Airspeed below rotorcraft	$[m/s]$
V_f	Forward flight speed	$[m/s]$
V_T, V_{tip}	Tip Speed	$[m/s]$
w	Harmonic Motion	$[1/s]$
W	Weight	$[N]$
W_d	Design weight	$[N]$
W_e	Empty weight	$[N]$
$[x]$	Body-centered longitudinal position	$[m]$
$[X]$	Body-centered longitudinal force	$[N]$
$\dot{w}$	Fuel Flow	$[kg/s]$
z	Upward deflection of blade	$[m]$
$[z]$	Body-centered vertical position	$[m]$
$[Z]$	Body-centered vertical force	$[N]$

Greek

α	Angle of attack	$[rad]$
α_0	Angle of attack at zero lift	$[rad]$
α_s	shaft angle	$[rad]$
α_{TPP}	tip path angle	$[rad]$
α_i	Stiffening effect due to rotation	$[-]$
β	Pitch change angle	$[rad]$

β	Angle of mutation		$[rad]$
γ	Lock Number		$[-]$
θ	Blade pitch		$[rad]$
θ_0	collective pitch		$[rad]$
$\theta_{.75}$	Blade pitch at $0.75R$		$[rad]$
θ_1	Blade twist		$[rad]$
Θ	Angle of twist		$[rad]$
Θ	Helicopter pitch angle		$[rad]$
γ	Lock number		$[-]$
$\gamma_i\ (z)$	Assumed eigenmode of deflection		$[-]$
κ	Induced Power Factor	1.15	$[-]$
λ	Inflow ratio		$[-]$
μ	Advance ratio		$[-]$
ρ	Density		$[kg/m^3]$
σ	Solidity ratio		$[-]$
σ	Normal Stress		$[MPa]$
τ	Shear		$[MPa]$
τ_y	Shear Yield Strength		$[MPa]$
ϕ	Inflow angle		$[rad]$
χ	Skew angle		$[rad]$
ψ	Azimuth angle		$[rad]$
ω	Eigenfrequency		$[Hz]$
Ω	Rotational speed		$[rad/s]$

List of Abbreviations

AHS	American Helicopter Society
APU	Auxiliary Power Unit
BEMT	Blade Element Momentum Theory
BVI	Blade/Vortex Interaction
BWI	Blade-Wake Interaction
CFRP	Carbon Fiber Reinforced Polymer
c.g.	Center of Gravity
CTEF	Continuous Trailing Edge Flap
CVU	Control Variable Unit
DSE	Design Synthesis Exercise
DREAM	Dual-Rotor Endurance Air Machine
FAR	Federal Aviation Regulation
FBS	Functional Breakdown Structure
FEA	Finite Element Analysis
FFD	Functional Flow Diagram
HOGE	Hovering Out of Ground Effect
IBC	Individual Blade Control
IGE	In Ground Effect
MOI	Moment of Inertia
MTBF	Mean Time Between Failures
MTOW	Maximum Take Off Weight
NASA	National Aeronautics and Space Administration
NDARC	NASA Design and Analysis of Rotorcraft
OGE	OGE
PCVT	Pericyclic Continuously Variable Transmission
PMC	Pericyclic Motion Converter
RAMS	Reliability, Availability, Maintainability and Safety
RCM	Reaction Control Member
RPM	Rotations Per Minute

SFC	Specific Fuel Consumption
TRL	Technology Readiness Level
U.S.	United States
VTOL	Vertical Take Off and Landing

Abstract

The American Helicopter Society (AHS), has defined a competition for the concept design of a rotorcraft. As part of the Design Synthesis Exercise (DSE) in the Bachelors program at the Faculty of Aerospace Engineering, TUDelft has commissioned a group of students to take part in this competition. The objective of the competition is to design a rotorcraft capable of flying to pre-determined hover stations and performing hover out of ground effect for a cumulative time of 24 hours. This would involve the application of innovative concepts in the field of aerodynamics, propulsion, control and performance, whilst having a light-weight design.

The rotorcraft designed, named Dual Rotor Endurance Air Machine (DREAM), consists of a coaxial rotor to provide thrust capabilities. The power required for flight is delivered by a two spool turboshaft engine which includes a wave rotor device. Electric power is provided by an Auxiliary Power Unit (APU). The rotor speeds are adjusted using a Pericyclic Continuous Variable Transmission (PCVT). Complete control is provided by Continuous Trailing Edge Flaps (CTEF).

The coaxial rotor blades were designed using the VR-12 airfoil, with varying twist around the blades. Analysis on the blades were done to seek out the vibrational frequencies that need to be avoided during flight. The engine power is transmitted to the rotor with variable gear ratios ranging from $24:1$ to $3:1$. The forward flight phase is to be performed at a speed of 24 m/s which is optimized for low fuel consumption. The rotorcraft has a design empty weight to maximum takeoff weight ratio of 0.35.

The helicopter was designed to have a light weight structure in order to be able to meet the hover time specified. The fuel tank is one of the largest aspects of the design and is capable of carrying 3250 kg of fuel. The rest of the airframe is represented by a CFRP truss structure and steel hub and shaft system. The rotor's blades are also made out of composites and have a radius of 8 m.

The rotorcraft mission is to commence forward flight immediately after take-off. It will travel to the first and second hover stations after which, it will initiate hover at the final hover station. During long periods of hover, the thrust required by the rotorcraft will decrease, and to operate at the highest efficiencies, the rotor speeds can be reduced. The CTEF along with the transmission system can provide cyclic and collective pitch for increased controllability. In addition to this, the rotorcraft is designed to be operated fully autonomously.

1 Introduction

The American Helicopter Society (AHS) runs a yearly student design competition. The objective of the current challenge is to design a heavier-than-air unmanned flying machine that can endure 24 hours of hovering while carrying a payload of 80 kg. Moreover, the design should be able to be realistically developed, built and tested within the coming five years, and realise improvements on existing state of the art rotorcraft technology. Group four will present a design of such a hovering machine.

The purpose of this report is to present a coherent design, meeting the requirements of the baseline report, with the results from the trade-off done in the midterm report. This is done by finalising the last trade-offs left open previously. Having done this the various subsystems are designed, to finally verify and validate the calculations.

This report is divided in three separate parts, and is structured as follows: Part one consists of the mission definition, the functional analysis, and the operational analysis, being discussed in Chapters 2, 3 and 4, respectively. The second part consists of the subsystem design. Firstly, a short summary of the chosen concept is provided in Chapter 5. Following is the propulsion and power systems, which are discussed in Chapter 6. Chapter 7 expands on the aerodynamic properties of the rotors. The structural design is elaborated on in Chapter 8. Lastly the control and electrical systems are explained in Chapter 9. The third part of the report is made up of various analyses done on the final design. Firstly an overview of the final design is presented in Chapter 10, after which the various performance characteristics are analysed in Chapter 11. Chapter 12 describes the sensitivity analysis of the design, after which the compliance matrix and RAMS analysis are shown in Chapters 13 and 14 respectively. The DREAM is compared to an NDARC model in Chapter 15. The applicable sustainability present in the various systems are highlighted in Chapter 17. Lastly the conclusion and recommendations are expanded on in Chapters 18 and 19.

Design Functional Analysis

2 Project Definition

The top-level system requirements of the design are defined by the stakeholders' needs and the mission requirements stated in the project description. Thus, it is of great importance that they are recognised as the design is going to aim to satisfy their needs and requirements.

For the current design the stakeholders are represented by the American Helicopter Society that has posed the challenge. However, as the main goal of the challenge is to actually show improvement in existing technology, it is realised that further stakeholders are represented in all aviation institutes, organisations, companies and societies that are interested in rotorcraft. Next to this, as discussed in the Baseline Report[1], this kind of a machine would be beneficial for scientific research operations or political or social support missions that require staying for a long time observing.

The mission need statement describes the uniqueness of the design and defines the expectations of the stakeholders. The need for an improvement in current state of the art hovering endurance technology, while at the same time carrying a non-productive payload, is recognised as driving for the project.

> ***There is a need for an unmanned rotorcraft that demonstrates the greatest improvement in endurance compared to state of the art technology while carrying 80 kg of payload.***

Next to this, the project objective statement defines the constraints with respect to work force and development time limitations. It can be observed that a minimal hovering time is stated. However, the 24 hour challenge was identified as a killer requirement and the aim was to achieve a great improvement of the current maximal hovering time.

> ***Design a rotorcraft, within ten weeks with eleven students, that can hover for 24 hours carrying a payload of 80 kg and can be built within five years.***

3 Functional Analysis

In the current chapter the functional characteristics of the design are going to be discussed. Firstly, Section 3.1 shows an updated version of the functional flow diagram, which is followed by the functional breakdown structure discussed in Section 3.2.

3.1. Functional Flow Diagram

The functional flow diagram (FFD) is one of the available tools for providing insight in the technical requirements of a product. This diagram specifies the flow of functions needed to ensure customer's satisfaction. The flow diagram is divided in the product's main functions and its different subsystems and can therefore be used to check if the designed subsystems comply with the stated requirements. The main functions of the flow diagram are roughly based on the hovering device's mission profile. The subsystems define the functions the product should complete, or in other words the problem to be solved, in order to finish the mission and satisfy the customer.

The functional flow diagram presented in Figures 3.1a to 3.1c is an updated version. The original was presented in the Baseline Report, essential changes are highlighted[1]. The updates in the FFD and funtional breakdown structure (FBS), presented in Section 3.2, mainly consist of an increase of the level of detail of the predefined functions with the knowledge gained during the project.

In Figure 3.1a, the increased detail is in the addition of previously forgotten functions. These are testing control surfaces (1.2.3), checking the battery (1.4.2) and the inclusion of an extra level for increasing thrust (2.1). In Figure 3.1b the level of detail is increased and several functions are redefined. The first sublevel is reordered to be more logical and one of its original function renamed and replaced to the navigation function (3.1.1.1). Furthermore function 3.1 has further redefined subfunctions. The sole update in Figure 3.1c is the addition of the control rotations per minute (RPM) function (4.3) with its newly defined subfunctions. This addition is quite important since one of the possible factors for highly increased endurance is due to the more efficient flight achieved by actively controlling RPM.

3.2. Functional Breakdown Structure

A functional breakdown structure is another useful tool for determining a product's technical requirements. A product's main function is broken down into sub-functions, each of which is in turn broken down into lower-level functions. Figure 3.2 shows the updated functional breakdown of the hovering device.

The functional breakdown structure is hierarchical, meaning that high-level functions are dependent on low-level technical functions. The first level of subfunctions is again loosely based on the hovering device's mission profile. The FBS and FFD are related trough their top and sublevel functions, with clear reference between the diagrams. The update of the FBS strongly correlates to that of the FDD described in Section 3.1, with the main highlights being the addition of the navigation (in 3.1) and the control RPM function (4.3). Furthermore the level of detail is increased in the sensor check (1.3), engine check (1.4) and increase thrust function (2.1).

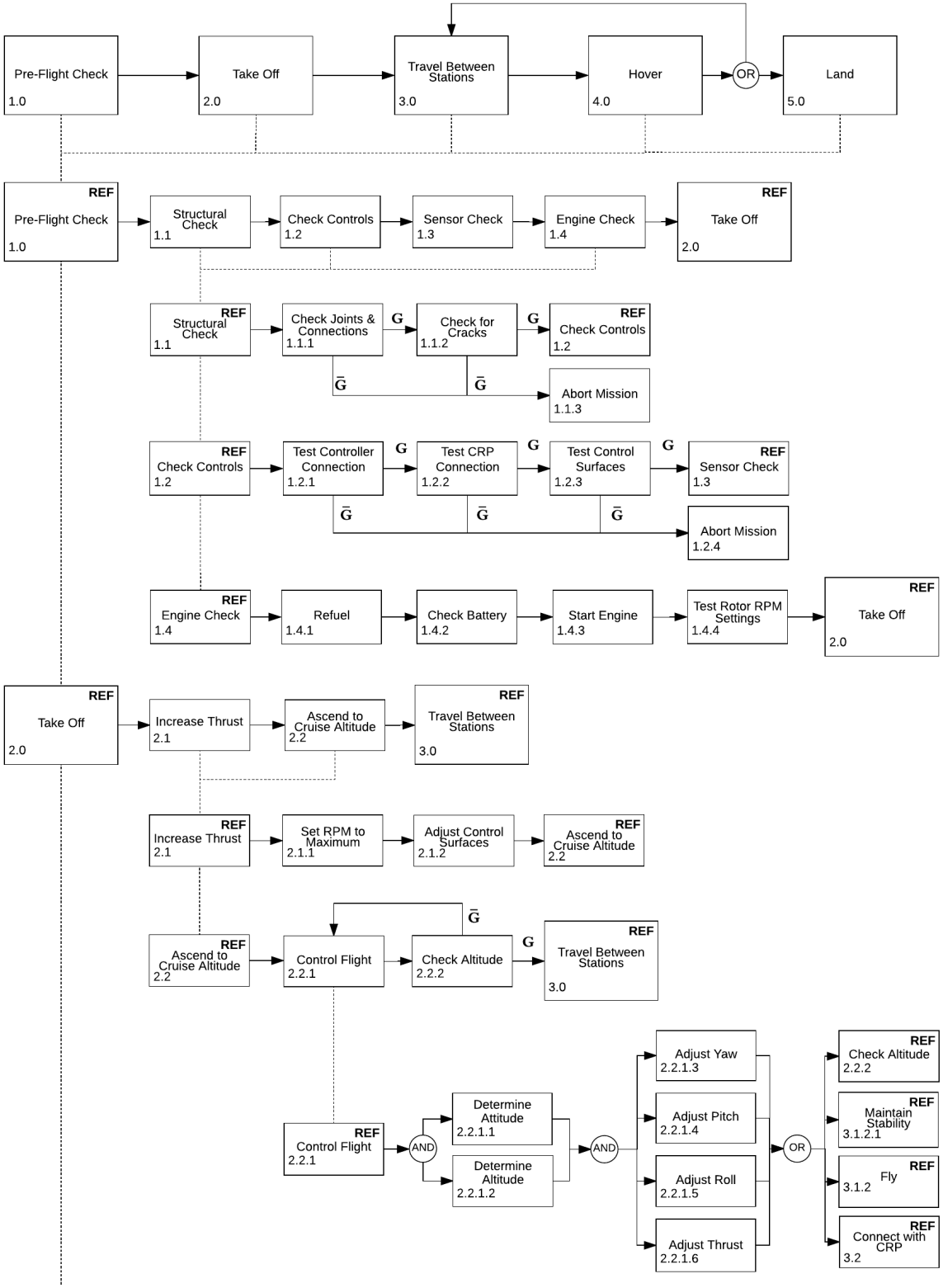

(a)

Figure 3.1: Functional flow diagram I

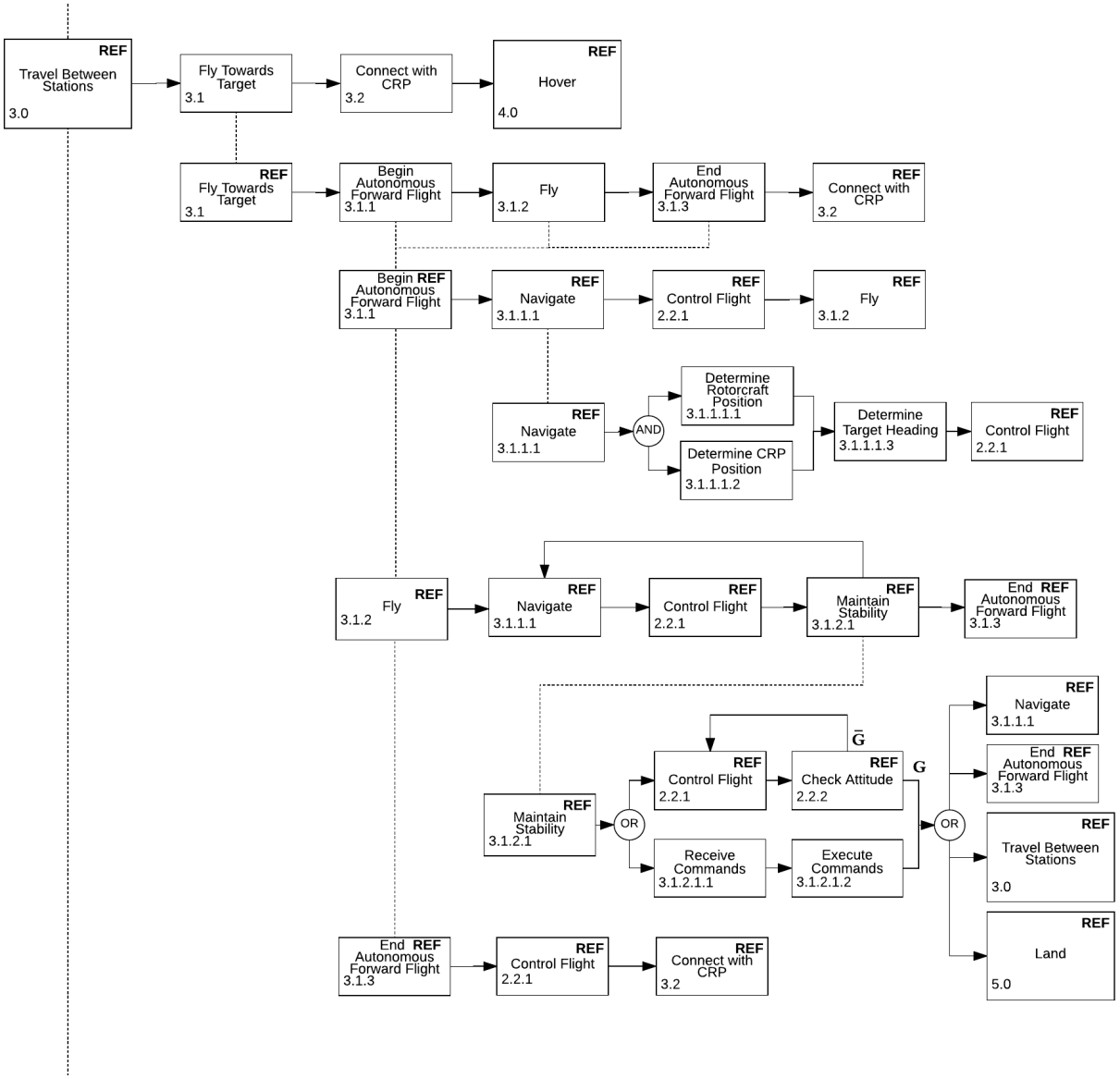

(b)

Figure 3.1: Functional flow diagram II

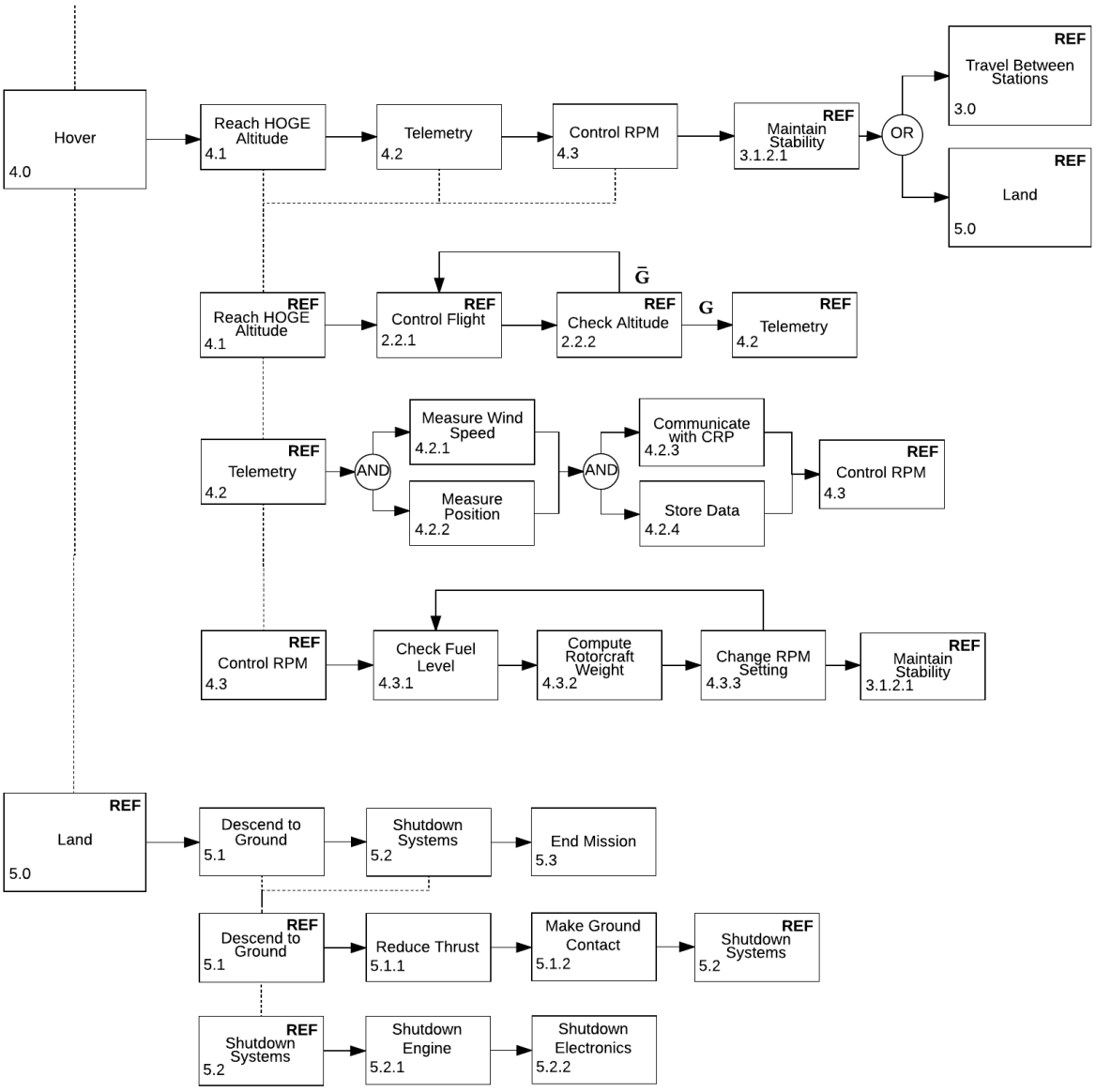

(c)

Figure 3.1: Functional flow diagram III

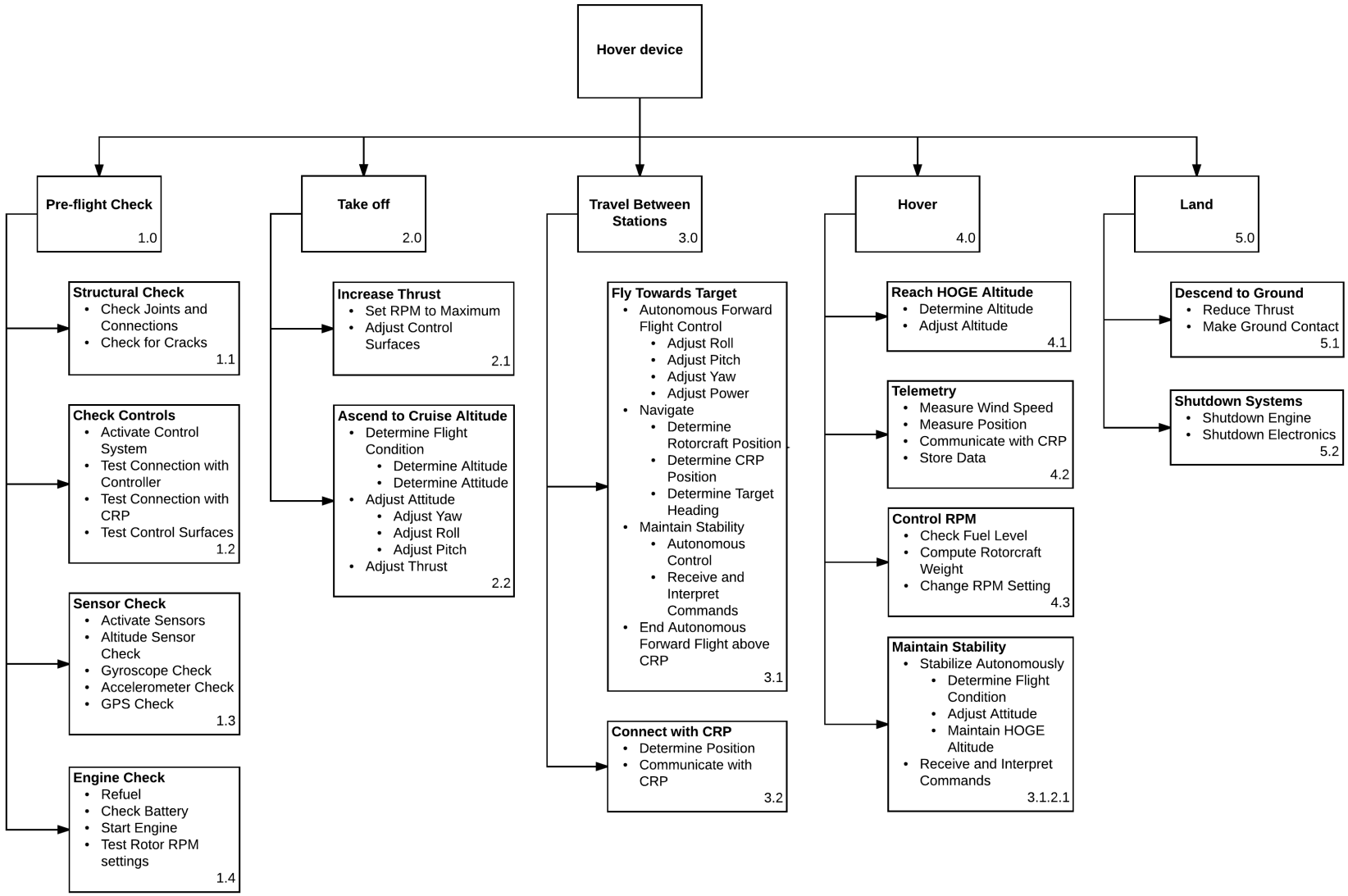

Figure 3.2: Functional breakdown structure

4 Operational Analysis

The present chapter discusses the operational performance of the design. Firstly, the market analysis will be discussed in Section 4.1, which is then followed by a short operations and logistics elaboration in Section 4.2.

4.1. Market Analysis

In order to perform a valuable market analysis, firstly the stakeholders need to be identified. As mentioned in Chapter 2, the main stakeholder is the one who poses the need of creating such a design: the American Helicopter Society. However, it is recognised that, as it is expected to achieve an improvement in current technology, additional stakeholders in all aviation organisations and companies are going to be affected by the development of such a design. Moreover, the TU Delft, the supervising professors and the students involved in the process are also interested in the success of the design.

Looking at the current research and development programs, one can observe that most are focused on improving speed and decreasing noise. The U.S. Army has implemented efforts in finding programs that develop high-speed rotorcraft designs. The two to be further supported are from the Bell Helicopter and Sikorsky/Boeing teams which are tasked with building prototypes whose test flights are expected to start as early as in 2017. Their aim is to provide for replacement possibilities for the long-serving Sikorsky UH-60 Black Hawk and Boeing AH-64E Apache[1]. Next to this, NASA's project "Get SMART" aims for reductions in noise and vibrations, which will make routine transportation of people by rotorcraft within short distances possible. This is believed to be beneficial for relieving the air traffic congestion appearing at the U.S. airports[2].

When looking at the design of DREAM, there are unique features of the the design that are expected to improve the operating costs with respect to currently existing rotorcraft. The design features include a wave rotor, an innovative transmission system, continuous trailing edge flaps and rotor blades optimised for hover. Figure 4.1 provides a comparison of the financial savings that can be made by implementing these designs. The two variable costs considered were the fuel consumption cost and the environmental cost due to CO2 emissions. The fuel costs were estimated with a base price of 56.2 *cents* per kilogram of fuel[3]. It is also known that for every kilogram of fuel used, 3.15 kg of carbon dioxide is produced as emissions[4]. Based on this, the financial impact could be estimated[5].

Furthermore, the financial impact of the CTEF's can be estimated as well. The purpose of the CTEF is to replace the role of the conventional swash plate control mechanism. These can be heavy and expensive. A swash plate system for a coaxial design would cost approximately $ 8530[2]. In comparison, piezoelectric material required for the control surfaces are estimated to cost $ 7200 with the added benefit of lowering overall structural weight[6].

[1] URL www.news.usni.org/2014/10/03/u-s-army-selects-bell-sikorskyboeing-build-prototypes-next-generation-helicopter-program [cited 23 November 2016]
[2] URL www.nasa.gov/topics/aeronautics/features/smart_rotor.html [cited 23 November 2016]
[3] URL http://www.flightdeckfriend.com/how-much-does-jet-fuel-cost [cited 31 January 2017]
[4] URL https://www.iata.org/whatwedo/environment/Documents/carbon-offset-program-faq-airline-participants.pdf [cited 30 January 2017]
[5] URL http://news.stanford.edu/2015/01/12/emissions-social-costs-011215/ [cited 31 January 2017]
[6] http://www.piezo.com/orderpricelist.html [cited 31 January 2017]

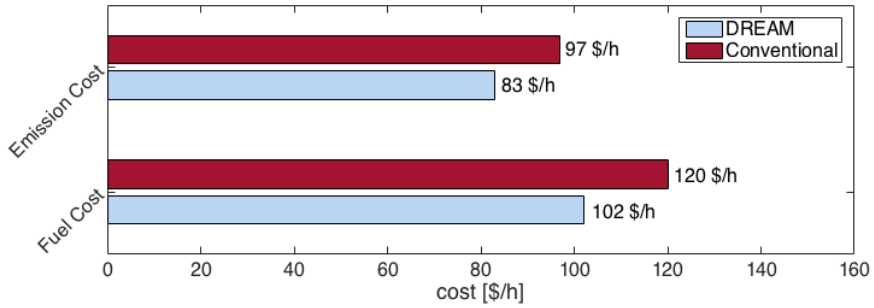

Figure 4.1: Variable costs in comparison to existing rotorcraft

Additionally, as stated by the study of Changa et. co[3] from 2015, hovering can be used for scientific research, such as aerial air sampling, where the inability of vertical movement and hovering causes a big drawback even if light aircraft with engines that can transport large payload and achieve greater range result in higher research capabilities. This, as many other scientific researches, will highly benefit from an unmanned machine that has high endurance and can take samples or images of a specific region over a large time frame, which will provide for a clear overview of the different natural processes.

Next to this, rotorcraft are needed in defence actions during military actions or protection of national borders. For example, already in 2009, the British government spotted that the lack of air force, in the face of helicopters, was undermining the country's force capabilities and troop protection during the operations in Afghanistan[7].

4.2. Operations and Logistics

The mission description is provided by the project definition and is presented in Figure 4.2. It can be seen that the mission is highly specific. The rotorcraft should be able to take off, move between and hover over three different stations, and finally land.

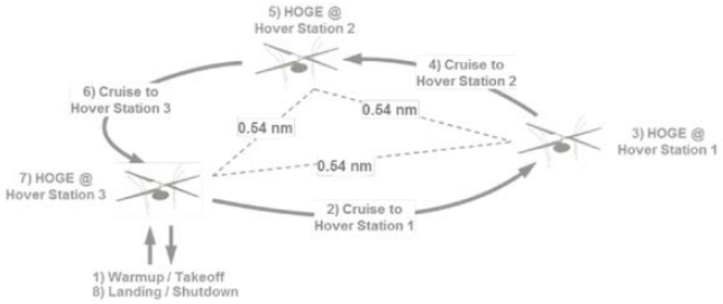

Figure 4.2: Mission description[4]

Figure 4.3 represents the operations and logistics diagram. It can be observed that it resembles the functional flow diagram and it does not take into account certification and maintenance processes. As the current design is aiming for participation in the AHS competition and since the design is not expected to be commercialised, elements like the machine lifetime are not considered. The start of the operations is the end of the manufacturing process. This is followed by preparation for the competition and is performed on the ground by the design team. It can be noted that a few repair slots have been allocated in case any structural or system issues occur. If they are not severe, they could swiftly be performed by the maintenance team, or in parallel with other operations, which is the reason the repair is planned

[7] URL www.news.bbc.co.uk/2/hi/uk_news/politics/8153129.stm [cited 23 November 2016]

on a separate level. The AHS inspection is needed so that the prototype is approved and it is checked that it fulfils all the requirements and meets all the limitations. It should be noted that the control of the rotorcraft will be autonomous with a possibility for overruling the autopilot from the ground. Moreover, as hovering is going to take up most of the time of the mission, it has been given a bigger part of the diagram. A few iterations over some of the functions are going to be required and those relations are also illustrated. Finally, the dashed arrow marks the possibility of having following flights after the competition.

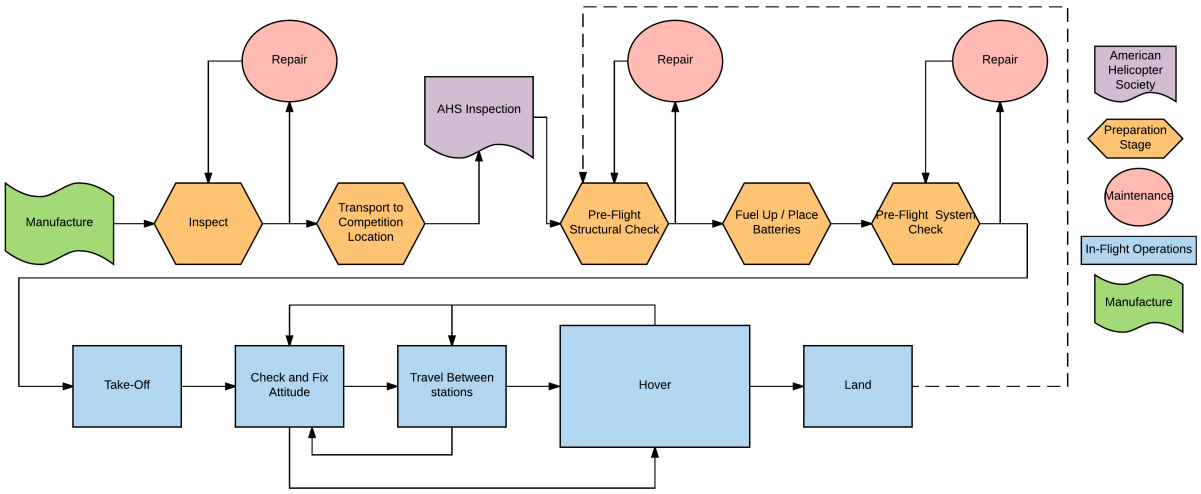

Figure 4.3: Operations and logistics diagram

Subsystem Design

5 Final Concept

This chapter summarises the method for selecting the final concept design performed in the Midterm Report[5]. The different analysed concept configurations are explained in Section 5.1 and the propulsion system selection in Section 5.2. The final concept layout is illustrated in Section 5.3. Last but not least, a brief presentation of the physical characteristics of the final design as well as a short introduction to the implemented technologies and improvements in a subsystem level are discussed in Section 5.4.

5.1. Concept Configurations

From the mission definition, project objective and the designs functional analysis, requirements have been defined and a rotorcraft concept needs to be selected to comply with the requirements and perform the mission. In the Midterm Report a design option tree has been generated to aid the selection of multiple rotorcraft concepts with different subsystems[5]. It was decided that the main concept design drivers were the rotorcraft configuration and propulsion system, which will be discussed in Section 5.2.

For the rotorcraft configuration four different options were considered for the final design. These were a single rotor with anti torque fins, tandem, coaxial and quadcopter configuration. These configurations were analysed and advantages and disadvantages were listed. This was followed by a trade-off and a final top level comparison to pick a final configuration which is presented in Section 5.3.

5.2. Propulsion System

In order to be able to compare the different propulsion system options, it was aimed that each of the concepts featured a different propulsion unit. This made possible that a comparison between their effect on the distinctive designs can be performed.

For the propulsion system, the following layouts were considered. The single rotor design made use of a conventional turboshaft configuration with drivetrain, while the tandem opted for a Wankel engine. Both the coaxial and quadcopter configurations were designed to use hydrogen. For the coaxial helicopter a hybrid system was used whereas the quadcopter used hydrogen as its main propulsion system.

5.3. Final Concept Selection

The original trade-off showed that the coaxial and tandem configuration were the most feasible solutions while a top level comparison gave the coaxial as the best design. The main reasons were the higher efficiency due to the twin rotor configuration and elimination of the need for an anti torque device. Furthermore the concept is flight proven and has a low structural weight.

As for the propulsion system hydrogen was deemed to be an unfeasible option for this specific mission and for the energy source it was decided to use jet fuel of similar products, depending on the engine requirements. The engine trade-off showed that a turboshaft achieved the highest overall performance.

Thus the final concept design includes a coaxial rotor configuration powered by a turboshaft with jet fuel as its energy source. This preliminary design will serve as a basis for the detailed subsystem design performed in this project phase.

5.4. Parameters and Systems of Final Design

In the current section a brief overview of the final design is going to be presented. Firstly, Table 5.1 lists number of physical parameters of the rotorcraft. This will be followed by a short discussion of the innovative solutions, which have been implemented in the design.

For further analysis and more detailed information on the subsystems, please refer to the corresponding chapter. For a more detailed overview of the design, including technical drawings and 3D renderings, please refer to Chapter 10, where also the imposed risks are discussed.

Weight $[kg]$		*Engines*	
Empty	1752.4	Type	*Rolls Royce Gem* $42-1$ $MK.204$
Maximum takeoff	5000	Number	1
Fuel capacity	3247.6	Maximum rated power	746 kW
		Maximum continuous power	690 kW
Rotor Parameters		*Upper Rotor*	*Lower Rotor*
Radius $[m]$	R	8	8
Chord $[m]$	c	$0.5-0.1$	0.2
Twist $[deg]$	θ	$45-12$	$32.5-12$
Solidity	σ	0.041	0.035
Tip speed $[m/sec]$	ΩR	$140.2-83.4$	$140.2-83.4$
Airfoil type		*Boeing Vertol* $VR-12$	*Boeing Vertol* $VR-12$
Main Dimensions $[m]$			
Fuel tank radius	R	2.01	
Fuselage height	h	2.34	
Total rotorcraft height	H	4.76	
Rotors separation		2	

Table 5.1: Physical Parameters

Power and Propulsion Solutions

In order to achieve as high as possible hover endurance, the power and propulsion department has implemented a transmission technology, which can continuously decrease the RPM in order to minimise excess power provided by the engine. Furthermore, the implementation of a wave rotor benefits for a lower SFC of $8-12\%$ compare to the engine performance without the wave rotor implemented.

Aerodynamics Solutions

By implementing a hyperbolic variation in twist and taper along the chord, the blade has been optimised for best hover performance. This also resulted in a 20% more efficient blade design.

Structures Solutions

Due to the fact that the rotorcraft is unoccupied and there are no safety restrictions regarding landing loads, it was realised that a dedicated landing gear is not required. Thus, the fuel tank has been design in such a way that it can cope with the high loada during landing.

Control Solutions

For controlling the rotorcraft, continuous trailing edge flaps (CTEF) have been implemented. Their main advantage is the fact that no mechanical components and hinges in the rotating system are required, which results in lower drag. Additionally, they lead to lower noise and vibrations, which ameliorates the performance while at the same time ensure complete control of the system.

6 Propulsion and Power

This chapter describes the design process of the propulsion subsystems. Section 6.1 elaborates on the engine characteristics and the auxiliary power. This is followed by Section 6.2 where the transmission design is presented. Section 6.3 provides an overview of the final results.

The propulsion subsystems consist of a turboshaft engine, a wave rotor incorporated into the engine, continuously variable transmission module and an Auxiliary Power Unit(APU). In the conceptual design phase, it was decided that the final design would use the Rolls Royce Gem 42-1 MK.204 engine, which has a maximum power output of 746 kW. In addition to this, a Solar T62-32 APU will be used to provide complete auxiliary power.

6.1. Engine Characteristics and Auxiliary Power

The engine is required to provide sufficient power to the coaxial rotor. In order to understand the power available and to size the transmission system accordingly, engine performance characteristics at off design point need to be modelled accurately. In order to do this, various scientific papers were used to simulate the characteristics and a gas turbine simulation program was used to verify the calculations.

Some key assumptions made during the analysis and calculations were that the modelling of the engine was done for constant ambient temperatures and pressures. This means standard ISA conditions were used. The intake airflow was considered to be accelerated from a stationary initial velocity. The engine design point characteristics are provided in Table 6.1[8,9].

Table 6.1: Engine design characteristics

Max. Rated Power	Max. Continuous Power	Rated SFC	Turbine Speed	Airflow	Weight
746 kW	690 kW	0.298 $kg/kw-hr$	6165 rpm	5.9 kg/s	184 kg

It needs to be noted that an overrunning clutch is used to detach the transmission system from the turboshaft engine in the case of an engine failure. This allows the rotorcraft to use autorotation in order to land safely.

6.1.1. Wave Rotor

The wave rotor consists of a rotor with air passages that rotate, channelling air through a drum. The air is channelled into the rotor by the use of ducts. The air is brought in from the compressor and compressed to higher pressures and temperatures within the wave rotor by utilising the waves generated inside the device. This high pressure air is fed into the combustion chamber and is heated. The heated air-fuel mixture is then brought back in to the wave rotor, where it expands to a lower pressure and temperature. It is then fed into the engine turbine. The combustion process occurs at higher pressures and temperatures which results in higher specific power and lower specific fuel consumption.

The wave rotor would need to be designed using complex computational fluid dynamics methods and is beyond the scope of this project. Hence, an existing design used on the Allison 250-C30 engine will be

[8] URL www.jet-engine.net/miltsspec.html [cited 24 January 2017]
[9] URL www.turbokart.com/about_rollsgem.htm [cited 24 January 2017]

implemented. This is a four port system where a portion of the total airflow in the engine is redirected to the wave rotor[6]. The design of the wave rotor and its placement within the engine is shown in Figures 6.1 and 6.2.

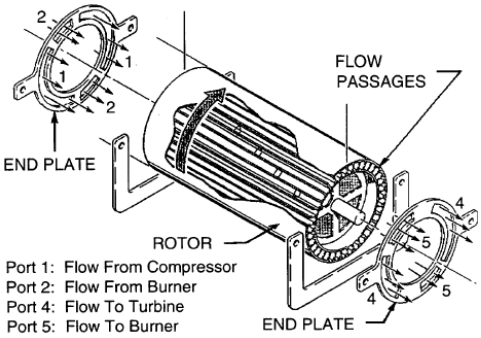

Figure 6.1: Chosen wave rotor design[6]

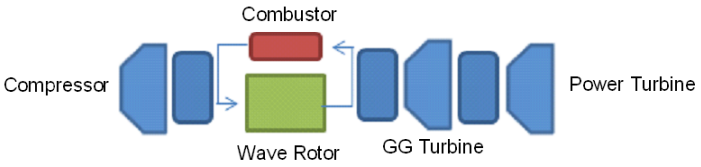

Figure 6.2: Placement of the wave rotor

In order to model the effects of the wave rotor for a different engine, the increase in pressures were analysed and the resulting change in sfc's were approximated[6]. These effects are described in Section 6.1.3. The dimensions of the wave rotor concept are provided in Table 6.2. The weight of the wave rotor was also estimated using reference papers[7].

Table 6.2: Design features of the wave rotor[6]

Inlet Area	Mean Diameter	Rotor Length	Mass Flow	Weight
0.00277 m^2	0.1631 m	0.1524 m	2.19 kg/s	40 kg

6.1.2. Turbine Speed Variation

One of the key issues to address in the design characteristics of the engine, is the ability to model the turbine speeds at different power settings. In order to do that, Equation 6.1 can be used[8].

$$\frac{P_T}{P_{opt}} = 2 \cdot \frac{N_T}{N_{opt}} - \left(\frac{N_T}{N_{opt}}\right)^2 \tag{6.1}$$

This equation can be rearranged to determine the turbine speeds for varying power levels and is provided by Equation 6.2

$$\frac{N_T}{N_{opt}} = 1 - \sqrt{1 - \frac{P_T}{P_{opt}}} \tag{6.2}$$

The ratio $\frac{N_T}{N_{opt}}$ is the ratio of the speed of the turbine based on the optimal operating speed of the engine. The results of the varying turbine speeds were calculated and verified by using data from NDARC calculations for a similar power output turboshaft engine[9]. This is shown in Figure 6.3.

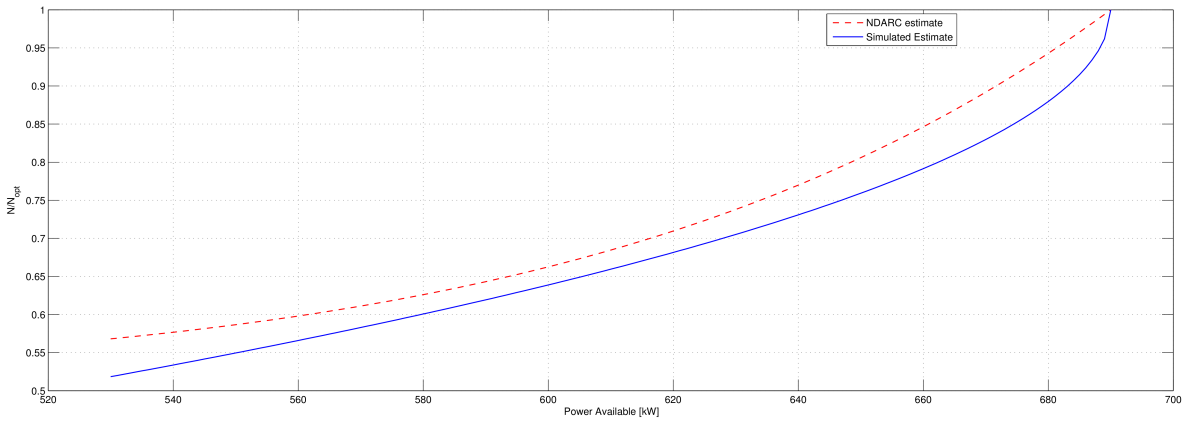

Figure 6.3: Turbine speed ratios vs power available

As it can be seen, the turbine speeds drop as the power available is decreased. This is one of the characteristics of the engine when operating away from the design point. Knowing this aspect of the engine is essential in the design of the drivetrain system which will be explained in Section 6.2. When comparing the results of the simulation, to the data provided by NDARC, it can be seen that there is a slight deviation. The maximum deviation is seven percent which shows that the equation used to model the rotational speeds of the turbine of the chosen turboshaft is accurate.

6.1.3. Fuel Flows and Specific Fuel Consumption (SFC)

The next step is to model the specific fuel consumptions and fuel flows with respect to the power delivered by the engine. The addition of the wave rotor has a direct influence on the fuel consumption. The SFC was modelled by using existing data on wave rotors used for turboshaft engines[6][7]. The performance of the wave rotor theoretically, is better at off design points for the turboshaft engine. Using the relationship between the respective Pressure Ratios provided by the chosen wave rotor[6], as well as implementing data from NDARC for fuel flows, it was possible to extrapolate data for the variation in SFC to the Power delivered for the Rolls Royce Gem. The behaviour of the SFCs are provided in Figure 6.4 and SFC is modelled in NDARC by rearranging Equation 6.3[9].

$$\dot{w} = SFC \cdot PowerAvailable \tag{6.3}$$

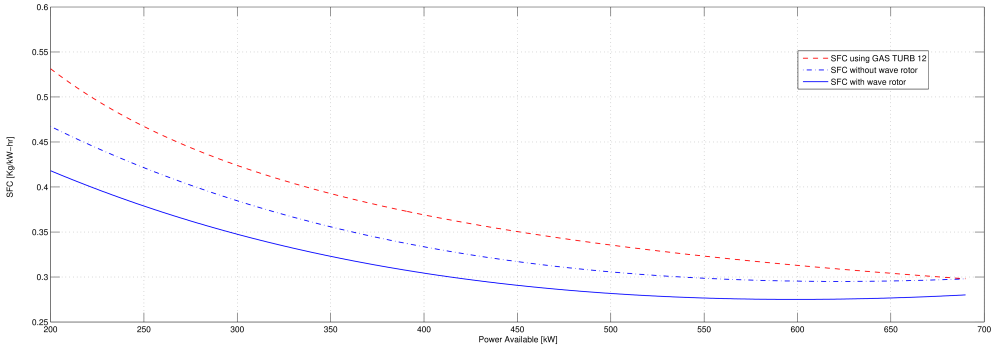

Figure 6.4: SFCs vs power available

The results obtained were verified using the gas turbine simulation program - GasTurb12 for a similar turboshaft engine[10]. The first curve represents the estimated SFC according to GasTurb12, whereas the second curve is representative of the SFC under the same conditions that the verification software is modelled for. The third curve shows the effects on the SFC with the addition of a wave rotor. It should be noted,that the wave rotor decreases the SFC by up to twelve percent for the same power rating. The effects are much more prominent for lower powers. Once this is done, the fuel flows with the wave rotor addition are determined using Equation 6.3.

The fuel flows are plotted against the available power and verified to check the accuracy, in Figure 6.5.

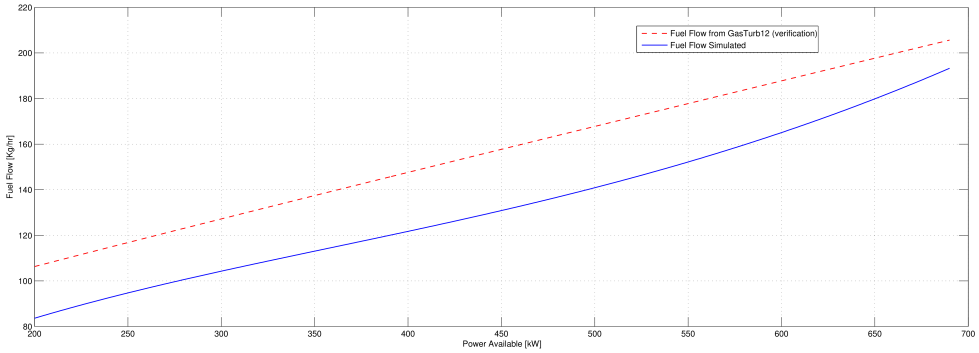

Figure 6.5: Fuel Flow vs Power Available

The addition of the wave rotor decreases the fuel consumption by approximately 9%.

6.1.4. Torques

The torques generated by the engine were modelled using Equations 6.4 and 6.5, where power is defined in kW and engine speed in rev/min[8]. The maximum torque generated by the engine is $2,170\ Nm$ at stall speed[11]. The stall speed that relates to this torque is the minimum engine speed at which the engine is able to transfer the power to the transmission.

$$\frac{T}{T_{opt}} = 2 - \frac{N_T}{N_{opt}} \tag{6.4}$$

$$T_{opt} = 9549.3 \cdot \frac{P_{opt}}{N_{opt}} \tag{6.5}$$

The variation in torque to the change in turbine speed is provided in Figure 6.6.

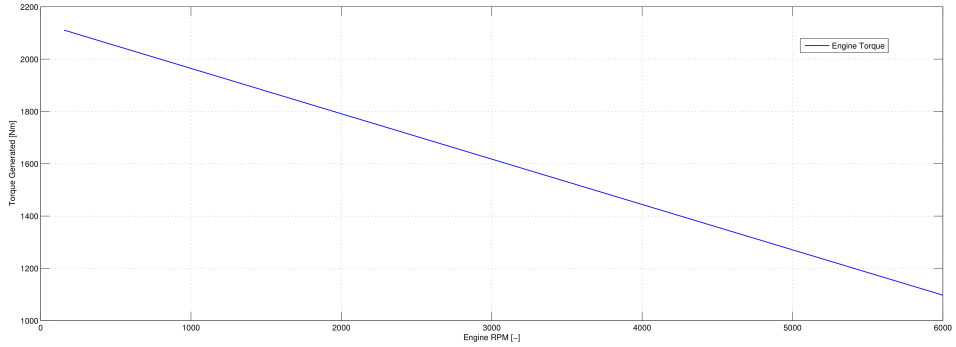

Figure 6.6: Torque generated for varying engine speed

[10] URL www.gasturb.de/the-program.html [cited 24 January 2017]
[11] URL www.turbokart.com/about/_rollsgem.htm [cited 24 January 2017]

6.1.5. Auxiliary Power Unit (APU)

The APU chosen is the Solar T62-32 which provides a maximum power output of 120 kW[12]. This APU will generate the required electrical power for all the subsystems in the rotorcraft and provide the startup for the main engine. The APU will however be initiated on ground and will be fully operational on its own during the mission. This unit will also be providing full power for the main gearbox for variable transmission. The APU is expected to be operating at different power levels, but is modelled to be operating at its continuous power output. The fuel flow for the APU is added for the calculation of the total endurance.

6.2. Transmission Design

In order to design the transmission, it is important to know the forces that act on the components of the drivetrain. The driving force on the drivetrain is the torque due to the rotational velocity of the engine shaft. This velocity is transferred from the engine to the rotors, which make sure that the rotorcraft stays in the air. However, the output rotational velocity of the engine is much bigger than that of the rotors. Therefore, gears are needed to lower the RPM to the appropriate rotor RPM. As can be seen from Equation 6.5, this can cause the torque to increase depending on the gear ratio used. The gear ratio is defined as the ratio between the input rotational velocity and output rotational velocity of a gear and is dependent on the number of teeth on the running and mating gears. This is shown in mathematical form in Equation 6.6.

$$\frac{\Omega_1}{\Omega_2} = r = \frac{N_2}{N_1} \tag{6.6}$$

Here, Ω_1 and Ω_2 are the input rotational velocity and output rotational velocity in RPM, respectively. r is the gear ratio and N_1 and N_2 are the number of teeth of the running and the mating gear, respectively.

Before the torques on the remaining shafts can be calculated, the amount of gears, their type and gear ratio and the transmission architecture have to be determined.

Since the rotorcraft has a coaxial configuration, with two contra-rotating rotors, a gear has to be found which is able to transfer the rotation of one shaft to the two contra-rotating rotor shafts. This can be done by using a bevel gear, which is connected to two mating bevel gears on opposite sides of the running gear. This can be seen in the upper right corner of Figure 6.7. The running gear is the gear that is connected to the input shaft of the gear and the mating gear is the gear that is connected to the output shaft of the gear.

The centre of gravity of the rotorcraft is preferred to be as close to the centre as possible. To achieve this, the turboshaft engine has to lie somewhat under the main rotor shaft. Considering that the input shaft to the first set of bevel gears has to be horizontal, it has been determined that three sets of bevel gears will be used. The first two sets, are simply used to alter the direction of the transmission system and do not serve to increase the gear ratio.

Due to the high endurance of the rotorcraft, the initial and final weights will have a considerable difference. In view of this, a gearbox is needed to ensure that the engine will be able to sustain continuous hover during the entire mission duration. Taking these requirements into account, the following configuration was decided upon:

[12] URL http://www.tamaaero.com/t62-solar-engine.html [cited 24 January 2017]

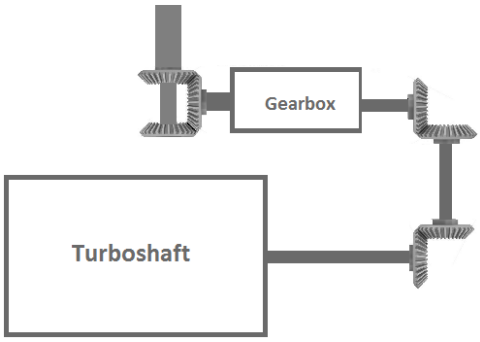

Figure 6.7: Layout of the drivetrain

6.2.1. Gear Design

Now that the drive-train layout is clear, it is time to take a look at the gears. As torque increases when RPM decreases, it is optimal for the first two bevel gears to have a gear ratio of one. The reasoning was to have speed reduction towards the end of the transmission system to save weight. This kind of bevel gear is also referred to as Miter gear. The total gear ratio will primarily be achieved by the gearbox with a little help from the bevel gear that causes the counter-rotation. The design of the gearbox will be treated in Subsection 6.2.2.

For the sizing of the bevel gears, Equation 6.7 is used[13]. Here, D is the pitch diameter of the gear in m, N is the number of teeth of the running gear, F is the face width of the gear, σ is the tensile yield strength of the material and J is a geometry factor that depends on the number of teeth on the running and the mating gears.

$$D = \sqrt{\frac{2 \cdot T \cdot N}{\sigma \cdot F \cdot J}} \tag{6.7}$$

The mating gears of the Miter gears will encounter less torque, because the power is lower, due to the efficiency of the gear. However, for safety and simplicity, the gears of the two Miter gears will be assumed to have the same size. In order to size it, an optimal combination for face width and pitch diameter of the gears had to be found. To this end, the mass of the gear was calculated using Equation 6.8. Here, the gear is modelled as a cylinder with diameter D and length F and ρ is the density of the material.

$$m = \frac{\pi \cdot D^2 \cdot F \cdot \rho}{4} \tag{6.8}$$

It turned out that the mass would be optimised for an infinitely small face width and an infinitely big pitch diameter. However, straight bevel gears or miter gears, are constrained by the pitch line velocity they experience. With this in mind, the minimum diameter to adhere to this constraint was determined using Equation 6.9[10].

$$D = 0.3048 \cdot \frac{V}{0.262 \cdot \Omega} \tag{6.9}$$

Here, V is the maximum pitch line velocity in ft/min and equal to $1,000$ ft/min.The maximum diameter was calculated to be 0.184 m, which applies to the first set of Miter gears. Another design parameter

[13] URL web.mit.edu [cited 19 January 2017]

for the gears are the number of teeth. The number of teeth determine the diametral pitch of the gears and the face width is constrained by this diametral pitch.

After the sizing of the gears, the efficiency of the bevel gears were calculated using Equation 6.10[14]. Here, η is the efficiency of the gear, α is the pressure angle of the gear and z is the number of teeth of the running gear.

$$\eta = cos^2(\alpha) \cdot \frac{1}{1 + cos^2(\alpha) \cdot \frac{\pi}{z} \cdot \left(\frac{\pi}{2 \cdot z} + \alpha\right)} \tag{6.10}$$

6.2.2. Pericyclic Continuous Variable Transmission (PCVT) Design

The PCVT is a gearbox that uses the effects of nutation and pericyclic motion to alter the rotational speed provided by the turboshaft engine. The envisioned design consists of an input shaft, two Reaction Control Members (RCM), two Pericyclic Motion Converters (PMC) and the output shaft. Separately, a Control Variable-Speed Unit (CVU) controls the required gear ratios of the PCVT[11].

The designed PCVT will be able to alter the rotor speeds of the rotorcraft by varying the gear ratios between 13:1 and 2:1 for varying power levels provided by the engine. The design layout of the PCVT is provided in Figure 6.8. The angular velocities of the components are defined by Equations 6.11 and 6.12[11]:

$$\Omega_{PMC} = -\Omega_{in} sin\beta \cdot \hat{j} + (\Omega_{in} cos\beta + (\Omega_{RCM} - \Omega_{in}) \cdot \left(\frac{N_1}{N_2}\right) \cdot \hat{k} \tag{6.11}$$

$$\Omega_{out} = \Omega_{in} + \frac{N_1}{N_2}\frac{N_3}{N_4}(\Omega_{RCM} - \Omega_{in}) \tag{6.12}$$

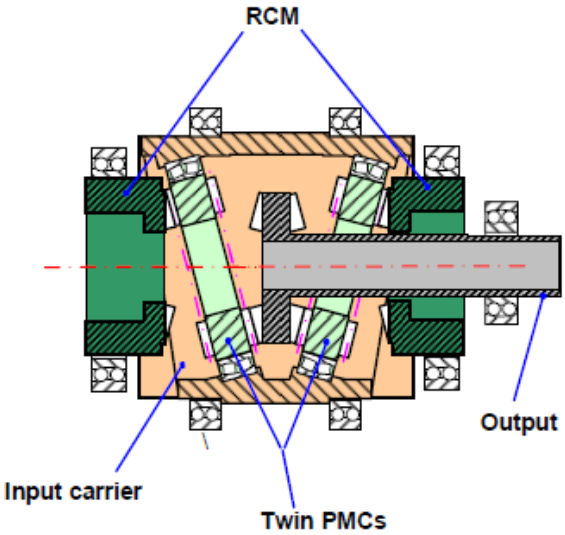

Figure 6.8: Expected layout of the PCVT

In this, N_1,N_2 and N_4 are the number of teeth on the RCM, PMC's and output shaft, respectively. The term Ω defines the rotational speed of a member and β is the angle of nutation. The PCVT is first

[14] URL http://www.gearsolutions.com/article/detail/5402/determining-gear-efficiency [cited 19 January 2017]

designed for a fixed gear ratio scenario. Concluding this, the speed of the RCM is varied, to be able to reduce or increase the gear ratios. The direction of rotation of the RCM with respect to the rotation of the input shaft will determine reduction or increment of the gear ratios. So, in order to reduce the gear ratio, the RCM will have to rotate in the same direction as the input shaft. Based on a base gear reduction of 13:1, the PCVT was designed. The design features are provided in Table 6.5.

Once the speed changes have been calculated, the individual gears have to be sized according to the torques and forces they experience. After analysis, it was understood that the stresses that needed to be addressed were the teeth bending stresses on the gears, whilst staying under the allowed shear stresses. Using Equations 6.13[11] - 6.15[15], the gears were sized and with the dimensions derived, the gear masses were calculated. The gears were assumed to be solid cylinders as were the bearings. The output shaft within the PCVT is modelled as a solid cylindrical shaft. Where D_p is the pitch diameter, f is the face width, P_d is the diametral pitch, K_0, K_v, K_s,K_m and K_m are constants.

$$\sigma_{teeth} = \frac{10T_{max}}{ND_p}\frac{K_0}{K_v}\frac{Pd}{f}\frac{K_sK_m}{J} \quad (6.13) \qquad P_d = \frac{N}{D_p} \quad (6.14) \qquad D_{shaft} = 1.72\left(\frac{T_{max}}{\tau_{max}}\right)^{\frac{1}{3}} \quad (6.15)$$

With these, it was possible to calculate the dimensions of the PCVT gearbox and the resulting weight. The material used for the design of the components of the PCVT is AISI 4340 steel. The maximum allowable stress is 470 MPa[16]. All calculations are performed with a safety factor of 1.2. The total dimensions and the Weight of the PCVT is provided in Table 6.6. The weights of the total gearbox system include the CVU and bearings as well.

The final design aspect of the PCVT is the characteristics of the CVU. This unit controls the speed of the RCM unit and hence, adjusts the gear ratio according to the situation. This includes two electric motors that is used separately for either increasing or decreasing gear ratios. In order to be able to vary the speed of the RCM, power needs to be delivered by the CVU to the electric motors. To calculate the amount of power required, the Circulation Ratio (CR) is calculated in Equation 6.16[11].

$$CR = \frac{\Omega_{RCM}}{\Omega_{in}}\left(\frac{\frac{\Omega_{in}}{\Omega_{out}} - 1}{\frac{\Omega_{RCM}}{\Omega_{in}} - 1}\right) \quad (6.16) \qquad P_{CVU} = P_{out} \cdot CR \quad (6.17)$$

From this, it is possible to know the power required to continuously vary the transmission system. This power is delivered separately by the APU system described in Section 6.1. It was calculated that the maximum power required for the transmission will be 84 kW. The varying power needed by the PCVT is shown in Figure 6.9.

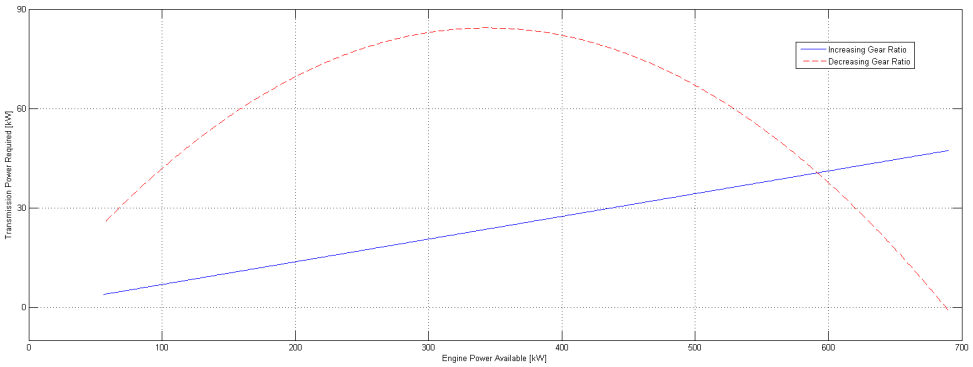

Figure 6.9: Power Required for Varying Transmission

[15] URL www.engineeringtoolbox.com/torsion-shafts-d/_947.html [cited 24 January 2017]
[16] URL www.azom.com/article.aspx?ArticleID=6772 [cited 24 January 2017]

6.2.3. Shaft Design

The sizing of the drivetrain shafts is similar to the sizing of the gears. First, the torque on the shaft is calculated. As the torque is the main force on the shafts, they are sized according to this torque. The shafts are assumed to be thin-walled. The sizing of the shafts is done using Equation 6.18, where R is the radius of the shaft, T is the torque on the shaft, t is the thickness of the shaft and τ_y is the yield shear stress of the material[12]. The mass of the shaft can then be calculated with Equation 6.19, in which m is the mass of the shaft and L is the length of the shaft.

$$R = \sqrt{\frac{T}{2\pi \cdot t \cdot \tau_y}} \tag{6.18}$$

$$m = 2 \cdot \pi \cdot R \cdot t \cdot L \cdot \rho \tag{6.19}$$

From these equations, it can be derived that the mass is optimised for minimum thickness. However, for a thickness lower than a certain value, the material is not stiff enough. A minimum thickness of 2 mm is assumed for this and thus, this thickness will be taken for all shafts. Then, the needed radii can easily be calculated. Just as with the gears, although the torque on the second and third shafts will be slightly lower than that of shaft one, the dimensions of the first three shafts will be equal.

6.2.4. Verification of the Gear and Shaft Design Program

As the program for the transmission design, excluding the PCVT, only consists of very basic calculations, it is only needed to check the calculations by hand calculation. While doing this, several mistakes have been spotted. This mostly involved mistakes due to copying lines and then inappropriately changing the variables to match the slightly different equation. Furthermore, some inputs were in the wrong units due to which an unrealistic answer was obtained. This was the second way of verifying this program, the outcomes were constantly checked for their feasibility. An example of this is the calculation of the torques on the shafts and gears. At some point, the torque on the second shaft was in the order of 10 Nm, which is obviously incorrect. Another example is the calculation of the needed radii of the shafts. At some point, the needed radius was in the order of 1 mm, which is also an unrealistic value as it is smaller than the thickness.

6.3. Results

In the previous section, the method of adapting the engine and designing the transmission has been described. In this section, the results of the design process will be displayed. Table 6.3 describes the range of RPMs that the main rotor can operate at for three stages of the mission. As can be seen, the PCVT is quite useful where it can vary the RPM of the rotor for given power levels. This can help with controllability and efficiency.

Table 6.3: Sample range of RPMs

Power Required	Rotor RPM Range
610 kW	169 – 188 RPM
342 kW	131 – 147 RPM
58 kW	71 – 85 RPM

In Table 6.4 the power required, the respective fuel flows and the SFCs are provided for four different stages in the mission. The stages in the mission analysed are for take off, forward flight, initiating the hover and end of the hover, in that order. It is to be noted that the fuel flows include the consumption of the APU system as well. The assumption is that take off will be initiated at maximum rated power. Each power rating is adjusted for the transmission losses for the specific flight stage.

Table 6.4: Fuel flows and sfc's at different flight stages

Mission Stage	Power Required	Fuel Flow	SFC
Takeoff	746 kW	260.3 kg/hr	0.316 $kg/kw-hr$
Forward Flight	417 kW	149.7 kg/hr	0.299 $kg/kw-hr$
Hover Initiate	610 kW	192.7 kg/hr	0.275 $kg/kw-hr$
Hover End	58 kW	58.4 kg/hr	0.587 $kg/kw-hr$

The remainder of the transmission is represented by three running gears, four mating gears and four shafts. All gears have a pressure angle of 20^o.

All four shafts have a thickness of 2 mm and the first three shafts have a radius of 0.033 m. The first shaft has a length of 0.3 m, the second shaft has a length of 0.5 m and the third shaft has a length of 0.2 m. The first two running and mating gears, which together cause the 180 deg change of direction, as has been mentioned in Section 6.2, have the same number of teeth, pitch diameter and face width. The diameter of these gears was chosen to be the maximum, namely 0.184. The needed face width is then 0.0254 m. Finally, the number of teeth was determined to be 40. As stated in Subsection 6.2.1, the overall gear ratio of these gears is 1.

The fourth shaft has a length of 0.1 m and a radius of 0.1 m. The third running gear has 30 teeth, a pitch diameter of 0.324 m and a face width of 0.127 m. The third and fourth mating gears have the same characteristics. They both have 55 teeth, a pitch diameter of 0.454 m and a face width, equal to the face width of the third running gear, of 0.127 m. This combination of teeth causes a gear ratio of 1.8. The total mass of the shafts is 4.8 kg and the total mass of the gears is 447 kg. Finally, the total efficiency of the transmission is 87.7 %

Table 6.5: Design features of the PCVT

N_1	N_2	N_3	N_4	β	RPM_{in}
20	22	66	65	2 deg	6165 RPM

Table 6.6: Dimensions and weight of PCVT

Diameter	Length	Total Weight
0.25 m	0.375 m	161 kg

The complete weight of the drivetrain and the propulsion system is provided in Table 6.7. The engine weight includes the wave rotor and a brief estimation of the expected housing or cowling of the unit.

Table 6.7: Weights of powertrain and drivetrain

Transmission Weight	Engine Weight	Length of Transmission
613 kg	286 kg	1.1 m

When comparing this to estimated weights of other rotorcraft drivetrain systems, the PCVT not only manages to be lightweight, but it also provides the ability to continuously vary the transmission. Using the method provided by Timothy Krantz, a conventional gearbox would weigh approximately 240 kg[13]. The PCVT is about 80 kg lighter.

7 Aerodynamic Design

This chapter discusses the aerodynamic design and the choices leading to the final design. Firstly, the process is explained briefly and depicted in a block diagram in Section 7.1. Then, the airfoil selection will be described in Section 7.2. Next, some rotor parameters are given and explained in Section 7.3. Furthermore, in Section 7.4 the blade geometry and the methods to determine it are explained. Then, the use of RPM-control is justified in Section 7.5. After this, the forward flight characteristics are shown in Section 7.6 and finally, the method is validated in Section 7.7.

7.1. Design Process

In this section, an overview of the process is shown. Figure 7.1 shows the order of the actions performed in order to obtain a blade design.

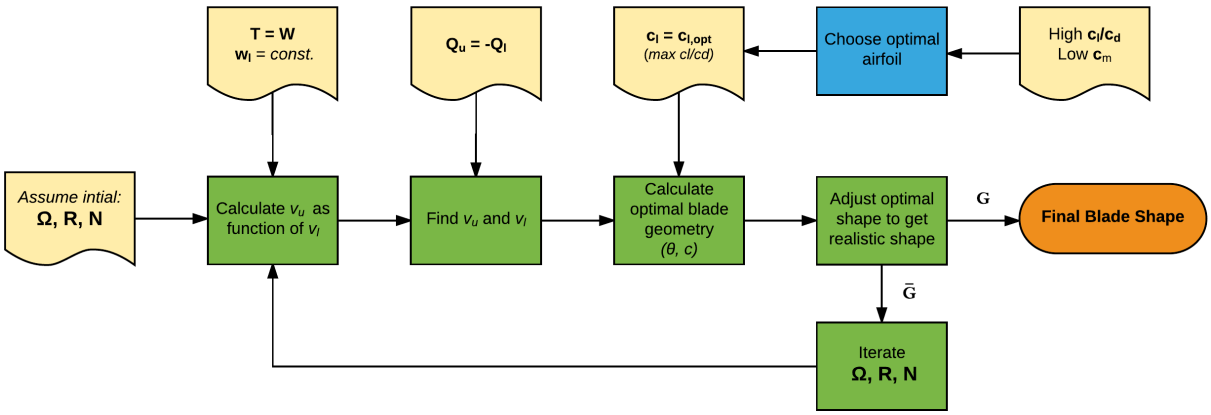

Figure 7.1: Block diagram of the rotor design process

7.2. Airfoil Selection

In typical rotorcraft, the flow conditions in forward flight are the dominant factor in determining the airfoil of the blade. The high relative airspeed of the advancing side of the disk usually require the use of supercritical airfoils at outer section of the blade. The retreating side encounters stall and regions of reverse flow on the inside of the blade, and therefore airfoils with a high lift coefficient at low Mach numbers will be required. These requirements however, are relevant to helicopters which are designed to be able to fly at a high forward speed.

In this design of the 24-hour hovering machine, forward flight is only a small fraction of the total mission and has no speed requirements. This allows for a shift of focus to optimal hover performance, without having to design for the high Mach numbers encountered in forward flight.

In order to achieve a high performance in hover, the airfoil should be able to achieve high lift in combination with low drag. Therefore, an airfoil with a high c_l/c_d is needed. Furthermore, for structural considerations it is best to have a low twisting moment, and therefore a low c_m is preferred as well.

Based on literature, some rotorcraft airfoils were selected for comparison. The Boeing Vertol VR-7 and VR-12 are considered, as well as the Sikorsky SC1095 and the Bell FX 96-H-08[14]. For these airfoils, XFOIL was used to generate polar data in order to compare the airfoil parameters. For a Reynolds number of 6,000,000 and a Mach number of 0.4, the c_l/c_d and c_m plots are shown in Figure 7.2.

The c_l/c_d plot, Figure 7.2a shows that the highest value is obtained for the VR-7 airfoil, with a peak around a 4^o angle of attack. The other airfoils show similar curves, with the exception of the VR-12 retaining a higher c_l/c_d for higher angle of attack. Based on this observation, the VR-7 would be the best airfoil to choose. However, the VR-7 has a high negative pitching moment coefficient, as seen from Figure 7.2b. As mentioned before, pitching moment is preferred to be low, which eventually led to the choice of using the VR-12 airfoil.

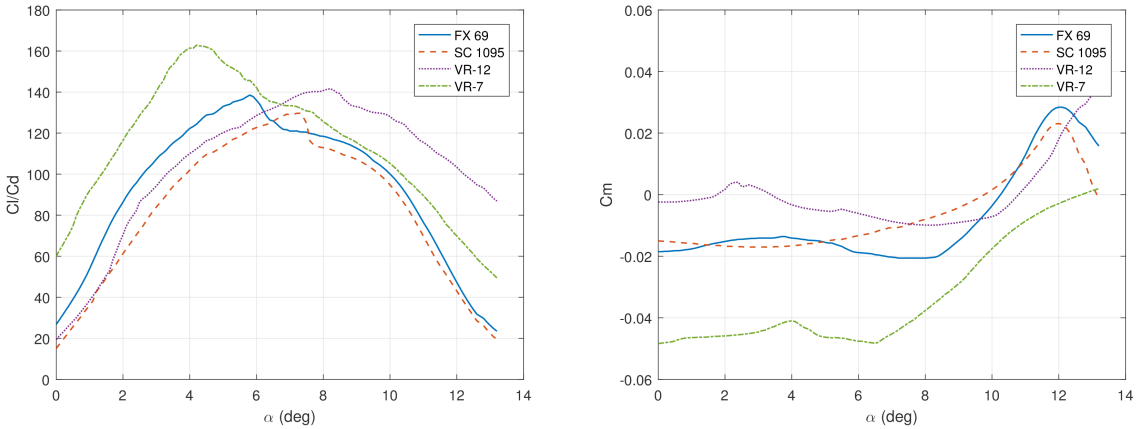

(a) c_l/c_d vs. α

(b) c_m vs. α

Figure 7.2: Comparison of four different airfoils based on XFOIL generated data

7.3. Rotor configuration

In this section, it is explained how the blade radius R, the number of blades N and the rotational speed Ω were obtained. As seen in Figure 7.1, an initial guess of these parameters was made in order to start the calculation and iteration process. These values are shown in the left column of Table 7.1, and the end values are shown in the right column.

An Ω of 20 rad/s was assumed as initial value, then after iteration a value of 17.5 rad/s resulted in being optimal. Furthermore, the radius of 8 m turned out to be a good initial estimate and was kept the same. A lower radius would require the chord to be too large and the optimal shape to be an infeasible shape. A higher radius would be structurally infeasible. The current radius allows for a good approximation of the ideal shape, as it will be explained in more detail in Section 7.4.3. The same goes for the number of blades N. An initial amount of three blades per disk was assumed, but this resulted in a blade shape with an unrealistically high root chord. With an amount of five blades, the ideal shape can be approximated more easily.

Furthermore, the vertical separation between the upper and lower rotor d_{rotors} was set to and kept at 2.0 m. This value is based on the fact that the upper rotor wake has nearly fully contracted at a distance of $0.25R$ below the disk, which equals 2.0 m[15]. Choosing the lower rotor location in the fully developed wake means a simplification of the method, which is an advantage for the design process.

Table 7.1: Initial and final rotor parameters

	Initial	**Final**
Ω_{max} $[rad/s]$	20	17.5
R $[m]$	8.0	8.0
N	3	5
d_{rotors} $[m]$	2.0	2.0

7.4. Blade Geometry

This section describes the method and results of the blade geometry determination. As a starting point, the following three constraints were taken into account in order to determine the blade shape:

1. The provided thrust has to be equal to the weight.
2. The induced velocity has to be constant along the blade span, for highest efficiency.
3. The torque of the lower rotor has to be equal and opposite to the torque of the upper rotor.

7.4.1. Method

In order to determine the flow effects of having two rotors operate in the same axis, an approximate model of the real world situation is used. The assumption is made that the upper rotor and the lower rotor are located sufficiently far apart, so that the upper rotor wake has contracted fully. The theoretical contraction ratio of 0.707 is used, which means that the area of the upper rotor wake on the lower rotor is half the area of the rotor disk[16].

The differential thrust of a stream tube is equal to the rate of change in momentum of the accelerated air. The total rotor system, can be modelled as infinitely many infinitely small stream tubes. The integral of the thrust of these stream tubes yields the total thrust of the rotor system. The total velocity change starts from stationary air far upstream to W_l in the far wake, hence the total thrust is given by Equation 7.1. Here A, the domain of integration is the wake area. The total power is equal to the rate of kinetic energy leaving the wake area, Equation 7.2.

$$T_{total} = \int_A \Delta\dot{m} \cdot w_l dA \qquad (7.1) \qquad\qquad P_{total} = \int_A \frac{1}{2} \cdot \Delta\dot{m} \cdot w_l^2 dA \qquad (7.2)$$

The power and thrust are a function of wake velocity. The power needs to be minimised for a certain set value of thrust. Since these are dependent on the function for wake velocity an optimised wake velocity profile has to be found. Using the calculus of variation mathematical frame work for this, the so called 'Isoperimetric Problem', it can be proven that the optimum velocity is a constant velocity distribution[17].

The thrust of the upper and lower rotor is calculated using momentum theory. Here for the upper rotor the single rotor helicopter model with zero climb velocity is employed. For the lower rotor part that is in the wake, the single rotor helicopter model in climb is used. For the part that is not in the wake, the model without climb velocity is used.The climb velocity used is two times the induced velocity of the upper rotor. The lower rotor is modelled in the complete developed wake of the upper rotor as explained earlier, using Equation 7.3 and 7.4.

$$T_u = 2\rho A_u v_u^2 \qquad (7.3)$$

$$T_l = 2\rho A_{l,in}(2v_u + v_{l,in})v_{l,in} + 2\rho A_{l_out} v_{l,out}^2 \qquad (7.4)$$

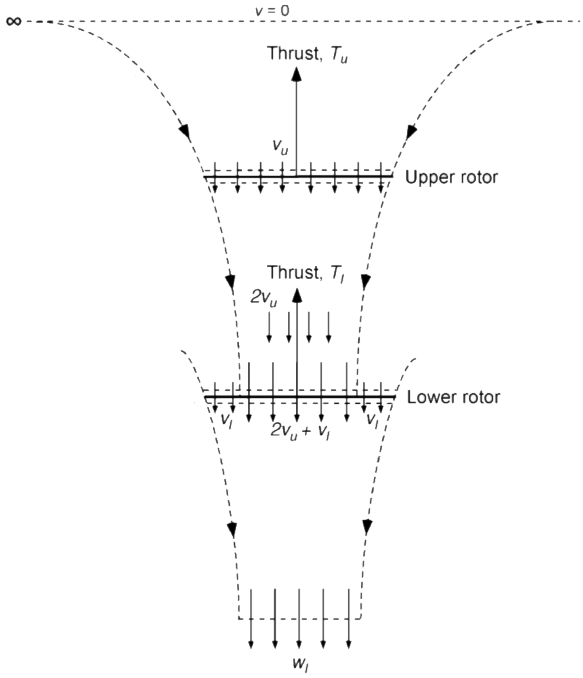

Figure 7.3: Wake model for two coaxial rotors[16]

Here $A_u, v_u, A_{l,in}, v_{l,in}, A_{l,out}, v_{l,out}$ are the area of the upper rotor, the induced velocity of the upper rotor the area of the lower rotor in the developed wake, the velocity of the lower rotor in the developed wake, the area of the lower outside the developed wake and the velocity of the lower rotor outside the developed wake respectively. Since the second rotor is modelled completely in the developed wake, the areas can be calculated by the following Equation 7.5.

$$A_{l,in} = A_{l,in} = \frac{1}{2} \cdot A_u \tag{7.5}$$

For simplicity of the propulsion and drivetrain system, the rotational velocity Ω is to be equal for the upper and lower rotor. When this is done the power provided to the upper and lower rotor should be the same, to keep torque balanced, which leads to Equation 7.6.

$$Q_u = \frac{P_u}{\Omega} = \frac{P_l}{\Omega} = Q_l \tag{7.6}$$

Here Q_u, Q_l, P_u, P_l are the torque and power for the upper and lower rotor respectively. From momentum theory, both with and without climb velocity, a similar analysis as the thrust yields the following power for upper and lower rotor, Equations 7.7 and 7.8.

$$P_u = 2\rho A_u v_u^3 \tag{7.7}$$

$$P_l = 2\rho A_{l,in}(2v_u + v_{l,in})^2 v_{l,in} + 2\rho A_{l_o ut} v_{l,out}^3 \tag{7.8}$$

From momentum theory it is well known that the velocity in the wake is two times the induced velocity both for climb and normal conditions[17].

The wake velocity w_l has to be constant to obtain minimal induced power. The wake velocity consists of two parts. The first part, the inner part $w_{l,in}$ is the contribution of the upper and lower rotor. Secondly

the outer part $w_{l,out}$ is only the lower rotor. The velocity of the inner and outer part are given by Equation 7.9.

$$w_{l,in} = 2 \cdot v_u + 2 \cdot v_{l,in} w_{l,out} = 2 \cdot v_{l,out} \tag{7.9}$$

Setting these equal for minimal induced power leads to Equation 7.10.

$$v_{l,out} = v_u + v_{l,in} \tag{7.10}$$

Using Equation 7.3, 7.4 and 7.5 such that $T_l + T_u = W$ together with 7.10 can be solved for $v_u(v_{l,in})$. When v_u and $v_{l,in}$ are known, the ideal power can be calculated for both upper and lower rotor separately. Since these powers have to be equal, Equation 7.6, v_l and v_u can be calculated. Since this implies solving a third degree polynomial a bisection algorithm was used. Here the function $f(v_u) = P_l - P_u$ is the difference between upper and lower power, which should become zero. As initial bisection upper and lower bound 1 and 20 m/s were used (range $R = 19$), which covers a large enough design space in our specific helicopter design, while keeping the computation cost relative low.

7.4.2. Ideal Blade Geometry

The method described in Subsection 7.4.1 results in an induced velocity profile from which the ideal blade geometry (twist, chord) can be determined. The thrust delivered by a blade element should be equal to the thrust from momentum theory. Figure 7.4 illustrates the momentum theory area and the blade element area are in both models the thrust delivering areas which should give equal thrust. The thrust for a given blade element is given by Equation 7.11.

$$\Delta T_{blade} = \frac{b}{2} \rho v^2 c_l c \Delta r \tag{7.11}$$

Here b is the number of blades, v is the velocity seen by the air-foil, c_l is the corresponding 2D lift coefficient, c the chord and Δr a small section of the blade. The thrust from momentum theory, at the disk location were the blade element delivers lift, is given by Equation 7.12.

$$\Delta T = 4\pi \rho v_i^2 r \Delta r \tag{7.12}$$

When blade element velocity is set equal to Ωr and since the thrust of both models should be equal, a relation for $cl(x)c(x)$ can be obtained, Equation 7.13.

$$cl(x)c(x) = \frac{8\pi v_i^2}{b\Omega^2 r} \tag{7.13}$$

A weak point of blade element momentum theory is that it is not a variational problem statement. That is, a change in lift, drag or general air foil characteristics of a blade section does not influence the other sections. This is not physically correct, in general a change in a section will change the pressure distribution in its surrounding. However, since the blades are relative smooth, this model is quite accurate. Moreover, optimisation of each separate section will lead to an optimised design.

The induced velocity necessary to produce lift leads to the induced power, this is the least power required for a hovering device. The other main contribution investigated is the profile power, obtained from profile drag. When each blade element airfoil functions at $\frac{c_l}{c_d}|_{max}$ this power is minimised. The point were $\frac{c_l}{c_d}|_{max}$

occurs is an airfoil characteristic point for a given incidence angle and cl, which will be referred to as $c_{l,opt}$. Substitution of $c_{l,opt}$ into 7.13 leads to the optimised blade chord distribution, Equation 7.14.

$$c(x) = \frac{8\pi v_i^2}{b\Omega^2 r c l_{opt}} \tag{7.14}$$

When c_l is linearised as function of α, Equation 7.15, the ideal twist can be calculated.

$$cl(\alpha) = (\alpha - \alpha_0)\frac{\mathrm{d}cl}{\mathrm{d}\alpha} = (\alpha - \alpha_0)cl_\alpha = cl_{opt} \tag{7.15}$$

For a helicopter in hover the angle of attack at each section can be calculated using Equation 7.16. Figure 7.5 illustrates the decrease in angle of attack with respect to the twist angle θ due to the induced velocity.

$$\alpha = \theta - atan\left(\frac{v_i}{\Omega R}\right) \tag{7.16}$$

Solving 7.15 and 7.16 for θ Equation 7.17

$$\theta = atan\left(\frac{v_i}{\Omega R}\right) + \alpha_0 + \frac{cl_{opt}}{cl_\alpha} \approx \frac{v_i}{\Omega r} + \alpha_0 + \frac{cl_{opt}}{cl_\alpha} \tag{7.17}$$

In the right hand side of Equation 7.17 the atan function is linearised around zero, since $v_i << \Omega r$. In the blade shape calculations this linearisation is not done, however it gives a good intuitive understanding of the approximately hyperbolic varying twist.

The previous analysis of the chord distribution and twist is valid for the upper rotor and the lower rotor outside the wake of the upper rotor. For the lower rotor inside the wake of the upper rotor a similar analysis can be applied. Here the only difference is the equation for ΔT obtained for blade element. From Equation 7.4 the thrust can easily been found corresponding to an small disk area and blade element section. The rest of the analysis is the same, and thus not repeated.

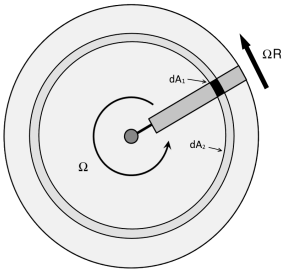

Figure 7.4: Rotor disk with assigned areas[14]

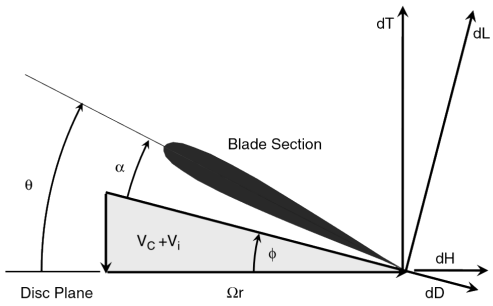

Figure 7.5: Blade section with angles and forces denotation[14]

Graphs of this ideal shape are presented in Figure 7.6. Initially, a root cutout of 1 m was chosen, as is shown on the x-axes range. It can be seen in Figure 7.6a that the upper rotor chord ideally is high at the root, and decreases to approximately 0.1 m at the tip. For the lower rotor, due to the influence of the upper rotor, a step increase of chord is observed around 5.7 m, which is where the edge of the upper

rotor wake is located. Since it is necessary to increase the induced velocity outside the wake and c_l is constant the discrete jump is necessary to comply with the idealised equations.

In Figure 7.6b the ideal twist is shown, a high twist at the root becoming increasingly smaller towards the tip. Again a sudden jump is observed at the point where the upper rotor wake stops. The decrease in twist can be explained because the velocity of the upper rotor, modelled as climb velocity is not present for the outer section, thus leads to an decrease in angle ϕ which explains the sudden decrease in twist.

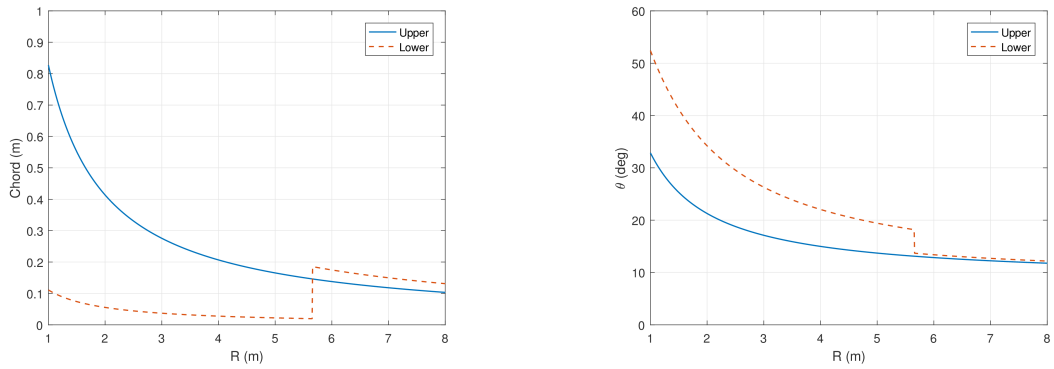

(a) Ideal chord distribution

(b) Ideal Twist Distribution

Figure 7.6: Resulting ideal blade geometry

7.4.3. Design Blade Geometry

In order to get the best performance, these optimal blade shapes should be approximated as close to the reality as possible. Some adjustments were made to the ideal geometry in order to end up with the actual design. These adjustments are explained below. The final rotor geometry is depicted in Figure 7.7.

Upper Rotor Adjustments

As a start, the maximum chord for the upper rotor was set to 0.5 m, as the optimal case would cause the root chord to become too high. The optimal twist is continuous and varying from around 30 degrees at the root to around 12 degrees at the tip. It was decided to keep this shape for the actual design.

Upper Rotor Adjustments

For the lower rotor, the chord has been set constant at 0.2 m. The reason for this is that the optimal shape requires the chord to be only 2 cm at its minimum, which is structurally infeasible. The sudden change in twist around the wake edge has been smoothed, by applying a third-degree polynomial at a range of 1 m around this position.

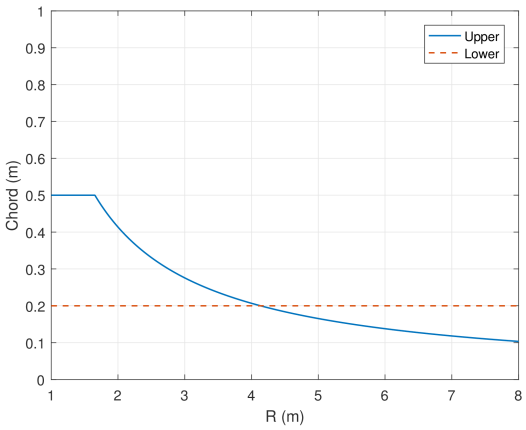

(a) Design chord distribution

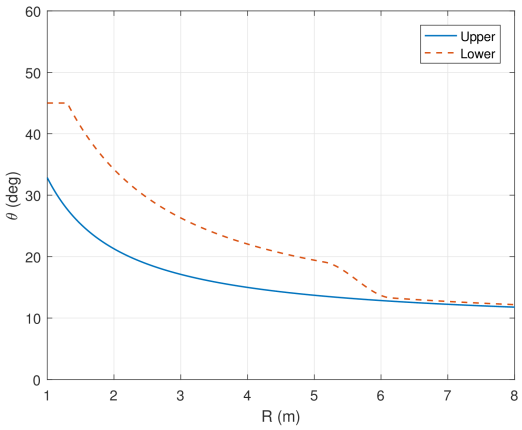

(b) Design Twist Distribution

Figure 7.7: Resulting design blade geometry

7.4.4. Blade Element Momentum Thrust Calculations

Since the blades are not the optimal shape, the thrust will be different than the thrust obtained from momentum theory alone. Instead the momentum theory and blade element theory are combined to obtain a relation for the induced velocity, as explained in Section 7.4.1. As can be seen in Figure 7.5 the inflow angle ϕ can be calculated for each section. As explained for the lower blade in the wake the thrust for momentum theory in climb is used with climb velocity equal to two times the upper blade induced velocity. The angle of attack can be calculated when ϕ is known, from which the lift and drag can be calculated since blade chord and profile properties c_l and c_d are known. The lift and drag forces on the element can be converted to thrust and tangential force 'T' and 'H' using Equation 7.18 and 7.19.

$$dT = cos(\phi)dL - sin(\phi)dD \qquad (7.18) \qquad dH = cos(\phi)dD + sin(\phi)dL \qquad (7.19)$$

The thrust can be integrated over the blade to obtain the total thrust. The power and torque can be calculated by multiplying the tangential force with the radial location 'r' for torque and torque multiplied by omega yields the power, Equations 7.20 and 7.21.

$$dQ = [sin(\phi)dL + cos(\phi)dD] \cdot r \qquad (7.20) \qquad dP = [sin(\phi)dL + cos(\phi)dD] \cdot r\Omega \qquad (7.21)$$

To take tip loss into account, Prandtl tip loss correction is used[17]. Since thrust varies with the square of induced velocity the thrust obtained is multiplied with the square of the Prandtl tip loss factor. for the drag the tip loss is not taken into account. since these phenomenon occur at the tip the change in inflow angle is assumed negligible such that the drag is not influenced by the change in induced velocity. The reason that at the tip the inflow angle change can be neglected is due to the large radial velocity, $\Omega \times R$. In Figure 7.8 the decrease to zero of the velocity profile is due to the tip loss factor. Similar the loss in thrust near the tip in Figure 7.9 can be seen. For the idealised blade design and an take off mass of 5000 kg and an rotational velocity of 17.5 rad/s, the hover power is calculated to be 517 kW. Current technology uses linear twist and taper. A blade with linear twist and taper was modelled in the same manner, from which a power of 630 kW was obtained. The idealised hyperbolic twist and tapered blades are thus approximately 20% more efficient.

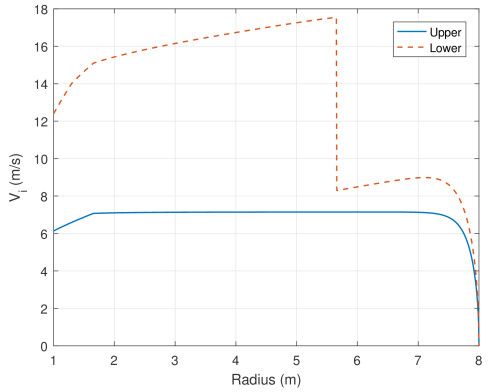

Figure 7.8: Induced velocity distribution of the rotorblades

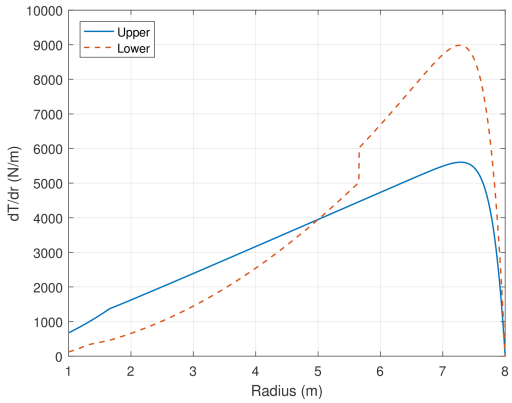

Figure 7.9: Thrust distribution of the rotorblades

In Figures 7.8 and 7.9 there are some important things to notice. First the velocity profile is near constant, leading near to a linear increasing thrust loading. As explained this lead to the a minimum induced power were the design was optimised for. The reason that it is not exactly linear is due to the deviations from the ideal blade as explained. The sudden decrease in velocity through the disk area of the lower rotor at $r = 5.65\ m$ is due to the wake of the upper rotor being modelled as not being present for $r > 5.65\ m$. The actual induced velocity of the lower rotor is lower inside the wake then outside the wake, since the disk velocity includes two times the upper velocity, for the section inside the wake. The increase in thrust is due to similar phenomenon. The rotor functions more efficient outside the wake of the upper rotor, hence the thrust increases. The kink in the beginning of both the thrust and velocity profile is due to the constant chord instead of parabolic, near the root. For the lower rotor this kink is due to the twist distribution, which has a kink there.

7.5. RPM-Control

In general translational motion of helicopters along the z-axis is, of course acceleration controlled, by regulating the collective pitch. For this helicopter, the rotational speed of the rotors are regulated instead. In this section it will be explained why rpm-control is more efficient that collective control, during longer flights. For small adjustments during flight, necessary to compensate for wind gusts continuous trailing edge flaps are used, see Chapter 9.

To determine the that RPM control is more efficient a relation between power, Ω, and collective pitch β has to be obtained. Here Ω is the rotational speed in $[rad/s]$ and collective pitch the change in pitch angle in rad. Furthermore, a relation between thrust Ω and β is necessary to relate changes in weight. From Figure 7.5 The power and thrust of a small blade section, dP and dT, can be determined, which is simply $dP{=}dM\ \Omega = r\ dH\Omega$ given in Equations 7.22 and 7.23.

$$dP = \frac{b}{2}\rho V^2 \cdot [clsin(\phi) + cdcos(\phi)] \cdot \Omega rc \cdot dr \approx \frac{b}{2}\rho(\Omega r)^2 \cdot [clv_i + cd \cdot \Omega r]c \cdot dr \tag{7.22}$$

$$dT = \frac{b}{2}\rho V^2 cl \cdot c \cdot dr \approx \frac{b}{2}\rho(\Omega r)^2 cl \cdot c \cdot dr \tag{7.23}$$

The total power and thrust are obtained by integrating Equations 7.22 and 7.23 over the blade. It can be seen that the only variables that can be changed during flight are Ω and c_l. The change in c_l is obtained by collective pitch. Collective pitch is not used, however to prove that it is first assumed that both could

be varied and shown that keeping collective constant yields the least power for a certain blade design at a certain weight/thrust during flight. c_l as function of r is then given by Equation 7.24

$$cl(r) = cl_0(r) + cl_\alpha \beta \tag{7.24}$$

Here it should be clear that $cl_0(r)$ is the blade lift at the design operation point and it is assumed that it does not vary significantly with induced velocity. Since blade element thrust of a section should equal the momentum theory thrust of the same area as explained in Section 7.4.1, the induced velocity can be obtained as function of r, c, Ω and c_l, Equation 7.25

$$v_i = \sqrt{\frac{b\Omega^2 cl \cdot r}{8\pi}} \tag{7.25}$$

Substitution of the induced velocity 7.25 and c_l 7.24 into 7.23 and 7.22 and integrating yields 7.26 and 7.27

$$\begin{aligned} P = \Omega^3 \left[\int_{R_0}^{R} \frac{b}{2} \rho \left(r^2 cl_0^{\frac{3}{2}}(r) \sqrt{\frac{bc(r)r}{8\pi}} c(r) + r^3 a cl_0^2(r) c(r) + r^3 c d_0 c(r) \right) dr \right] \\ + \Omega^3 cl_\alpha \beta \left[\int_{R_0}^{R} \frac{b}{2} \rho \left(\frac{3}{2} r^2 cl_0^{\frac{1}{2}}(r) \sqrt{\frac{bc(r)r}{8\pi}} c(r) + 2r^3 a cl_0(r) c(r) \right) dr \right] \end{aligned} \tag{7.26}$$

$$T = \Omega^2 \left[\int_{R_0}^{R} \frac{b}{2} \rho r^2 cl_0(r) c \cdot dr + \int_{R_0}^{R} \frac{b}{2} \rho r^2 cl_\alpha \beta c \cdot dr \right] \tag{7.27}$$

Here it is assumed that $cl^{\frac{3}{2}}$ and cl^2 can be linearised around the design c_l. And that c_d can be written as $c_d = c_{d_0} + a \cdot cl^2$. Here the power and thrust relation can be reduced to 7.28 and 7.29.

$$P = k_1 \Omega^3 + k_2 \Omega^3 cl_\alpha \beta \tag{7.28}$$

$$T = k_3 \Omega^2 + k_4 cl_\alpha \beta \Omega^2 = W \tag{7.29}$$

From 7.29 the collective pitch can be written as function of Ω and the weight, Equation 7.30

$$\beta = \frac{W - k_3 \Omega^2}{k_4 cl_\alpha \Omega^2} \tag{7.30}$$

Substitution of 7.30 into 7.28 yields the power as function of Ω and the weight. The change in power with a change in omega should be zero, in order to be at an optimal condition. Hence the partial derivative is set to zero and solved for Ω, Equation 7.31.

$$\frac{\partial P}{\partial \Omega} = 0 : \Omega = \sqrt{\frac{\frac{k_2}{k_4} W}{3k_1 - 3k_2 k_3}} = k_5 \cdot \sqrt{W} \tag{7.31}$$

When this optimal Ω is substituted into the relation for β it becomes clear that β is a constant, Equation 7.32.

$$\beta = \frac{1 - k_3 k_5^2}{k_4 cl_\alpha k_5^2} \tag{7.32}$$

Since the rotor blades are optimally designed for a specific weight to operate at a specific rotational speed, see Section 7.4, the blade should stay at this pitch and vary omega according to Equation 7.31.

7.6. Aerodynamic Characteristics Forward Flight

The rotorcraft is designed to hover, but it must also fly between hover stations. The forward flight segment is only a small part of the total mission, but it is desirable to minimise fuel consumption. The main objective of this section is to estimate what the power in steady forward flight will be at MTOW when the forward flight segments are executed first.

7.6.1. Wake Analysis Forward Flight

In forward flight the wake will exhibit different properties than in hover. The combination of forward speed and rotation makes the inflow distribution across the rotor disc more complex. The induced velocity in forward flight can be related to the induced velocity in hover according to Equation 7.33. It would be more realistic to see the induced velocity as a complex vorticity pattern, consisting of trailing shed and bound vortex elements, but this is not relevant for analysing the forward flight performance of rotorcraft[17]. The local induced velocity at the disk can be analysed with Equation 7.34, in which ψ is the azimuth position of the rotor blade and K is the induced velocity distortion factor. The value of the distortion factor scales with 0.0825 times the forward velocity for $\in [0, 30]$[17].

$$v_1 = \sqrt{-\frac{V^2}{2} + \sqrt{\left(\frac{V^2}{2}\right)^2 + v_{1_{hov}}^4}} \tag{7.33}$$

$$v_L = v_1\left(1 + K\frac{r}{R}cos(\psi)\right) \tag{7.34}$$

The centre of the lower rotor disk coincidences with the wake centre of the upper rotor for hover. This is however not valid in forward flight, because the wake will be skewed in a direction which is opposite to the direction of flight. The skew angle in Equation 7.35 depends on the distance between the two rotors d_{rotors}, the velocity at which the rotorcraft flies V, the angle of attack of the tip path plane of the rotors α_{TPP} and the induced velocity of the of the upper rotor v_1. It was assumed that the induced velocity between the two rotors follows a straight line. This is justified by the fact that the forward flight velocity is larger that the induced velocity of the upper rotor.

Furthermore the induced velocity of the upper rotor is not uniformly distributed in radial direction, which implies a variation in skew angle. However, it was decided to take the average induced velocity in order to find the skew angle. The skew angle will the determine the shift of the the upper rotor wake d_{wake} and hence the affected area on the lower rotor. The shift of the wake was determined using Equation 7.36.

$$\chi = tan^{-1}\left(\frac{Vcos(\alpha_{TPP})}{Vsin(\alpha_{TPP}) + v_{1_{ave}}}\right) \tag{7.35}$$

$$d_{wake} = tan(\chi)d_{rotors} \tag{7.36}$$

A large forward flight velocity would mean that the affected area will be smaller and hence the mutual interference is reduced. Depending on the forward flight velocity of the rotorcraft, the wake could be shifted such that it falls completely within the rotor disk of the lower rotor. Another option is that the wake falls partly in the lower rotor disk. The last possibility is that the wake falls completely outside the disk of the lower rotor. The forward flight velocity will be around 25 m/s and therefore it is very likely that the wake of the upper rotor will fall inside the disk of the lower rotor. This means that the lower rotor is characterised with two areas, each with a different induced velocity distribution.

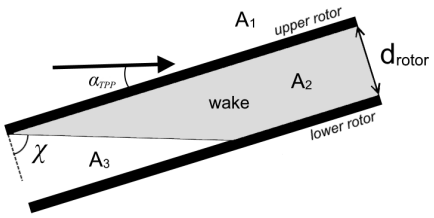

Figure 7.10: Wake geometry coaxial in forward flight

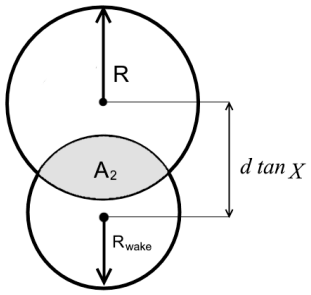

Figure 7.11: Wake upper rotor on lower rotor disc

In Figure 7.10 the induced velocity distribution of the upper and lower rotor are given. Three different areas can be distinguished. The induced velocity across area A_3 has the same induced velocity distribution as the upper rotor. This is due to the fact that this area falls outside the wake of the upper rotor. The induced velocity across area A_2 is characterised with a higher induced velocity distribution than the other two areas. This area is located inside the wake of the upper rotor. This means that the induced velocity inside this area is the sum of the induced velocity of the upper and the lower rotor. Similar to hover, it is assumed that the spacing between the two rotor blades is sufficient such that the area affected lies in the vena contracta of the wake. Hence the contraction ratio is $\frac{1}{2}\sqrt{2}$. In order to determine the area of the lower rotor that is affected by the wake of the upper rotor, it is necessary to find the shift of the upper rotor wake. From this the affected area was calculated by using Equation 7.37, which depends on the wake shift d_{wake}, lower rotor radius R_L and wake radius of the upper rotor r_{wake}. In figure 7.11 the area inside the wake of the upper rotor is illustrated.

$$A_2 = r_{wake}^2 cos^{-1}\left(\frac{d_{wake}^2 + r_{wake}^2 - R_L^2}{2d_{wake}r_{wake}}\right) + R^2 cos^{-1}\left(\frac{d_{wake}^2 + R_L^2 - r_{wake}^2}{2d_{wake}R_L}\right) - \frac{1}{2}\sqrt{(-d_{wake} + r_{wake} + R_L)(d_{wake} + r_{wake} - R_L)(d_{wake} - r_{wake} + R_L)(d_{wake} + r_{wake} + R_L)} \tag{7.37}$$

7.6.2. Blade Element Flapping

Due to asymmetry of the velocity distribution there will also be an unequal distribution in lift between the advancing and retreating side of the rotor blade. The rotor blades are mounted to a hinge which allows the rotor blade to flap. The flapping motion can be considered as a periodic motion in forward flight and can therefore be expressed as a Fourier series. The flapping motion is given in Equation 7.38. Only the first three terms of the Fourier series will be considered since second and higher harmonic terms will have little influence on the rotor torque and thrust [17]. The first term in Equation 7.38 is the conning angle, the second term the longitudinal flapping angle and the last term is the lateral flapping angle and are given in Equations 7.40, 7.39 and 7.41 respectively [17].

$$\beta = a_0 - a_{1_s} cos(\psi) - b_{1_s} cos(\psi) \tag{7.38}$$

$$a_{1_s} = \frac{\mu}{1 - \frac{\mu^2}{2}}\left[\frac{8}{3}\theta_0 + 2\theta_1 + 2\left(\mu\alpha_s - \frac{v_1}{\Omega R}\right)\right] - \left(\frac{1 + \frac{3\mu^2}{2}}{1 - \frac{\mu^2}{2}}\right)B_1 \tag{7.39}$$

$$a_0 = \frac{3\rho acR}{m}\left(\theta_{avg}(1 + \mu^2) - \frac{4\lambda}{3}\right) \tag{7.40}$$

$$b_{1_s} = \frac{\frac{4}{3}\mu a_0 + \frac{v_1}{\Omega R}}{1 + \frac{\mu 2}{2}} + A_1 \tag{7.41}$$

θ_0 is the average pitch at the centre of rotation, θ_1 is the twist distribution, λ is the inflow ratio, μ the advance ratio of the rotor blade and m is the mass per unit span of the rotor blade. The lateral and longitudinal cyclic pitch coefficients are A_1 and B_1 respectively. Cyclic pitch is equivalent to flapping in such a way that changes in rotor conditions due to one degree of cyclic pitch have the same effect as one degree of change in flapping. However, this assumption is only valid to rotors with zero hinge offset, but proves to be sufficient to perform performance analysis of rotors with moderate hinge offsets[17].

7.6.3. Blade Element Angle of Attack

The pitch of a blade element, given in Equation 7.42, depends on the collective pitch θ_0, the pitch distribution θ_1 and the cyclic pitch θ_{cyc} [17]. Since the rotorcraft will be controlled by means of continuous trailing edge flaps (CTEF), there will no lateral control due to cyclic pitch. This means that the cyclic pitch must be equivalent to the change in c_l, c and c_d of the to CTEF. Therefore, it assumed that tilting the rotor disc in a particular direction has the same effect as deflecting the CTEF. For the current analysis it was decided to only determine the cyclic pitch coefficients and assume that the CTEF will have the same effect. This is justified by the fact that more focus is put on the required power at which the rotorcraft can fly between the hover stations, rather than what the aerodynamic influence of the CTEF is. Therefore, the pitch angle can still be written as a Fourier series. The lateral and longitudinal cyclic coefficients in this series are A_1 and B_1 respectively.

$$\theta = \theta_0 + \frac{r}{R}\theta_1 - A_1 cos\psi - B_1 sin\psi \tag{7.42}$$

The velocity U of a rotor blade section can be decomposed into a tangential U_T and perpendicular U_P velocity component. In Figure 7.13 a side view is given of a blade element with the aforementioned velocity components. The velocity component perpendicular to the leading edge U_T is the sum of the forward velocity of the rotorcraft and the rotational speed of the rotor blade at position r. From Equation 7.43 it can be seen that for $\psi \in [0°, 180°]$ the blade sees a higher velocity than for $\psi \in [180°, 360°]$ [17]. The velocity vector that is perpendicular to the the quarter chord line of the rotor blade and lies within the plane that contains the rotor shaft is U_P. This velocity vector depends on the component of the forward flight velocity parallel to the shaft $V\alpha_s$, the local induced velocity parallel to the shaft v_L and the blade flapping dynamics. Furthermore, there is also a spanwise velocity component U_R, which is due to the forward speed V. This velocity component is given in Figure 7.13.

$$U_T = \Omega r + V sin\psi \tag{7.43}$$

$$U_R = V cos(\psi) \tag{7.44}$$

$$\begin{aligned} U_P = V\alpha_s - v_1(1 + K\frac{r}{R}cos(\psi)) - V cos(\psi)(a_0 - a_{1_s}cos(\psi) - b_{1_s}cos(\psi)) \\ -\Omega R\frac{r}{R}(a_{1_s}sin(\psi) - b_{1_s}cos(\psi)) \end{aligned} \tag{7.45}$$

The local angle of attack is a function of azimuth and radial position of the rotor blade element. The equation for the angle of attack is given in Equation 7.46[17]. Furthermore, the angle of attack can be seen in Figure 7.13. The combination of cyclic pitch and flapping can be considered as the most primary variables in this equation. The sum of longitudinal rotor flapping and longitudinal cyclic pitch is given in Equation 7.47. This equation was derived by setting the rolling moment of the rotorcraft to zero. In this equation the inflow term is with respect to the tip path plane. The sum of lateral cyclic pitch and lateral rotor flapping is given in Equation 7.48. The equation for the lateral motion of the rotor blade was also derived, by setting the pitching moment equal to zero.

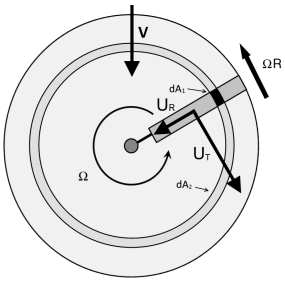

Figure 7.12: Rotor disk with tangential and radial velocity component[14]

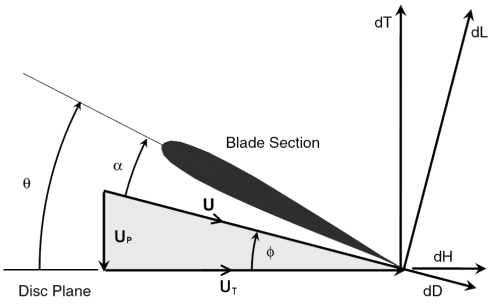

Figure 7.13: Blade section with the radial and tangential velocity components[14]

$$\alpha = \frac{1}{\frac{r}{R} + \mu sin(\psi)}\Bigg[\frac{r}{R}\left[\theta_0 + \theta_1\frac{r}{R} - (A_1 - b_{1_s})sin(\psi)\right] - \frac{v_1}{\Omega R}\left(1 + \frac{r}{R}cos(\psi)\right) + \mu\left[\alpha_{TPP} + \left(\theta_0 + \theta_1\frac{r}{R}sin(\psi) - a_0 cos(\psi) - (A_1 - b_{1_s})sin(\psi)cos(\psi) - (B_1 + a_{1_s})sin(\psi)^2\right)\right] \tag{7.46}$$

$$B_1 + a_{1_s} = \frac{\mu}{1 + 1.5\mu^2}\left(\frac{8}{3}\theta_0 + 2\theta_1 + 2\left(\mu\alpha_{TPP} - \frac{v_1}{\Omega R}\right)\right) \tag{7.47}$$

$$A_1 - b_{1_s} = -\frac{(\frac{4}{3}\mu a_0 + \frac{v_1}{\Omega R})}{1 + \frac{\mu^2}{2}} \tag{7.48}$$

7.6.4. Blade Element Force, Moment and Torque

In forward flight the rotorcraft shall produce a certain amount of thrust to compensate for the weight of the rotorcraft to maintain altitude. Furthermore, it also needs to counteract the H-forces and parasitic drag during steady forward flight. The thrust vector can be split up into a vertical and a horizontal component. Equation 7.49 gives the relation the thrust for N blades[17]. The total thrust of of the rotor blade is equal to the number of blades times the average lift per blade. Root and tip losses were taken into account for the calculation of the rotor thrust. The aforementioned losses were adjusted by the Prandtl correction factor. The horizontal force perpendicular to the rotor shaft is the H-force and can be calculated using Equation 7.50. The H-force is directed opposite to the direction of flight.

$$T = \frac{b\rho ac}{4\pi}\int_0^{2\pi}\int_0^R U_T^2\alpha dr d\psi \tag{7.49}$$

$$H = \frac{b}{4\pi}\int_0^{2\pi}\int_0^R \rho U^2 c c_L cos(\varphi) dr d\psi sin(\psi) + \frac{b}{4\pi}\int_0^{2\pi}\int_0^R \rho U^2 c c_D cos(\varphi) dr d\psi sin(\psi) \tag{7.50}$$

In Equations 7.52 and 7.53 the vertical and horizontal force equilibrium are given respectively. The parasitic drag of the rotorcraft can be considered small because the drag coefficient and equivalent flat area are small. For the subsequent analysis it was chosen to use the angle of attack of the tip path plane α_{TPP} as the reference angle. In Figure 7.14 a free body diagram of the rotorcraft in steady forward flight is given. The rolling moment of the rotorcraft can be calculated with Equation 7.51.

$$R = -\frac{b}{2\pi}\int_0^{2\pi}\int_0^R \frac{\rho}{2} a c U_T^2 \alpha r sin(\psi) dr d\psi \tag{7.51}$$

$$\sum F_y = (T_U + T_L)cos(\alpha_{TPP}) + (H_U + H_L)sin(\alpha_{TPP}) - W = 0 \tag{7.52}$$

$$\sum F_x = (T_U + T_L)sin(\alpha_{TPP}) - (H_U + H_L)cos(\alpha_{TPP}) - D_{par} = 0 \tag{7.53}$$

In order to determine what the rotor power in forward flight is, it is first necessary to determine what the torque per rotor blade is. The torque Q required in forward flight per rotor is given in Equation 7.54. The power follows from this by multiplying this equation with the rotational speed.

$$Q = \frac{b}{2\pi}\int_0^{2\pi}\int_0^1 r\frac{\rho}{2}U_T^2 cc_d dr d\psi - \frac{b}{2\pi}\int_0^{2\pi}\int_0^1 r\frac{\rho}{2}U_T^2 ca\alpha dr d\psi \tag{7.54}$$

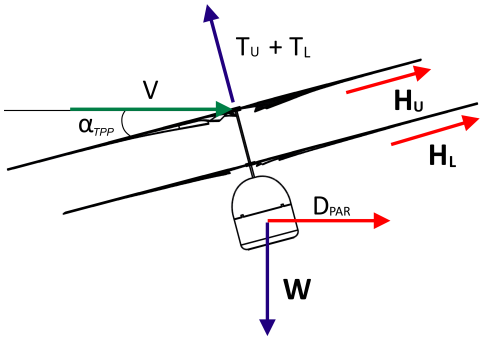

Figure 7.14: Free-body diagram of rotorcraft in forward flight

7.6.5. Discretisation of the Physical Problem

In order to perform calculations it was necessary to discretise the rotor disc. The discretisation was used to perform calculations in MATLAB. The rotor blade was analysed at 100 radial points over 3600 angular positions. These numbers were chosen such that the analysis would yield accurate results within the least amount of time. The segments were taken small such that the discretisation error is small and to assure convergence of the discretisation. The errors that arise due to termination of iterative procedures used to determine a numerical solution are taken for granted. Due to the small bisection limits the aforementioned error can be assumed to be small. In total there were six parameters which were adjusted during the forward flight analysis: Ω, θ_{upper}, θ_{lower}, A_1, B_1 and α_{TPP}. In order to iterate it was chosen to use recursive bisection to find the value of the iterable parameter. Intervals were chosen such that the iteration would converge. The iterating procedure with the in- and outputs are given in Figure 7.15. Apart from the given inputs, there is also a dependency on sea level conditions and rotor geometry.

7.6.6. Constraints Forward Flight Analysis

In order to determine relevant forward flight characteristics it is necessary to impose constraints on the numerical analysis. A total of six constraints were used to determine if the output values were valid. Hence there will only be a power output if the input variables yield output values that comply with all of the constraints. This corresponds with output **G** in Figure 7.15. On the other hand, if the output values do not comply with the constrains there will be a new iteration, which is denoted with output **F** in Figure 7.15.

- **Constraint 1 - Equal torque**
  One of the important constraints is that the torque of the upper and lower rotor must be the same in magnitude in order to avoid rotation of the rotorcraft. Such a rotation could result in the rotorcraft drifting away in forward flight, extending the flight distance between the hover stations. This would result in more jet fuel being consumed. Therefore $Q_{upper} = Q_{lower}$ must hold.
- **Constraint 2 - Force equilibrium**
  The rotorcraft shall perform steady horizontal flight, which means that the horizontal thrust components must cancel out the parasitic drag and the horizontal H-force components. Thus, Equation 7.53 must be incorporated in the conditions for forward flight. Furthermore, the forces in the vertical direction must also cancel each other out. Therefore Equation 7.52 must hold.
- **Constraint 3 - No rolling moment**
  Due to an unsymmetrical velocity and lift distribution, the upper and lower rotor can produce a rolling moment. Since both contra-rotating rotors are assumed to rotate at the same RPM they must cancel out the rolling moment. In steady forward flight the rotorcraft shall not create a rolling moment, hence $R_U + R_L = 0$.
- **Constraint 4 - Limitation power**
  The power in forward flight shall be less than for hover. The estimated power for hover is 517 kW.
- **Constraint 5 - Limit RPM**
  The rotational speed of the shaft shall stay within in allowable RPM range. This means it shall not go below 220 nor beyond 256 RPM.
- **Constraint 6 - Maximum angle of attack**
  The angle of attack shall not exceed the stall angle α_{stall}. The maximum angle of attack for the VR-12 is 17.5°[17]. Beyond this angle the rotor blade is unable to produce lift, hence it will stall.

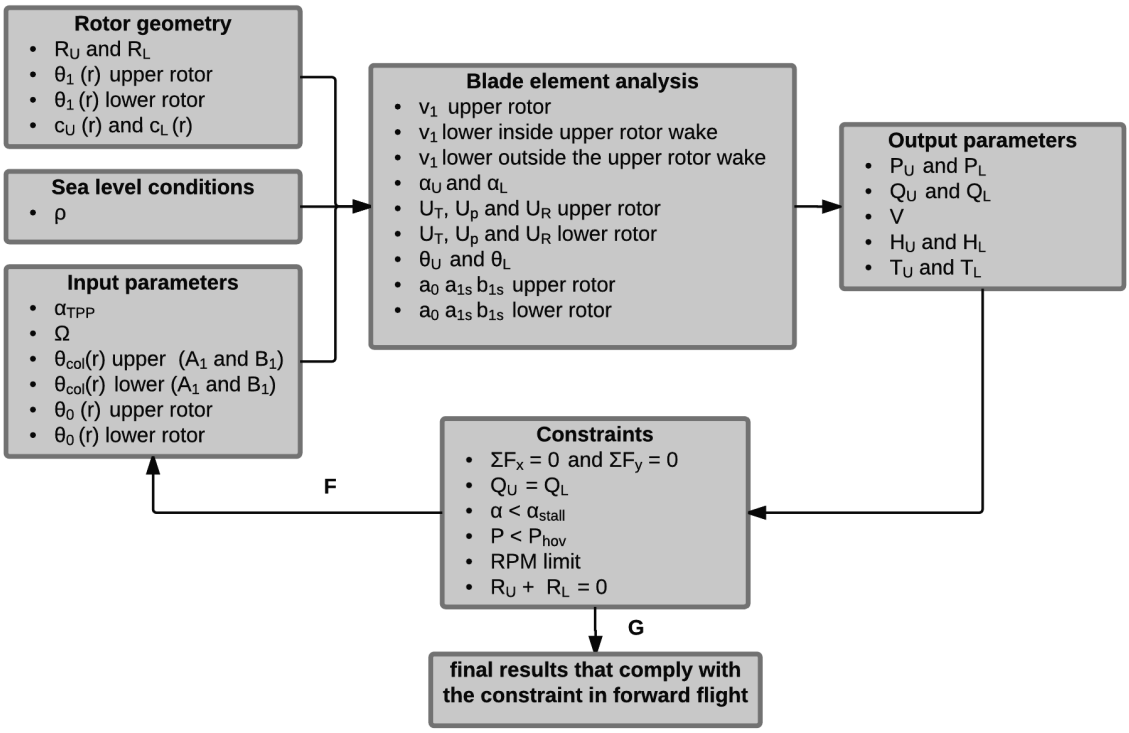

Figure 7.15: Iterating procedure

[17] URL http://www.airfoiltools.com/search/list?page=v [cited 20 January 2017]

7.6.7. Results Forward Flight

The results from the analysis for forward flight are given in Table 7.2. The purpose of this analysis is to estimate the power required in forward flight by means of Blade Element Momentum Theory (BEMT). Due to the unique design of the the rotor blade, which has high efficiency in hover, it is likely that it will have a lower efficiency in forward flight. Furthermore, it was also assumed that the forward flight segments will be executed first. The wake shift is such that a small part of the lower rotor is affected by the upper rotor wake. It can also be seen that the output values comply with the given constraints. Furthermore, the total power required in forward flight at MTOW will be around 361.8 kW.

	Description	Value		Description	Top	Bottom
g	Gravity	9.81 m/s^2	R	Rotor radius	8 m	8 m
W	Weight	49050 N	n_b	No. of blades	5	5
ρ	Air density	1.225 kg/m^3	μ	Advance ratio	0.21	0.21
R	Rotor radius	8 m	v_1	Induced velocity	1.81 m/s	2.4 m/s
C_{L_α}	Lift gradient	7.38 rad^{-1}	A_b	Blade area	8.15 m^2	7.00 m^2
A	Disk area	201 m^2	θ_0	Collective pitch	0.069 rad	0.065 rad
Ω	Rotational speed	13.79 rad/s	σ	Solidity Ratio	0.0405	0.0348
V	Air speed	25.11 m/s	γ	Lock No.	6.76	12.0
C_d	Drag coefficient	0.15	a_0	Coning angle	0.01 rad	0.01 rad
S_{body}	Flat plate area	3.15 m^2	H	H-force	2.26 kN	6.41 kN
α_{TPP}	Tip path angle	0.083 rad	T	Thrust	27.19 kN	21.24 kN
χ	Skew angle	1.41 rad	Q	Torque	13.12 kNm	13.12 kNm
d_{wake}	Wake shift	12.36 m	P_{fwd}	Forward power	180.89 kW	180.89 kW

Table 7.2: Input and output parameters during forward flight

7.7. Validation

In this section, the use of the model as represented in Figure 7.3, with the assumptions as explained in Section 7.4.1 will be validated. The main assumption this model is based on, is that the wake of the upper rotor has contracted fully when at the lower rotor. This assumption is supported by an experiment by Taylor[15]. The findings of this experiment show that the wake of a rotor contracts quickly, at a distance of 0.25 R below the rotor disk. That means that a vertical separation of 2 m would be sufficient to be able to assume full contraction.

Another way to validate the method is by checking whether the resulting ratio between thrust of the upper rotor and the thrust of the lower rotor complies with a theoretical value given in literature. This theoretical value is obtained from Leishman and Ananthan[16], who derived the relations shown in Equations 7.55 and 7.56. These relations are valid for the used case, described in Section 7.4.1.

$$v_l = 0.4375 v_u \tag{7.55}$$

$$T_u v_u = T_l (v_u + v_l) \tag{7.56}$$

Rearranging these equations gives Equation 7.57, the theoretical ratio between upper and lower rotor disk thrust. The resulting ratio $\frac{T_u}{T_l}$ equals 1.4476, which is close to the theoretical value.

$$\frac{T_u}{T_l} = 1.4375 \tag{7.57}$$

8 Structural Design

The current chapter represents the structural design of the rotorcraft. Firstly, the general analysis method will be discussed in Section 8.1. The design of the rotor blades is discussed in Section 8.2 and Section 8.3 elaborates on the design of the overall structure as well as the material used and the implemented reinforcements and supports. This is followed by the hub and shaft design, discussed in Section 8.4. Lastly, the production plan will be presented in Section 8.5.

8.1. General Method for Analysing

It should be noted that within the limited time available, producing a Finite Element Analysis (FEA) model was not considered the best option, due to the fact that it would have had to be strongly simplified. Thus, it was decided to make use of an off-the-shelf FEA model, more specifically, Fusion 360, which is one of the Autodesk software and is using the validated Nastran code for finite element analysis.

Next to this, the material properties provided by the program have been validated by comparing the properties for some representative materials. Tables 8.1 and 8.2 lists some of the properties and the discrepancies between them.

Table 8.1: Material properties verification for Aluminium 7075

Property	*Fusion* 360	*Callister*[18]	Difference [%]
Density $[g/cm^3]$	2.8	2.8	0
E $[GPa]$	71.3	71.3	0
σ_{yield} $[MPa]$	442	505	12

It can be seen that only a small deviation in yield stress for aluminium is present, which might be due to the variations in the alloy. However, as Fusion 360 gives more conservative values, it is assumed that it is safe to use the specified properties.

Table 8.2: Material properties verification for Carbon Fiber Reinforced Polymer

Property	*Fusion* 360	*Callister*[18]	Difference [%]
Density $[g/cm^3]$	1.4	1.7	17
E $[GPa]$	133	112	19
σ_{max} $[MPa]$	577	875.5	34

It is realised that the strength of the composite material depends on the orientation and volume of the fibres and this can be the reason behind having this big of discrepancies. However, here again the values provided by Fusion 360 are on the conservative side, thus, in order to keep the analysis consistent, it has been decided that the material properties are not going to be varied from the ones already provided[18].

Next to this the calculation methods are going to be verified using simple beam theory in order to show that the program can produce accurate results when it comes to static stresses. Aluminium is going to be the used material for the verification with the specified characteristics as described in Table 8.1. Figure 8.1 gives an overview of the studied loadings.

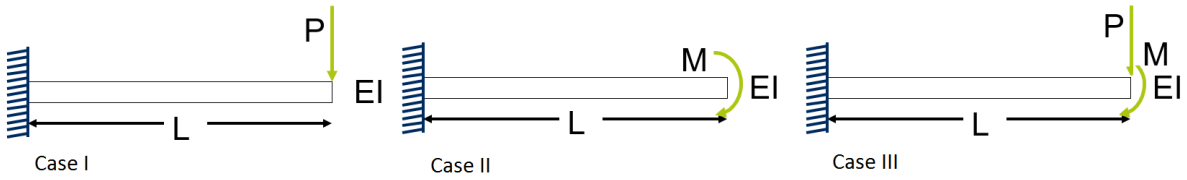

Figure 8.1: Beam loadings[19]

Moreover, Equations 8.1 , 8.2 and 8.3 are used for the calculation of the values for Case I, Case II and Case III, respectively[19].

$$\delta_1 = \frac{PL^3}{3EI} \qquad (8.1) \qquad \delta_2 = \frac{ML^2}{2EI} \qquad (8.2) \qquad \delta_3 = \delta_1 + \delta_2 \qquad (8.3)$$

Additionally, it should be noted that the program has different meshing sizes and a comparison between the accuracy of each of them is given. The results are provided in Table 8.3.

Table 8.3: Calculation verification of *Fusion* 360

	Analytical	*Fusion* 360 10 %	*Fusion* 360 5 %	*Fusion* 360 2 %	Max Difference [%]	Min Difference [%]
δ_1 $[mm]$	0.866	0.853	0.859	0.866	1.5	0
δ_2 $[mm]$	1.298	1.288	1.291	1.298	0.770	0
δ_3 $[mm]$	2.164	2.139	2.153	2.163	1.1	0.05

It can be observed that the results are extremely close to the one obtained with the analytical approach. The discrepancies converge to the expected value with decreasing the mesh size, thus it is expected that *Fusion* 360 will provide with accurate results.

8.2. Blade Design

In this section the analysis and design of the rotor blade will be discussed. The helicopter blade encounters different forces during flight. Lift is produced in the out-of-plane direction upwards. Drag is produced in the in-plane direction opposed the rotation. Due to the rotation the blade also encounters a centrifugal force along the radius. These forces are in balance with each other under a certain coning angle, allowed by the flapping hinge at the root of the blade.

8.2.1. Load Cases

The rotor blade will encounter varying load conditions during its operational life. The mission profile encompasses a high endurance and thus a large weight variation. Because of this, the rotational speed of the rotors will also vary during the mission.

The load case that will be used for design is the case of hover with maximum weight and RPM. Due to the maximum weight, the highest lift forces will be introduced on the blades, and due to the rotational speed the largest centrifugal forces will be felt by the blades.

Besides this design condition, other conditions also need to be taken into account. At the end of the mission, the rotor will encounter lower RPM. The moment balancing for the mission duration should also be checked.

Also, at landing, a higher gravity force will be induced on the rotorcraft, and thus also on the blades. The blades need to withstand these forces without failing.

Finally, due to the Continuous Trailing Edge Flaps (CTEF), which will be further elaborated in Chapter 9, the rotor blade will need to be able to deal with the extra torque forces induced by them.

8.2.2. Structural Components

In Chapter 7 the airfoil and its chord distribution were discussed. The airfoil was determined to be the Boeing VTOL VR-12. These characteristics impose the restrictions on the blade structure design to design the components of the blade.

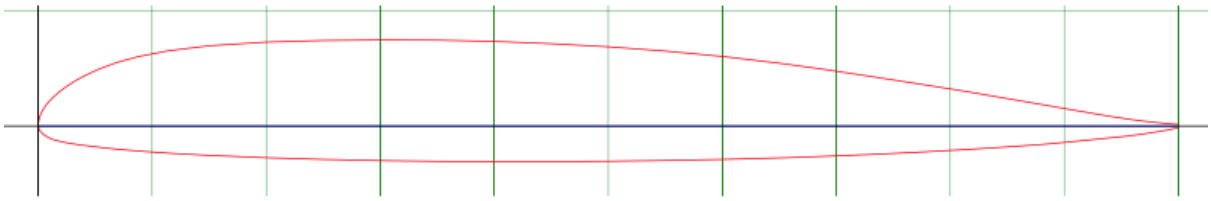

Figure 8.2: Outline of Boeing VTOL VR-12 airfoil[18]

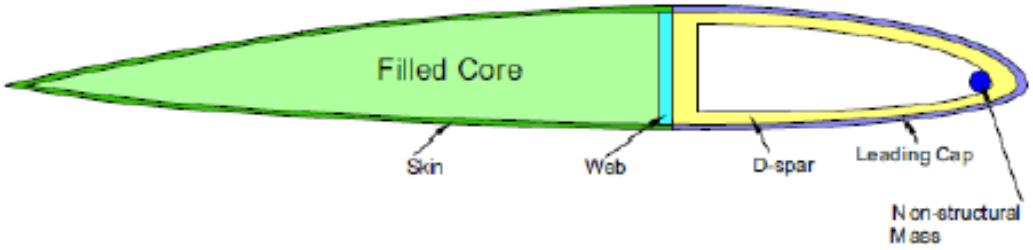

Figure 8.3: Cross section of conventional rotor blade[20]

The shape of the VR-12 can be seen in Figure 8.2. Conventional rotor blades have a cross section as can be seen in Figure 8.3. They consist of the outer skin, a D-spar, a vertical web, foam filling the cavities to provide some extra stiffness to the blade and in some cases extra non structural mass is added to the blade. For our analysis and design, the layout was simplified to a rotor blade consisting of a outer skin and a structural D-spar. The vertical web of the D-spar is chosen to be at the position of largest airfoil thickness.

For the analysis, the D-spar was assumed to be the main load carrying component, and so the structural analysis was done for that component only.

The rotor blade was sectioned into four parts along the rotor radius for the design, to adjust the thicknesses of the spar along the span of the blade on each of these sections. Taking the root cutout into account, the sections are as follows:

Root cutout:	$0 \leq R \leq 1$ $[m]$
Section 1:	$1 < R \leq 2$ $[m]$
Section 2:	$2 < R \leq 4$ $[m]$
Section 3:	$4 < R \leq 6$ $[m]$
Section 4:	$6 < R \leq 8$ $[m]$

[18] URL http://airfoiltools.com/plotter/index/?airfoil=vr12-il [cited 23 January 2017]

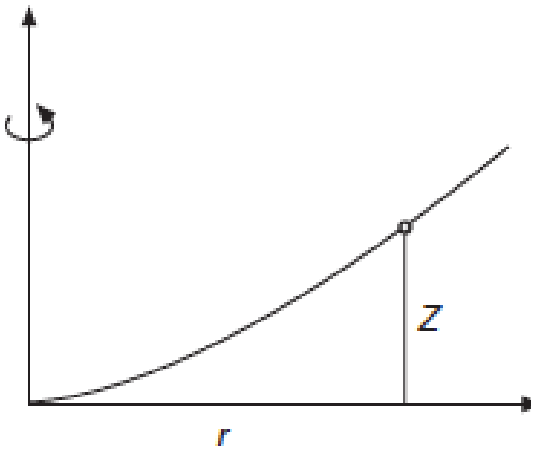

(a) z Location of the rotor blade[21]

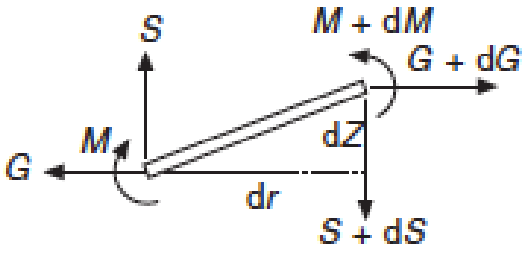

(b) Equilibrium of blade segment[21]

The upper and lower rotor use the same airfoil, however they have significant different sizes, as was explained in Chapter 7. The chord length distribution is also very different across the radius. Therefore, a separate analysis was done for the upper and lower blades. The two rotor disks have a vertical separation of two meters. As a safety factor the rotor blades are set to have a maximum out-of-plane deflection of one meter. The blade material is set to be Carbon Fibre Reinforced Polymer (CFRP), because of its high specific strength and stiffness.

The cavities of the D-spar is filled with Compaxx 900-X structural foam. This structural foam has a low density at 60 kg/m^3, and a yield stress of 1.35 MPa; in tension[19]. The cavity behind the D-spar is filled with a honeycomb structure, to aid in the transferring the loads from the CTEF control surfaces to the structural D-spar member.

8.2.3. Out of Plane Forces and Motion

The out of plane motion of the rotor blade is defined as the vertical movement of the blade. This motion is known as the flapping motion of the rotor blade. Let z be the vertical displacement of the rotor blade at a certain position r along its radius.

The forces and moment equilibrium are then as shown in Figures 8.4a and 8.4b. For the in-plane forces, the equilibrium gives us expression 8.4 for the centrifugal force experienced by the rotor blade. For the out of plane forces and moment experienced by the blade, the moments and shear forces were also taken from the equilibrium and are expressed by Equations 8.5 and 8.6, respectively.

$$G = \int_r^R m\Omega^2 r dr \qquad (8.4) \qquad dS + mdr\frac{\partial^2 z}{\partial t^2} = 0 \qquad (8.5) \qquad Gdz + Sdr - dM = 0 \qquad (8.6)$$

Differentiating Equation 8.6 and inserting into Equation 8.5 gives one expression for the moment in the blade. Using the elementary bending equation gives the final expression for the moment in the beam[21].

$$\frac{\partial^2}{\partial r^2}\left(EI\frac{\partial^2 z}{\partial r^2}\right) - \frac{\partial}{\partial r}\left(G\frac{\partial z}{\partial r}\right) + m\frac{\partial^2 z}{\partial t^2} = 0 \qquad (8.7)$$

[19] URL http://www.dow.com/en-us/markets-and-solutions/products/compaxx/compaxx900xstructuralfoam/ [cited 23 January 2017]

Using appropriate boundary conditions for the hinged blade will give the final expression for the moment in the blade. The z position for the blade is then the balance between the moment by the outward centrifugal force and the lift force acting on the blade.

For a detailed analysis, the analysis becomes increasingly complex and very time consuming. Therefore, it was chosen to make a CATIA model of the blades, and implement these in a FEA software program. Autodesk Fusion360 was used for this. This program allows forces and rotational velocities to be applied to a body imported from CATIA, and then computes the static stresses and deflections on the body. Both complex and simplified CATIA models were made of the blade, and the results were compared. The variation of the analysis was small, but the computation time and mesh error were greatly reduced by using the simplified CATIA model.

As a check to the program, simplified forces, velocities and deflections were also computed in separate models in the program, and checked with MATLAB scripts implementing the simplified situations. The Fusion360 software gave corresponding values for these simplified cases, and thus was deemed verified. However, after quite some time computing the combined effects, the results gave seemingly erroneous results, with tip deflections under lift force and rotation to be 38 m upwards.

Because of this, it was eventually chosen to go back to Equation 8.7. This formula was simplified significantly by making a static analysis, and thus neglecting the dynamic damping component and assuming the blade z position does not change in time. Also, to simplify the moment calculation in the blade, for the analysis it was assumed the blade was clamped at the root. The simplifications were necessary to achieve a design within the limited time. The simplified equation was then implemented in MATLAB to give the internal moments and resulting z position for the upper and lower blade. The MATLAB script that was used was verified by implementing simplified situations, as described in Section 8.1, for which the results are known. A initial value for the z location of the blade was needed for iterations. The initial values were obtained by determining the z location when the resulting moment from the lift and centrifugal force around the root attachment is zero. An initial thickness was given to the blade D-spar structure, and stresses and displacements were then checked for failure or exceeding the set displacement limits. The results will be discussed in Section 8.2.6.

8.2.4. In-Plane Forces and Motion

Besides the out-of-plane forces and displacements, there are also in-plane forces and displacements. The C_m of the VR-12 airfoil produces a torque on the airfoil. The induced torque was determined by the aerodynamics department by integrating the torque along its radius. For a conservative result, the computed torque of 200 Nm is then applied at the tip of the blade for the analysis. The CFRP has a high shear modulus of 47 GPa, and with the enclosed area of the D-spar with set thicknesses from the previous design steps, the rotation angle along the radius of the blade was determined using Equation 8.8[22], where G is the shear modulus, t is the material thickness, q is the shear flow and A is the enclosed area. Discretely integrating the equation over the several sections with different thicknesses and enclosed areas, the angle of twist at the tip was determined to be 0.33^o. According to the aerodynamics department, this was a reasonable value and so the design was not altered.

$$\frac{d\theta}{dr} = \frac{1}{2A} \oint \frac{q}{tG} ds \tag{8.8}$$

As discussed later in Chapter 9, CTEF are used for control of the rotorcraft. These flaps do not induce a pitching moment to the blade to obtain a pitch angle, such as the KAMAN K-Max intermeshing helicopter[20], but rather the CTEF adjust the blade aerodynamic characteristics and no blade twist is allowed. The skin near the trailing edge should then be able to adjust its shape, therefore the skin was not taken into account when doing the structural design for the blade. The loads induced by the CTEF

[20] URL http://www.helis.com/howflies/servo.php [cited 25 January 2017]

should be able to be transferred to the spar, for this the CTEF are attached to the honeycomb core. The CTEF is located at 70% of the rotor radius, and extends up to 95% of the rotor radius. The CTEF gives a maximum C_m increase of 0.05 at the deflection of the trailing edge set for control[23]. With this δC_m the torque change was computed and using the same approach as above with Equation 8.8. This leads to an increase in angle of twist of 0.2^o. This was considered reasonable, and so the design was again not altered.

Analogous to the analysis in Section 8.2.3 the forces and moments in the rotational plane are considered. As the rotor disks rotate, drag is also induced on the blades. this drag creates a moment around the root attachment, which is counteracted by the centrifugal force. The magnitude of the in-plane forces were obtained form the aerodynamics department, and a analogous analysis was used as described in 8.2.3. The final result is found in Section 8.2.6.

8.2.5. Root Attachment

The root cut-out was determined to be one meter. The structural D-spar member cross section changed over into a simple circular cross section with a radius of 6 cm. The blade is then attached to the hub via the hinge. This hinge is designed to have rotational freedom in the vertical and horizontal direction, known as the flapping and lead/lag hinge. The flapping hinge will have a rotational spring, to control the flapping motion. The design of this spring however, is considered outside the scope of this report due to time constraints. The rotational movement of the blade, or feathering motion, is restricted. This is explained briefly in Section 8.2.4, and will be elaborated in Chapter 9.

The lead/lag hinge in conventional design is provided with a lead/lag damper to dampen the lead/lag motion of the blades under motion. As described in Section 8.2.7 the critical frequencies are avoided, however the damper might still prove to be of value. Similar to the torsional spring in the flapping hinge, due to the time constraints this was considered outside the scope of this report.

8.2.6. Final Blade Design

The final blade consist of the D-spar with varying thickness along the radius. For both the upper and lower rotors, non-structural mass was added at the tips to increase the centrifugal force at the tips. This was done to reduce the tip deflection of the rotors, to stay within the set maximum tip deflection of one meter. At the root cut out, the blades are attached with a smooth structure made of the same material as the blades, CFRP. The weights of the blades were obtained by measuring the CATIA models. An assumption then needed to be made for the added weight of the the CTEF control surfaces. The CTEF control system is still experimental, so the assumption is made that the total implemented system weighs 40 kg, this is assumed to be evenly distributed over the blades. This weights assumption comes from the Honeycomb structure that is added, rounded to the nearest number, giving its experimental nature. For both rotors, the designs are described in Tables 8.4 and 8.5 for the lower and upper rotor respectively.

Table 8.4: Design lower rotor

		Section 1	Section 2	Section 3	Section 4	
Chord	$[mm]$	200	200	200	200	
Spar width	$[mm]$	48	48	48	48	
Spar height	$[mm]$	18	18	18	18	
Thickness	$[mm]$	7	7	3	1	
Added non-structural mass	$[kg/m]$	-	-	5.52	6.95	
Final weight rotor blade	$[kg]$					23.7

Table 8.5: Design upper rotor

		Section 1	Section 2	Section 3	Section 4	
Chord	$[mm]$	500	240	160	120	
Spar width	$[mm]$	125	60	40	30	
Spar height	$[mm]$	50	24	16	12	
Thickness	$[mm]$	4	3	2	1	
Added non-structural mass	$[kg/m]$	-	-	6.85	8.46	
Final weight rotor blade	$[kg]$					47.3

The thicknesses as described in Tables 8.4 and 8.5 lead to the final mass of the rotor blades out-of-plane deflections which can be seen in Figures 8.5 and 8.6 respectively.

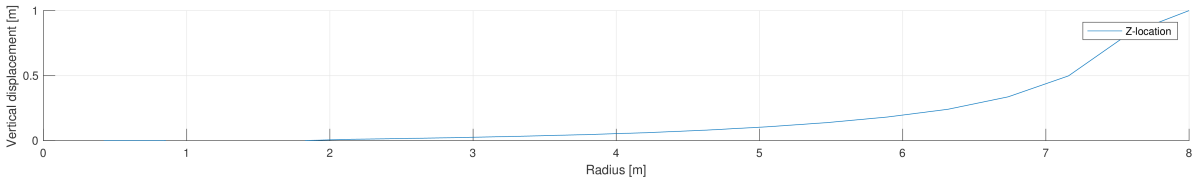

Figure 8.5: Upwards deflection of upper rotor

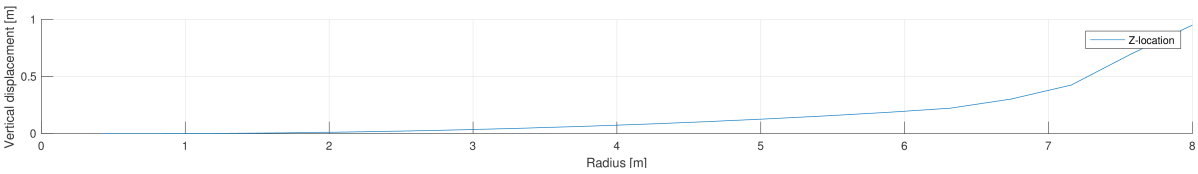

Figure 8.6: Upward deflection of lower rotor

To reflect on the load cases that need to be inspected, the loads at maximum RPM and maximum lift were the design conditions, and the thicknesses were decided accordingly. As the RPM reduces, the lift reduces simultaneously. The begin and end conditions were checked for the moment balancing, which both complied with the maximum deflection requirement. However, the intermediate conditions were not checked. As both centrifugal force and lift are relative to the rotational speed squared, the assumption was made that the moment balance would not vary heavily. The moment due to gravity is not yet into account for this analysis, as the magnitude of this moment is relatively small compared to the lift and centrifugal moments. As the gravitational moment does not change with rotational speed, for further analysis would be advisable to take that into account.

Under landing conditions, a acceleration of 1.5 g is assumed. Since the blades are fairly symmetric with respect to the horizontal axis, the downwards maximum loading the blade can cope with is considered fairly similar to the maximum upwards loading. At landing conditions though, the weight of the rotorcraft is greatly reduced due to fuel used and the loads will be much lower than at maximum weight. Therefore. the maximum loading capability for landing conditions is considered sufficient.

8.2.7. Resonance Frequencies

Next to the forces and moments that it needs to be able to handle, the resonance frequencies of the blade are also very important. For a rotor disk, there is an advancing and a retreating blade with respect to the wind. This means that every revolution of the rotor disk, the blade will encounter a cycle in lift and drag force. It is very important to avoid the eigenfrequencies of the blade during flight to avoid resonance in the blade, to avoid high amplitude reactions, which may cause the blade to break. The

rotating eigenfrequencies can be computed from the following equations, where γ_i is the eigenmode of the blade[21].

$$\omega_i^2 = \omega_{nr}^2 + \alpha_i \Omega^2 \tag{8.9}$$

$$\alpha_i = \frac{\int_0^1 mz \int_0^z \left(\frac{d\gamma_i}{dz}\right)^2 dzdz}{\int m\gamma_i^2 dz} \tag{8.10}$$

These eigenmodes need to be assumed fairly close to the actual eigenmode to get reliable results from this analysis. It is because of this assumption that it was decided to use the FEA software again. Autodesk Fusion360 can compute the eigenfrequencies for different eigenmodes for a structure, taking into account the rotation speed. The CATIA model of the blades were implemented into the software, and the eigenfrequencies were plotted into Campbell diagrams. Figures 8.9 and 8.10 show the Campbell diagrams for the upper and lower rotor, respectively. In the figures, several eigenmodes are shown. The modes represent different vibratory modes for flapping, lead/lag motion and torsional. The higher modes (four and above) are higher order modes of the flapping, lead/lag and torsional motion. An illustration of these vibratory modes can be found in Figures 8.7 and 8.8.

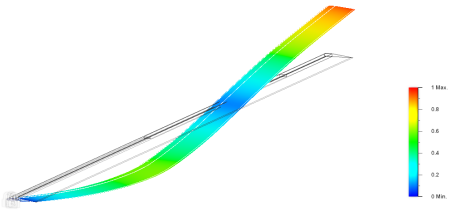

Figure 8.7: Flap eigenmode of lower rotor, second order vertical

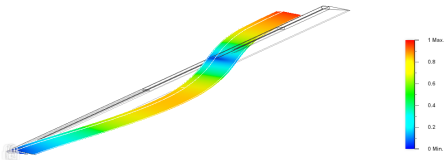

Figure 8.8: Lead/lag eigenmode of lower rotor, second order horizontal

The thick lines in the Campbell diagrams represent the frequencies where the rotation speed coincides with the eigenfrequency of the blades. Higher order lines were also included. For example, for the second order, the rotor would have vibrated twice during one rotation. The resonance effects are then lower, however might still cause problems. When this line would intersect the eigenmode lines, then at that rotation speed the rotor blades would experience resonance. The Fusion360 software computed the first eight modes of the blade, however the modes above the second order vibrate at very high frequency. In Figures 8.10 and 8.9 the Campbell diagrams are shown including the first three modes of the blades, and the lines representing the first four orders of resonance.

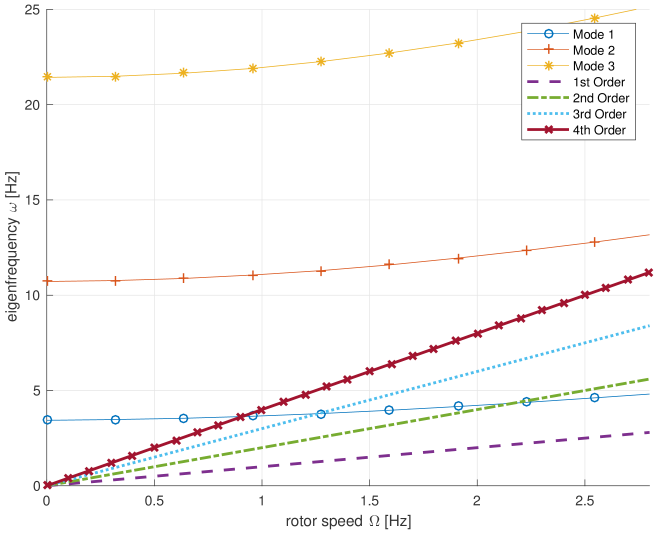

Figure 8.9: Campbell diagram of upper rotor blade

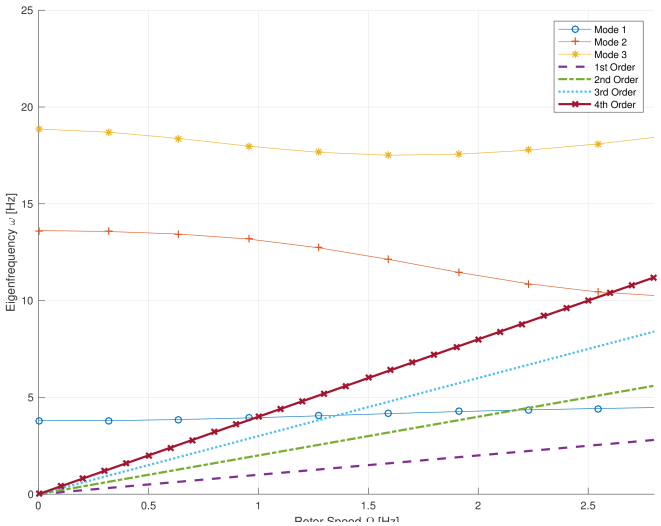

Figure 8.10: Campbell diagram of lower rotor blade

From the Campbell diagrams, several intersections can be seen between the lines. The operational rotation speed of the rotor disks lies from 2.78 Hz and 1.65 Hz. Within this range there are three intersections visible:

Rotor disk	frequency $[Hz]$	RPM		
Upper	2.17	130.2	2^{nd} order	1^{st} mode
Lower	2.17	130.2	2^{nd} order	1^{st} mode
Lower	2.6	156	4^{th} order	2^{nd} mode

This analysis thus shows two RPMs to avoid, 130.2 RPM and 156 RPM. The engine is capable of rapidly skipping these RPM to avoid resonance problems. However, enough lift still needs to be produced. When skipping over these RPMs, the lift produced at that moment is less than the weight of the rotorcraft. To solve this problem, the CTEF are used. The CTEF are capable to provide enough extra thrust when deflected to produced enough thrust to remain airborne[24].

8.2.8. Fatigue

The rotorcraft mission states that is must be in hover. Under perfect hover conditions, the blades will experience no change in velocity during its rotation. However, at any wind speed the blade will go through a velocity change, and thus a load cycle per rotation. Thus a fatigue analysis needs to be done. The material for the rotor blades structural member, the D-spar, is CFRP, which behaves very different under fatigue loading than metals, due to its inhomogeneous and anisotropic characteristics. As an illustration to this fact, in Figure 8.11 the cycles to failure are compared to metals frequently used in aerospace.

The understanding is that the fatigue life of CFRP is mainly dependent on the working environment and the damage modes experienced by the structure[25]. Also, CFRP has the tendency to absorb moisture over its lifetime, reducing its yield stress. This however, is of less importance to the current design, as the operational life is set for 24 hours, and no significant moisture absorption is present in this time span[25].

Low velocity impacts are very important to analyse for the CFRP structure. Even at low velocity, the impact can break fibres, and this damage can easily propagate through the structure. As this damage is

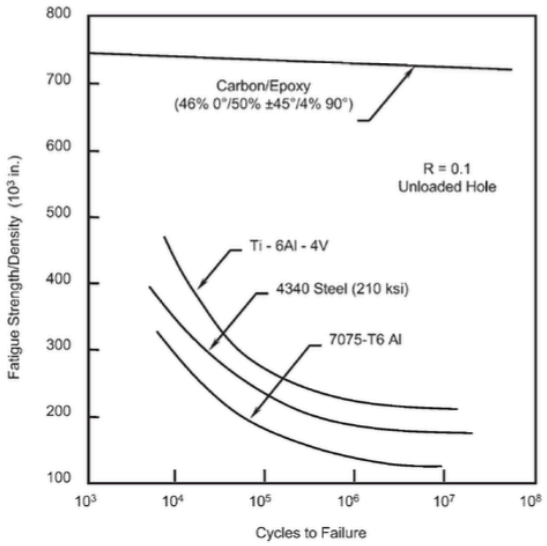

Figure 8.11: Comparison of fatigue life for Carbon Epoxy and metals frequently used in aerospace

often difficult to see from the exterior, it is hard to predict the actual damage. Fibre fractures, matrix failures and delamination can be the result of this, with structure failure as a consequence. High quality during the manufacturing needs to be ensured so no damage exist at beginning of life[25]. During the operational life, damage due to low velocity impact needs to be avoided where possible. For conventional rotor blades, the leading edge of the blades are sometimes covered with a titanium laminate to prevent erosion damage. However for our design, due to the low mission duration, it was opted not to do this.

The ideal case would be to have the traditional S-N curves to evaluate the fatigue lifetime with respect to the load cycles experienced by the rotorcraft. However, this is not so straightforward for composite materials. The frequency of loading is not taken into account for the S-N curve, while this does have an influence on the fatigue life of a structure. As a result, an experimental obtained S-N curve could prove reliable for a certain structure, but unreliable for another. Because of this, the engineering approach is to design with a sufficient safety factor[25].

8.3. Fuselage Design

This section covers the design of the fuselage of the rotorcraft. Included here are the structural elements below the rotor blades, hubs and shafts, since those are covered in seperate chapters.

Firstly, the choice between a monococoque, semi-monocoque and spaceframe structure needed to be made. In order to do this, the different loads on the system were studied. It was concluded that the main loads are due to the thrust produced by the rotors, the weight of the subsystems, including the structure itself, and the loading due to vibrations imposed by the rotors and engine. Furthermore, as weight is considered of high importance, the option which is expected to result in the lowest weight is chosen. The part which connects the rotor axes to the airframe is the main gearbox housing, which includes the PCVT and some bevel gears. Inside the gearbox, a thrust bearing is used to transfer the forces of the rotating shaft to the non-rotating gearbox housing. The rest of the airframe is connected to this gearbox housing. Since all the subsystems transfer their weights to the frame at discrete locations, their attachment points, a space frame structure ended up being the lightest option for the airframe. This choice was reinforced by the fact that no pressurization is necessary and no large aerodynamic forces act on the fuselage, which often are reasons for incorporating a load carrying skin structure in aircraft. The low aerodynamic forces are due to the large root cut-out area with respect to the fuselage top-view

area, as well as the low forward flight velocities and the low flight times (see Sections 7.4.2 and 11.2).

It was quickly found that the fuel tank needed to be in line with the main rotor shafts. Because of the large change in mass during the mission due to fuel consumption, there would be a balancing problem if the tank is not aligned with the rotor axes. The most straightforward solution is to hang the tank at the bottom of the rotorcraft, due to its large dimensions. The lightest solution was to make the tank a monocoque structure which is attached to the bottom of the spaceframe, instead of positioning a thin tank inside a frame structure. This way, the tank doubles as landing gear. The specific tank design is further elaborated upon in Section 8.3.3. The basic fuselage layout, including the fuel tank, frame and main gearbox, is presented in Figure 8.12.

Figure 8.12: Airframe structure layout

8.3.1. Cross Sectional Design

After determining the airframe layout, the cross section of the beams used in the frame needed to be determined. Different possibilities were evaluated. Firstly, the limiting characteristics of the cross section were outlined. As mentioned before, the expected loading of the structure includes normal stress but also high imposed vibrations.

Average normal stress is expressed by Equation 8.11. It can be observed that, if we assume that the load F is kept constant, the higher the cross sectional area A, the lower would be the stress σ. However, increasing the area is expected to result in higher weight. Thus, a balance needs to be found.

$$\sigma = \frac{F}{A} \tag{8.11}$$

Next to this, the vibrational loading needs to be taken into account. Typically, the structure is then represented as a number of point masses with the connecting items modelled as springs with specific spring constants. As discussed in the course of Vibrations AE2135-II by Sergio Turteltaub[26], the spring constant for a continuous axially loaded beam is given by Expression 8.12, where E is the Young's Modulus and L is the beam's length. Here it can still be observed that having a large cross sectional area is beneficial for increasing the stiffness of the beam. This will lead to better load carrying capabilities of the structure, however, again at the price of higher weight. Next to this, smaller length of the spring leads to an increase in stiffness. Thus, shorter beams are going to contribute positively to loads carrying capabilities. Therefore, a optimal packaging of the subsystems inside the structure is essential. This will be discussed more in depth later on.

$$k = \frac{E \cdot A}{L} \tag{8.12}$$

In order to get a more in-depth analysis on the structural vibration and how could this be improved, Aircraft Structures for Engineering Students by T.H.G. Megson was consulted[22]. The analysis performed there for a general case starts with a studying the oscillation of a mass/spring system, as illustrated in Figure 8.13. Determining the normal modes and frequencies for a general spring/mass system requires solving a system of second-order differential equations, which will provide the phase and amplitude of each mode of vibration. Using the flexibility or force method, this systems is expressed by Equation 8.13, where m_j represents each discrete mass, x_i is the displacement of the i^{th} item and δ_{ij} is the displacement at the point i due to a unit load at a point j.

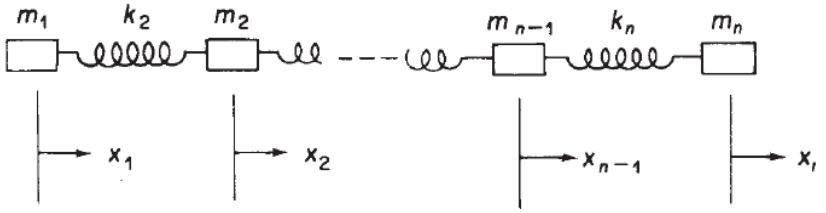

Figure 8.13: Spring system

$$\sum_{j=1}^{n} m_j \ddot{x_j} \delta_{ij} + x_i = 0 \quad (for \quad i = 1, 2, ..., n) \tag{8.13}$$

Consequently, by using the unit load method the flexibility coefficients δ_{ij} can be evaluated and expressed by Equation 8.16. The displacement x_i is linearly proportional to the harmonic motion w, given by Equation 8.14. However, square of w is inversely proportional to the flexibility coefficient δ, given by Equation 8.15. Based on this, it was realised that, in order to keep the deflection of the beams loaded by vibrations low, it is required that the cross sections has a high MOI.

$$x_i = x^{(i-1)} \cdot sin(wt + \zeta) \tag{8.14}$$

$$w^2 = \frac{1}{m\delta} \tag{8.15}$$

$$\delta_{ij} = \int_L \frac{M_i M_j}{EI} dz \tag{8.16}$$

Keeping in mind the normal stress and vibrational loading as well as the weight, it was concluded that the optimal cross section of the truss beams would have a high MOI and a cross sectional area, which allows to cope with normal stresses, but does not exceed the minimum required, in order to optimise for weight. Several possibilities were studied, the most beneficial ones being a circular, a square and a rectangular one. It was decided to compare the three possibilities by keeping the same area and aim for the highest moment of inertia (MOI). The corresponding MOIs for the three options are expressed by Equations 8.17, 8.18 and 8.19 and 8.20, respectively, where r_i is the inner radius of the circular tube, t is the thickness of the cross section, a is the length of the outer side of the square and b and c are the corresponding lengths of the rectangular beam, where $b = 2 \cdot c$ has been considered. It should be noted that the MOI for both x and y directions of the rectangle were evaluated.

$$I_{circ} = \frac{\pi}{4} \cdot \left((r_i + t)^4 - ri^4 \right) \tag{8.17}$$

$$I_{sq} = \frac{a^4}{12} - \frac{(a - 2t)^4}{12} \tag{8.18}$$

$$I_{rect_x} = \frac{b \cdot c^3}{12} - \frac{(b - 2t) \cdot (c - 2t)^3}{12} \tag{8.19}$$

$$I_{rect_y} = \frac{c \cdot b^3}{12} - \frac{(c - 2t) \cdot (b - 2t)^3}{12} \tag{8.20}$$

With a fixed value for the area and thickness of $A = 5E - 05\ m^2$ and $t = 2E - 3\ m$ the calculations resulted in $I_{circ} = 8.1E - 10\ m^4$, $I_{sq} = 1.3E - 10\ m^4$, $I_{sq} = 1.3E - 10\ m^4$, $I_{rect_x} = 1.9E - 10\ m^4$, $I_{rect_y} = 5.0E - 11\ m^4$. Thus, due to its highest MOI value in both directions, for the same cross sectional

area, the circular tube is considered the optimal choice that will provide good performance regarding vibrations at the lowest possible weight.

8.3.2. Airframe

The main loads that act on the space frame are due to the fuel tank and fuel weight at the bottom, the rotor thrust at the top and the other subsystem weights at different locations close to or inside the frame. As seen in Figure 8.12, the frame is somewhat pyramid shaped, with the engine, being a large component, housed inside.

The Autodesk Fusion 360 software was used to perform a structural FEA on the airframe and fuel tank. Since structural vibration analysis of the complete rotorcraft, including the engine, rotors and Auxiliary Power Unit (APU), was deemed beyond the scope of this project, a safety factor of at least 2 was used for the design of the fuselage elements in order to compensate for this. It is recognised that this method yields results which deviate from reality, so it is included as one of the technical risks presented in Section 10.4.

The forces applied to the frame - essentially the weights of different components - are multiplied by 1.5 to represent a $1.5g$ manoeuvre in order to comply with the requirements. Different sized round tubes made from CFRP (see Section 8.3.4) are chosen. The main load carrying members, running diagonal between the tank and the gearbox, have an outer diameter of 40 mm with a wall thickness of 4 mm. The frame has a weight of 21.3 kg. Because the frame is very dependant on the other subsystems that it houses, the weight used for performance analysis is 30 kg in order to have some margin for further design.

Figure 8.14 shows a visualisation of the results of the finite element analysis performed by the Fusion 360 software. The legend represents the range of stresses the frame encounters, in MPa. The results show that with a maximum stress of 122 MPa the safety factor is 2.46, assuming the material failure stress of 300 MPa as given in the program. As explained in Section 8.1, the isotropic assumption is accepted here because the failure stress value is on the conservative side.

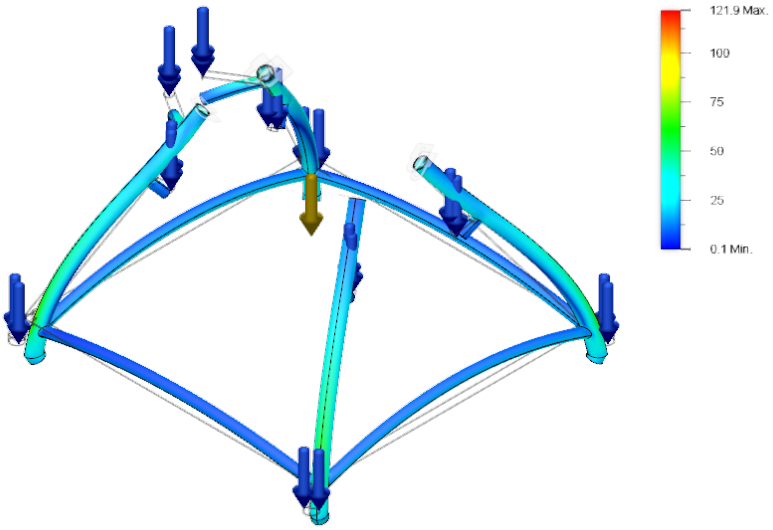

Figure 8.14: FEA of frame (legend in MPa)

8.3.3. Fuel Tank Design

As stated earlier, the fuel tank is a monocoque structure connected to the bottom of the space frame. It is a cylindrical structure with a curved top and bottom, to keep them from bending easily. The cylindrical shape has been chosen so that the pressure is evenly distributed on the sides due to the fuel weight.

A cross-section view can be seen in Figure 8.15. It can be observed that the bottom is curved inwards, so that the helicopter can land on the ring that is formed. This way, there is no landing gear needed and weight is saved. The material chosen for the tank is CFRP, and a wall thickness of 3 mm is enough according to the structural analysis carried out.

The Autodesk Fusion software is used to analyse the most critical condition, which is when the rotorcraft lands with a deceleration of $1.5g$. The structure has a safety factor of 2.25 if the maximum stress of 133 MPa is taken into account during this manoeuvre. The tank is connected to the frame at four locations around the perimeter of the top surface so that is where the forces are applied to the tank. Inside the tank, there are partitions in order to avoid the large mass of fuel starting to slosh, which would put the helicopter out of balance and might even induce an oscillation in combination with the control system which tries to compensate for the fuel slosh. The partitions are designed such that fuel can move passively between the different sections, but only very slowly, to avoid the need for extra fuel pumps and lines.

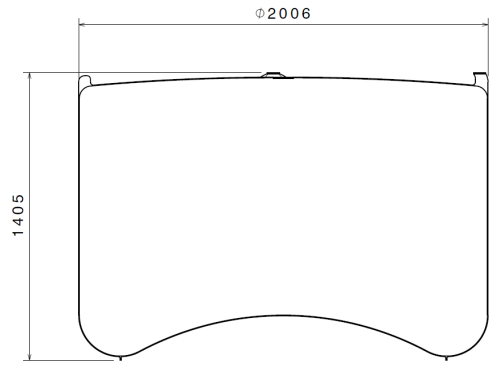

Figure 8.15: Fuel tank shape and dimensions

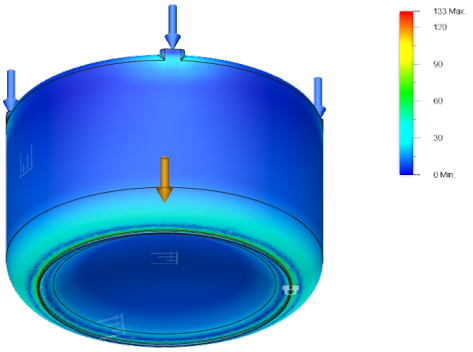

Figure 8.16: FEA of fuel tank (legend in MPa)

8.3.4. Material Selection

The material selection for the airframe was performed while keeping in mind the critical aspects as discussed before: tensile and vibrational loading as well as keeping the weight as light as possible.

In order to chose for the best option, the relevant specific characteristics of the material, which are strength, Young's modulus and density, need to be properly analysed. It should be noted that for the current loading scenario, the material selected is dependent on the specific strength and specific modulus of the material. However, due to the present vibrational loads, the structure can be represented as a large spring. The design space for the material selection is discussed in Materials Selection in Mechanical Design by Ashby[27]. The required high strength in the current loading case is the reason that foams and ceramics are not considered as sensible option. This leaves the choice to elastomers, polymers, composites and metals. Based on the required high Young's Modulus, the design space is presented by composites and metals. The specific strength $\sigma/\ \rho$ and specific modulus $E/\ \rho$ of different representing

materials was evaluated. Due to their high tensile strength capability, both the composite materials, represented by glass fiber, aramid and carbon fiber, and the metals, steel, titanium and aluminium, show good performance with respect to those criteria. However, the latter impose an increase in weight, which is highly unwanted, thus it was decided that composites, more specifically CFRP, are the best option for the structural material. This was verified by Figure 8.17, where the design space for light weight springs is illustrated.

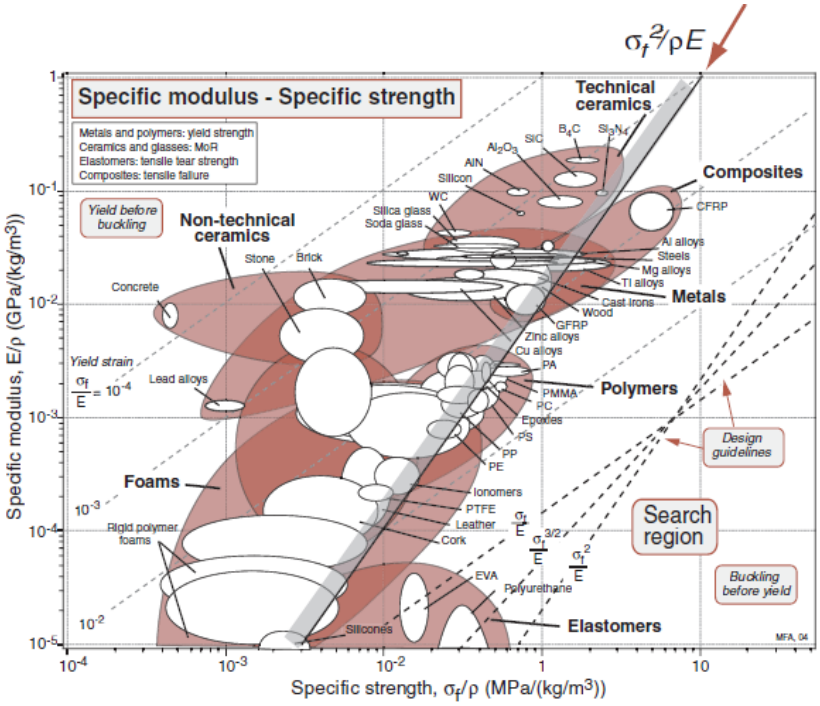

Figure 8.17: Material selection[27]

8.4. Shaft and Hub Design

In this section the shaft and the hub design of the rotorcraft are going to be discussed. Firstly, the methods for representing and simulating the loading of the hub in an accurate way were studied. Two loading scenarios are going to be analysed.

Firstly, the loading case when the rotorcraft is on the ground, the engine is producing torque, the blades are starting to rotate, but lift force is absent and the hub and shaft need to be able to support the weight of the blades, will be discussed. This is represented in Figure 8.18. Next to this, focus will be put on the loading when the engine is creating torque and the blades are rotating and producing lift required for taking off, illustrated in Figure 8.19. The latter representation is supported by the analysis discussion by Wane Johnson[28].

It should be noted that the current design implements a hinge, which accounts for the flapping and lagging of the blades, as well as a damper that reduces the vibrational loads on the structure. Additionally, the control system, as discussed later in Chapter 9, will contribute to limiting the vibrations.

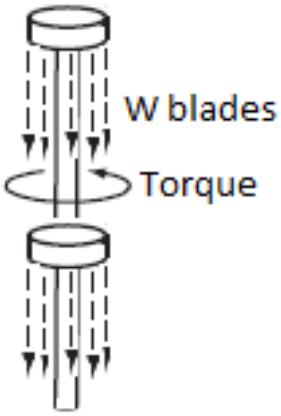

Figure 8.18: Hub and shaft loading Case I

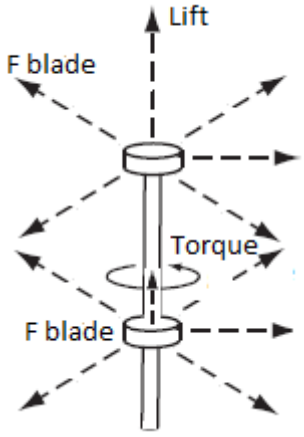

Figure 8.19: Hub and shaft loading Case II

Shaft Design

The shaft is the part that connects the engine to the hub and respectively to the rotor blades. It should be noted that due to the coaxial rotor configuration, two shafts need to be designed. The main loading is imposed by the torque that needs to be transferred to the rotor in order to provide rotation and allow for the blades to produce lift. Moreover, the shaft needs to be able to carry the tensile loads due to the lift force, the weight of the blades and the hub and to be able to support the centrifugal forces created when the blades are rotating.

Firstly, the average tensile stress is expressed by Equation 8.11, thus the resistance to the loading created by the lift is dependent on the material properties and the cross section of the shaft.

Next to this, the stress imposed by the created torque on a solid shaft is expressed by Equation 8.21, where τ is the shear stress, T is the torque created by the engine, R is the radius of the shaft and J is the polar moment of inertia, that is calculated by Equation 8.22[19]. For hollow thin skinned shaft the torque that can be met is given by Equation 8.23, which depends on the enclosed area A and the shear flow in the cross section, that is dependent on the shear stress and thickness as given in Equation 8.24[12].

$$\tau = \frac{T \cdot R}{J} \tag{8.21}$$

$$J = \frac{\pi R^4}{2} \tag{8.22}$$

$$T = 2Aq \tag{8.23}$$

$$q = \tau t \tag{8.24}$$

Naturally, due to the fact that the shaft connecting the engine to the bottom rotor needs to be able to accommodate inside its cross section the shaft that connects the top rotor, it needs to be designed as a hollow tube with a specific radius. On the other hand, the longer shaft will have to be able to carry additional bending loadings and will need to be able to support the weight of the hub and blades, thus a solid tube is expected to perform better than a hollow one. However, just for a comparison, a hollow option was analysed, but it resulted in having too high of a radius that would impose that the radius of the lower shaft will also need to be increased, and consequently the weight of the system.

Hub Design

The blades of the rotor are attached to the hub by a means of a hinge, which is attached to the shaft. It should be noted that it is assumed that the loading due to the drag of the blades as well as the flapping motion of the blades are fully carried by the hinge. Thus, the design of the hub should account for the weight of the blades, the centrifugal force created by them when rotating at maximum rotational speed and the torque of the shaft. Furthermore, the geometry needs to be able to accommodate the specific number of blades, which in this case is 5, and at the same time to not create excessive drag.

Firstly, a circular cross section was considered. This proved to be capable of carrying the loads and the blades could be placed accordingly. However, due to the directional loading in the system, a possible optimisation was seen, which lead to the conclusion that a star shape hub could be a possible solution. This was later evaluated with Fusion 360 and proved to be the reasonable solution.

8.4.1. Analysis and Results

Taking into account the above mentioned analysis, the hub and shaft system could be designed. It should be noted that for the calculations, as stated by the requirements, a safety factor of 1.5 the loads is used.

Material Selection For the material selection of the hub and shaft three possibilities were considered: CFRP, aluminium and steel.

Having a lower density compared to steel, CFRP and aluminium would be more beneficial for the weight optimisation of the system. However, due to the high loading on the hub and shaft from the blades weight and the torque from the engine, at the connection points between the shaft and the hub as well as between the separate sections of the hub a very high stress is experienced. This stress was found to be higher than the ultimate strength of either CFRP or aluminium, thus a failure would occur. Consequently, it has been decided that steel alloy would be the best option for the hub and shaft system, which will provide the required strength. The chosen specific material is Steel AISI 1045 595 QT, which has a yield strength of 1860 MPa and an ultimate strength of 2239 MPa, as provided by Fusion 360.

Dimensions Considering the loading, as presented in Figure 8.19, the shaft connecting the engine to the top hub resulted in having an optimal radius of 25 mm and the hollow shaft a radius of 30 mm. However, when analysing the loading scenario presented by Figure 8.18, it was realised that the stiffness of the shaft is not sufficient in order to support the weight of the blades and the hub. Thus, a further analysis concluded that the final design implements a solid shaft with a radius of 40 mm and a hollow one with an outer radius of 45 mm and thickness of 4 mm. For the hub design, fitting the blades and the hinges, transferring the load due to the torque from the shaft to the hub and carrying the weight of the blades is determining the thickness and the overall design.

Stress and displacement results Using the FEA model previously discussed, the maximum total displacement that was critical was observed in Case II loading and was found to be 9.7 mm, as presented in Figure 8.20. It was realised that the the torque is the one contributing the most to the hub displacement, as the longitudinal displacement was found to be only 1.15 mm, only 1/10 of the total one. Furthermore, due to the asymmetric cross section of the hub, the centre of gravity of the system has a an offset in the x-direction of 180 mm. When rotating with high speeds, this can cause additional structural loads and instability of the shaft. Even though the analysis performed was carried out by assuming the highest loads that are going to be experienced by the structure and no failure is expected, it is recommended that, if further design and analysis of the system is carried away, a balancing weight is implemented in the two hub designs.

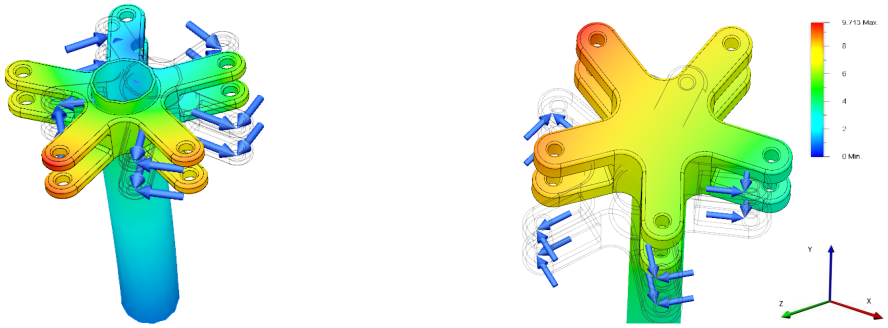

(a) Case II total displacement in bottom hub (b) Case II total displacement in top hub

Figure 8.20: Total displacement Case II

Next to this, the stress experienced by the structure was studied and the one experienced by the top hub is presented in Figure 8.21. It can be noted that the maximum stress present on the scale is said to be 2570 MPa. However, even if this is higher than the ultimate strength value of the material, it is spotted in only one point on the structure and is considered to be an outlier, due to the meshing properties. Thus, it is not considered as a failure point. The highest stress met by the structure due to the loading is 1390 MPa and can be observed where the shaft is connected to the hub. As the maximum strength of the material is higher than this stress, no failure is going to be occur.

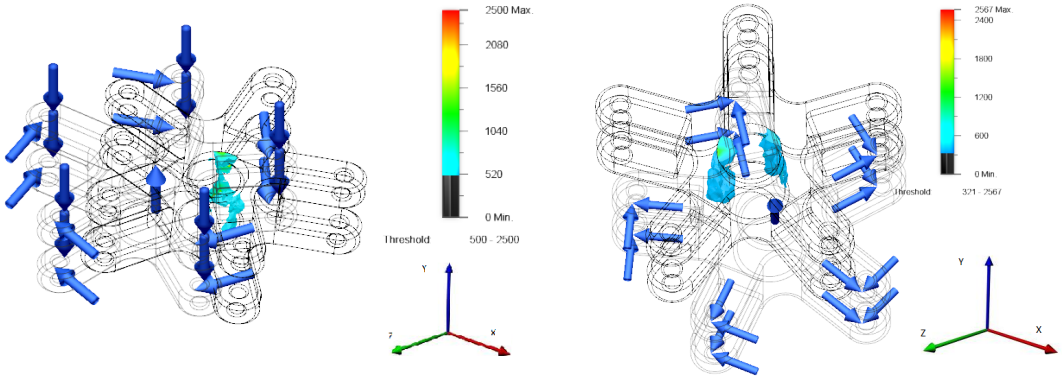

(a) Stress on the top hub Case I (b) Stress on the top hub Case II

Figure 8.21: Von Mises stress top hub

8.5. Structures Manufacturing Plan

The current section will give an overview of the production plan of the structure. Firstly, the production of the blades will be described, followed by the airframe and tank and finally, the hub and shaft system.

Production of Blades

Manufacturing methods of the blades strongly influences its life as they can introduce conditions that affect the fatigue life, such as variations in the resin content, the fiber orientation and imposed local residual stress. Two main categories in blade production are present: manual and mechanical. The small to medium blades are typically produced manually by using wet lay-up processes. For large blades, mechanical processes are more common, such as filament and tape winding. For helicopter blades

semimechanised processes are utilised[29].

The external skins are firstly pre-cured and then then separately layered. The front area of the raw spar is machined in order to obtained the correct shape and additional weights for balancing are added to the leading edge. Then the different frames are assembled and glued together. Lastly, the flap actuator components are assembled[30]. The trailing edge of the blade is typically honeycomb sandwich and has very thin skin[29].

Production of Airframe and Fuel Tank

As discussed, the airframe is represented by a truss structure and the material used is a CFRP. For this, tubes with 20 mm and 4 mm are required. Next to this, the fuel tank that has a cylindrical shape is also produced from CFRP. Two methods are considered for producing such tubes and cylinder: filament winding and pultrusion.

Filament winding is the process of winding fibres and the matrix of the material around a predetermined shape[31]. It is typically used for producing composite structures with a cylindrical and hollow shape. However, the disadvantage of this process is that it is hard orientating the fibres in the longitudinal direction. Thus, this method is considered appropriate for producing the fuel tank, but not the tubes for the airframe[21] It sould be noted that the fuel tank can not be produced as a single piece. Rather, the top, side and bottom should be separately manufactured and then assembled together.

Pultrusion is the process of pulled through a die with a predetermined shape. Typically, this method results in a highly unidirectional fibres orientation. This would not be beneficial for the fuel tank structure. On the other, the truss structure is mainly loaded in tension and having a unidirectional material with the highest strength working in the loaded direction is going to be highly beneficial[22].

Last but not least, the connection between the different components needs to be discussed. There are three main methods to be analysed: mechanical bonding, welding or joining the components by the use of adhesives[31]. The first one implements using rivets and bolts. This, however, is not considered the optimal solution due to the fact that high stress is usually present at the hole locations and, with the expected high vibrational loadings, this can lead to structural failure. Thus, the choice is left between welding or using adhesives. Welding of composites is highly challenging process that is possible only when the matrix of the material is a thermoplastic. However, due to the expected high temperatures imposed from the engine and the APU, a thermoset is going to be optimal for the matrix. Thus, bonding with adhesive is recommended. There are variable aerospace adhesive that can resist very high tensile stresses[23].

Production of Hub and Shaft

Last but not least, the steel-made hub and shaft system is going to be discussed. There are various production techniques for producing metal components such as: bending, stretching, extruding and others[31].

Regarding the shaft production, due to the simple shape of the cross section, extruding the material through a die with a corresponding shape is considered as the most optimal solution. However, as the hubs have more complex cross sections that also need to be precisely manufactured, the best option is considered to be casting them. Due to the small tolerance required, investment casting is going to be the optimal solution which also achieves predictable static and fatigue resistance levels[31].

[21] URL www.composite.about.com/od/equipment/a/Filament-Winding-The-Basics.html [cited 22 January 17]
[22] URL www.composite.about.com/od/eqptpultrusion/a/The-Pultrusion-Process.html [cited 22 January 2017]
[23] URL http://solutions.3m.com/wps/portal/3M/en_US/Adhesives/Tapes/Products/Two-Part-Epoxy?N=6081606&rt=c3 [cited 21 January 2017]

9 Control System

The current chapter discusses the control system of the rotorcraft. Firstly, Section 9.1 will present the possible control systems, which will be followed by Section 9.2 where a trade-off between them will be provide. Section 9.3 shows the stability analysis in hover conditions, which is going to be supported by the discussion on active control in Section 9.4. The control system layout will be presented in Section 9.5. Last but not least, Section 9.6 lists the relative conclusions and recommendations.

9.1. Control Systems Options

This section describes the different control system lay-outs considered for the rotorcraft design. Each design is shortly explained and some advantages are named.

Swashplates

The conventional way of controlling rotorcraft is by using swashplates. They consist of a non-rotating bottom disk which can be lifted and tilted by control levers, and a spinning upper disk that moves as a reaction to the bottom disk. The upper disk is attached to the blades and provides a change in blade pitch. Swashplates are able to provide both cyclic and collective pitch for full rotorcraft control[32].

Currently there is ongoing research in swashplate technology with the development and testing of an electrical swashplate. It shows that electrical swashplates are a feasible solution for the replacement of conventional ones. Some main advantages include elimination of hydraulic systems, therefore lowering weight, complexity, costs and maintenance requirements[33].

Pivoting Propellers

Another control system design concept was to use external pivoting propellers to provide the needed control force. Two small propellers would be placed on the sides of the rotorcraft, attached to the fuselage. The distance from the fuselage is such that a relatively small force generates enough momentum to control the rotorcraft. The propellers are able to pivot in order to ensure full control. Pivoting propellers are currently used in aircraft, though not for rotorcraft control.

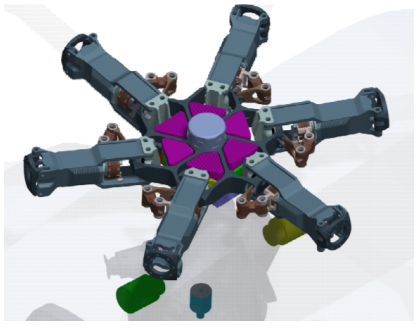

Figure 9.1: Individual blade control system design[34]

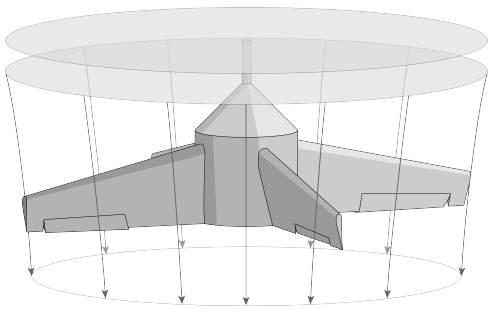

Figure 9.2: Wake fins control system design

Individual Blade Control

The individual blade control (IBC) is currently used as an addition to conventional control methods to improve noise and vibration effects. Research has been commissioned in order to explore if a rotorcraft

can be solely controlled by an integrated IBC system since IBC has several advantages as compared to conventional systems. The system introduces a reduction in vibration, noise, weight and power required and restrains resonance effects[34, 35].

An example of the design of the aforementioned IBC system is shown in Figure 9.1. The control system is completely integrated into the rotor head. All blades have a separate actuation system, providing extra degrees of freedom as compared to conventional designs without complementary actuators[34].

Servoflaps

Servoflaps are amongst control systems with a relatively high technological maturity level, but are used not that much for general rotorcraft control. A servoflap controlled main rotor is defined by the addition of small flaps on the trailing edge of the rotor blades. A mechanism controls the flap, generating a small force. The induced momentum pitches the blade, providing cyclic and collective pitch abilities. Servoflaps eliminate the need for hydraulics and require lower control forces due to the unique lay-out[36, 37].

Wake Fins

An additional control system design includes wake fins. The design consist of multiple fins, or wing shaped structural components, attached to the rotorcraft fuselage. Each fin has a trailing edge flap controlling the generated forces on the surface. The forces are produced by the airflow of the rotor wake along the surface of the fins. A basic example of this configuration can be found in Figure 9.2.

Continuous Trailing Edge Flaps

Continuous trailing edge flaps (CTEFs) make use of active bimorph actuators located at the trailing edge section of the airfoil, as illustrated in Figure 9.3. These bimorph actuators deform the trailing edge, introducing a change in lift and pitching moment coefficients. A main advantage is that CTEFs eliminate mechanical components and hinges in the rotating system, hence reducing drag. Its main goal is to reduce noise and vibration, while increasing performance and ensuring full control capabilities.

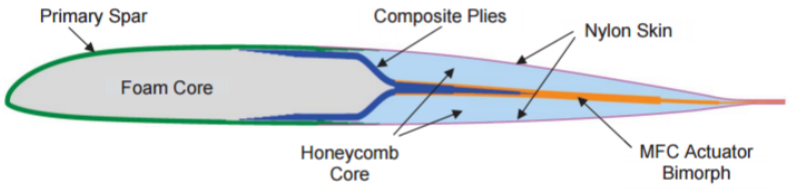

Figure 9.3: A continuous trailing edge flap design[24]

9.2. Trade-Off

In this section the trade-off of the different control system designs is presented. First in Subsection 9.2.1 the used trade-off criteria and their weights are discussed. Subsection 9.2.2 presents trade-off and the reasoning behind the scores. In Subsection 9.2.3 a sensitivity analysis is done on the trade of and Subsection 9.2.4 presents the final control system choice.

9.2.1. Trade-Off Criteria and Weight Factors

For the trade-off it was chosen to use the same method as for choosing the concept design. Criteria were determined from the original requirement tree[1] and logical further additions. Establishing their relative weights was done by separately weighing each criterion against all others in a pairwise comparison.

Table 9.1 presents the trade-off with its criteria and their respective weight values. Firstly, it can be observed that the most influential criterion is the ***accuracy*** with a weight of 30%. This criterion comes

from the requirement for full rotorcraft control capabilities. For an effective system a high ***responsiveness*** is also a necessity. Highly responsive systems allow for effective counteractions of gusts and therefore a stable hover environment. Consequently the criterion is given a weight of 25%. The subsystem ***weight*** has a relative weight of 19%. As hovering performance is considered a driving design feature, one way to significantly increase hover performance is to lower the rotorcraft weight, thus lowering subsystem weight. One of the AHS competition requirements states that the design should be able to be built within the next five years. Therefore the ***technology readiness level*** (TRL) has a weight of 11%. Finally, with a weight of 5% the ***power consumption***, ***reliability*** and ***manufacturability*** are considered relatively less important to the design choice, but cannot be forgotten. When the power consumption of the subsystem is low, more power is available for hover, thus aiding the main goal. Reliability is also important for the design, as a failure of a subsystem during the competition will result in a complete failure of the design. As for manufacturability, having a design that is extremely hard to build but still is successful might not be optimal as this might hamper achieving the goal of demonstrating an improvement in current technology.

9.2.2. Trade-Off Scores

In this subsection, for each trade-off criterion, it is shortly clarified why the different control systems received their score as presented in Table 9.1.

Accuracy - The individual blade control, servoflaps and continuous trailing edge flaps score good on accuracy, because they are able to generate multiple inputs during one revolution[24, 34, 37]. Both electric and hydraulic swashplates are in this sense limited to one input setting throughout a single rotation, thus loosing accuracy. The wake fins make use of the rotor wake and do not alter blade lift directly, which also negatively affects accuracy. The pivoting propellers are expected to be unable to combine cyclic and collective control.

Responsiveness - The responsiveness of both swashplates, IBC, servoflaps and CTEFs are deemed to be good. While swashplates and servoflaps are flight proven, IBC and CTEFs have been designed for high responsiveness[24, 34, 37]. The wake fins are thought to have a lower responsiveness, since the control force is generated by the rotor wake. The pivoting propellers scored bad, since the propellers need time to pivot before being able to generate a force in the right direction.

Weight - Servoflaps and CTEFs do not need heavy structural or hydraulic components[24, 37]. The wake fins consist of a low-load bearing structure and electric swashplates weigh less than the hydraulic version, but the structural system is still relatively heavy[33]. The propellers need a heavy structure to place them at a sufficiently large distance from the fuselage. Hydraulic swashplates have been proven to be heavy and the IBC system so far has the same order of magnitude as the hydraulic system[34].

TRL - The technology readiness level scores were divided such that currently existing systems, hydraulic swashplates and servoflaps, scored good. Electric swashplates, IBC and CTEFs are presently being developed and tested[24, 33, 34], and are given a moderate score. Pivoting propellers have been used before, however not as a control system for a rotorcraft and wake fins are a relatively new concept. Both receive a low score.

Power Consumption - Since the servoflaps, wake fins and CTEFs have a low actuation power, its power consumption is small[23, 38]. The individual blade control system scored moderate as they are more power efficient as compared to conventional systems[34], however since the systems controls the whole blade, more power is needed as compared to flaps. The same reasoning goes for the electric swashplates[33]. The hydraulic swashplates and pivoting propellers are deemed to have a relatively high power consumption.

Reliability - The reliability of hydraulic swashplates is flight proven. Testing of its electric counterpart gives a low catastrophic failure rate, thus high reliability[33]. Wake fins are thought to have a high reliability due to its low number of moving parts. The propellers, IBC, CTEFs and servoflaps are thought to have a moderate reliability because they have a higher number of moving parts.

Table 9.1: Control system trade-off

	Weights	**Hydraulic Swashplates**	**Electric Swashplates**	**Pivoting Propellers**	**Individual Blade Control**	**Servoflaps**	**Wake Fins**	**Continuous Trailing Edge Flaps**
Accuracy	0.30	Moderate	Moderate	Bad	Good	Good	Moderate	Good
Responsiveness	0.25	Good	Good	Bad	Good	Good	Moderate	Good
Weight	0.19	Bad	Moderate	Bad	Bad	Good	Moderate	Good
TRL	0.11	Good	Moderate	Bad	Moderate	Good	Bad	Moderate
Power Consumption	0.05	Bad	Moderate	Bad	Moderate	Good	Good	Good
Reliability	0.05	Good	Good	Moderate	Moderate	Moderate	Good	Moderate
Manufacturability	0.05	Good	Good	Moderate	Moderate	Moderate	Good	Moderate
Weighted average		2.26	2.36	1.11	2.36	2.90	2.03	2.79

Manufacturability - The swashplates score good on manufacturability due to the available technical knowledge of the system. The wake fins are also thought to be a relatively simple design. Pivoting propellers exist and are manufacturable, however they have never been used in this setting. Servoflaps are not that common in aviation, furthermore they need a more complex system that allows energy transfer to the rotating hub. The IBC and CTEF research shows that the designs are manufacturable, however due to the high number of moving parts, the complexity is higher[24, 34].

It can be seen from the trade-off table that the servoflaps have the highest score, however the continuous trailing edge flaps are a close second, the only difference being in the TRL. The other systems have a significantly lower score and can be discarded. The difference between the servoflaps and CTEFs is so small, and only the cause of one criterion. The sensitivity analysis in Subsection 9.2.3 and top level comparison will provide the final design choice in Subsection 9.2.4.

9.2.3. Sensitivity Analysis

In order to evaluate the outcome of the trade-off, a sensitivity analysis has been done. Several changes were made to the table in order to show their effect on the trade-off. The adjustments can be divided into changes in the score scale and removing criteria.

Changing Trade-Off Score Scale

The original trade-off used the scores $1-3$ or bad, moderate and good. In order to test the method's sensitivity, the score scale was refined to $1-5$, or bad, semi-bad, moderate, good and excellent. When changing the score scale, the two best designs change position. This is mainly due to the refinement in the scores for the main criteria. The CTEFs are deemed to have a higher accuracy and responsiveness as compared to the servoflaps due to its innovative design. The scores of the other systems strongly resemble the original ones.

Removing One Trade-Off Criterion

Another way of testing the trade method is by removing one criterion since the results should not be heavily dependent on a single criterion. Considering that a feasible situation is dismissing the requirement of building within 5 years, TRL is a criterion of interest. As can be seen in Table 9.1 the difference between the two best solutions is dependent on the TRL. If that particular criterion is removed, the servoflaps and CTEFs end up with the same score. When the highest weighing criterion is removed and the weights of the remaining are redefined, the scores resemble those of the original trade-off. IBC did get a relatively lower score but the servoflaps and CTEFs are still numbers one and two respectively.

9.2.4. Final Choice

From the original trade-off two control system design came forward as potential solutions. The servoflaps and CTEFs both scored significantly higher than the other systems, with a minor difference between the two. The sensitivity analysis showed that the two systems are indeed interchangeable. In a top level comparison, the continuous trailing edge flaps are thought to have an advantage over the servoflaps for several reasons. First of all, CTEFs score better on accuracy and responsiveness when refining the score. Furthermore, they are innovative and have the potential to be further developed and improved. Another reason is that CTEFs are designed such that they can actively reduce vibrations and noise, resulting in a more efficient output and acoustic signature reduction. Moreover, one of the options to increase endurance is controlling the RPM throughout the flight. CTEFs can aid in this process by actively changing the blade twist and lift coefficient throughout flight.

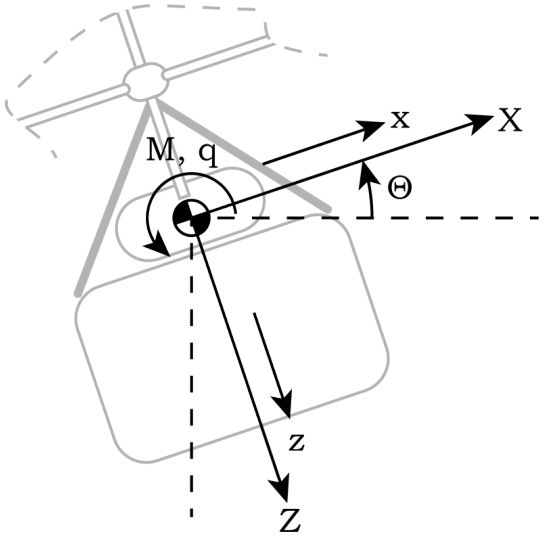

Figure 9.4: Axis system and sign conventions

9.3. Stability Analysis in Hover

This section contains an analysis of the DREAM's dynamic stability characteristics while hovering in the absence of controls. The purpose is to determine the characteristics of the helicopter's eigenmodes such as frequency and amplitude doubling time. The analysis is focused on hover, since it is the DREAM's principal function. Assumptions are listed, along with their motivations and limitations. The general equations of motion in one horizontal plane are given in Section 9.3.2. All input variables and applied formulae are listed in Section 9.3.3. Then the helicopter's unforced eigenmodes are briefly explained in Section 9.3.4.

Partial derivatives of the form $\frac{\delta A}{\delta B}$ are given the shorthand notation A_B. Time derivatives $\frac{du}{dt}$ are denoted $\dot{u}$. A body-centered axis system is used (see Figure 9.4). The majority of equations and methods, as well as verification data, are derived from literature[17](See especially Ch.9).

9.3.1. Assumptions

To simplify analysis, a number of assumptions are made. The following list outlines the most important assumptions.

(1) *The rotorcraft is assumed to be radially symmetrical.* As a consequence, analysis of longitudinal motion and pitch is considered equivalent to lateral motion and roll.

(2) *Longitudinal and lateral motion are treated as independent.* The stability analysis will be carried out in a two-dimensional plane with three degrees of freedom. This greatly simplifies analysis, but ignore certain types of motion, like tracing a circular path on the ground.

(3) *Yawing motion is not analysed.* It is assumed that yaw can be controlled sufficiently with collective control inputs to vary torque between the two rotor disks.

(4) *Certain stability derivatives are assumed to be zero in hover*, namely $X_{\dot{z}} = Z_{\dot{x}} = Z_{\dot{q}} = M_{\dot{z}} = M_{\dot{z}} = 0$. Vertical motion should not affect the horizontal force on the rotor and vice versa, hence $X_{\dot{z}}$ and $Z_{\dot{x}}$ are

zero. $Z_{\dot{q}}$ is zero because the variable thrust profile caused by a pitching motion is cancelled on both sides. $M_{\dot{z}}$ and $M_{\dot{z}}$ are zero because the rotor axis passes through the center of gravity.

(5) *The interaction between rotors does not affect stability derivatives.* Under this assumption, the main stability derivatives can be modelled as the sum of the values computed separately for each rotor.

(6) *Angles are assumed to be small.* As such, the small angle identities $\sin(\theta) \approx \theta$ and $\cos(\theta) \approx 1$ hold.

9.3.2. Equations of Motion in Hover

Under assumptions **(2)** and **(3)**, the helicopter's motion is governed by Equations 9.1 - 9.3. X, Z and M are the total moments and forces acting on the rotorcraft. x, z and Θ are the three degrees of freedom. q is the pitch rate. Furthermore, m and I_{yy} are the helicopter's mass and moment of inertia. X_C, Z_C and M_C are control inputs[17].

$$-m\ddot{x} + X_{\dot{x}}\dot{x} + X_{\dot{z}}\dot{z} + X_q q - mg\Theta = -X_C \tag{9.1}$$
$$Z_{\dot{x}}\dot{x} - m\ddot{z} + Z_{\dot{z}}\dot{z} + Z_q q = -Z_C \tag{9.2}$$
$$M_{\dot{x}}\dot{x} + M_{\dot{z}}\ddot{z} + M_{\dot{z}}\dot{z} + M_q q - I_{yy}\dot{q} = -M_C \tag{9.3}$$

This linear system of partial differential equations can be simplified by applying assumption **(4)**. Substituting $\dot{x}$ with $\dot{x}(s)e^{st}$, doing the same for $\dot{z}$ and Θ and setting the control input C to zero, the system becomes:

$$\begin{bmatrix} X_{\dot{x}} - ms & 0 & X_q s - mg \\ 0 & Z_{\dot{z}} - ms & 0 \\ M_{\dot{x}} & 0 & M_q s - I_{yy}s^2 \end{bmatrix} \begin{bmatrix} \dot{x}(s) \\ \dot{z}(s) \\ \Theta(s) \end{bmatrix} = \overrightarrow{0} \tag{9.4}$$

Setting the determinant of the matrix in 9.4 equal to zero results in a characteristic equation of the form $As^4 + Bs^3 + Cs^2 + Ds + E = 0$, with coefficients given by Equations 9.5. The solutions to the characteristic equation give insight into the eigenmodes of the rotorcraft.

$$\begin{aligned} A &= m^2 I_{yy} \\ B &= -m(I_{yy}(X_{\dot{x}} + Z_{\dot{z}}) + mM_q) \\ C &= m(Z_{\dot{z}}M_q + X_{\dot{x}}M_q - X_q M_{\dot{x}}) + I_{yy}X_{\dot{x}}Z_{\dot{z}} \\ D &= m^2 g M_{\dot{x}} + Z_{\dot{z}}(X_{\dot{x}}M_q - X_q M_{\dot{x}}) \\ E &= -mgZ_{\dot{z}}M_{\dot{x}} \end{aligned} \tag{9.5}$$

9.3.3. Calculation of Stability Derivatives

The five main stability derivatives involved in this analysis are $X_{\dot{x}}$, X_q, $Z_{\dot{z}}$, $M_{\dot{x}}$ and M_q. Their values are calculated using formulae from literature. A list of input values related to the DREAM's aerodynamic and structural properties is used to compute the stability derivatives. The calculation method takes the effects of horizontal rotor force H and blade flapping a_{1_s} into account. The tip speed ratio and inflow ratio, μ and λ', reflect how horizontal and vertical motion induce forces on the rotor[17].

Tables 9.2 and 9.3 list all initial inputs. These inputs are the result of aerodynamic and structural analysis of the DREAM. Tables 9.4 and 9.5 list the intermediate variables and derivatives. The results

are summarised in Table 9.6. The analysis is repeated at three different weights: takeoff, around half empty and landing. The decrease in weight over the mission has various effects, such as shifting the c.g., decreasing thrust and rotation speed, and decreasing the moment of inertia. Values are given for the separate rotors where applicable. Because of assumption **(5)**, the total values of the final stability derivatives $X_{\dot{x}}$, X_q, $Z_{\dot{z}}$, $M_{\dot{x}}$ and M_q are obtained by adding the two rotor values together, e.g. $X_{\dot{x}_{top}} + X_{\dot{x}_{bottom}} = X_{\dot{x}_{total}}$.

	Description	Value
g	Gravity	9.81 m/s^2
ρ	Air density	1.225 kg/m^3
R	Rotor radius	8 m
n_b	Number of blades	5
C_{L_α}	Lift gradient	7.38 rad^{-1}
e/R	Hinge offset ratio	0.0188
A	Disk area	201 m^2

	Description	Top	Bottom
A_b	Blade area	8.15 m^2	7.00 m^2
θ_0	Root pitch	0.573 rad	0.793 rad
$\theta_{.75}$	Pitch at $r/R = .75$	0.234 rad	0.250 rad
θ_1	Twist	-0.367 rad	-0.663 rad
γ	Lock No.	6.76	12.0
σ	Solidity Ratio	0.0405	0.0348

Table 9.2: Inputs which remain constant throughout the mission

	Description	Rotor	Start	Middle	End
T	Thrust	Top	29,000 N	17,600 N	10,000 N
		Bottom	20,000 N	12,200 N	6,940 N
h_m	Rotor to c.g. distance	Top	3.62 m	3.44 m	2.37 m
		Bottom	1.62 m	1.44 m	0.369 m
V_{tip}	Tip speed	Both	140 m/s	111 m/s	82.8 m/s
I_{yy}	Moment of inertia	Helicopter	10,100 kgm^2	9,350 kgm^2	4,720 kgm^2

Table 9.3: Inputs which vary throughout the mission

	Formula	Rotor	Start	Middle	End
m	$(T_{top} + T_{bottom})/g$	Helicopter	5000 kg	3040 kg	1730 kg
Ω	V_{tip}/R	Both	17.5 rad/s	13.8 rad/s	10.4 rad/s
C_T/σ	$T/(\rho A_b V_{tip}^2)$	Top	0.148	0.143	0.146
		Bottom	0.119	0.115	0.118
V_i	$\sqrt{T/2\rho A}$	Top	7.67 m/s	5.98 m/s	4.51 m/s
		Bottom	6.37 m/s	4.98 m/s	3.75 m/s
ϕ	V_i/V_{tip}	Top	0.0548	0.0538	0.0544
		Bottom	0.0455	0.0448	0.0453

Table 9.4: Derived variables

9.3.4. Eigenmodes in Hover

Now that the main stability derivatives have been computed, they can be substituted into Equation 9.5 to determine the eigenvalues of the helicopter in hover. Table 9.7 lists the eigenvalues computed for the three different mission stages. The values in Table 9.6 are used as inputs.

The DREAM has four distinct eigenvalues corresponding to three eigenmodes in 2D hover. There are two pure converging modes represented by negative, real eigenvalues, and one diverging oscillatory mode represented by a complex pair.

The slower convergent mode affects vertical speed, which will automatically decrease as a result of $Z_{\dot{z}}$ being negative. The faster converging mode affects horizontal and angular motion. However, the divergent mode affects these as well. Therefore, given an initial disturbance, the rotorcraft will oscillate

	Formula	Rotor	Start	Middle	End
$C_H/\sigma_{a_{1_s}}$	$\frac{3}{2}C_T/\sigma\left(1-\frac{C_{L_\alpha}\theta_{.75}}{18C_T/\sigma}\right)$	Top	0.0784	0.0707	0.0752
		Bottom	0.0247	0.0195	0.0233
$C_T/\sigma_{\lambda'}$	$\frac{1}{\frac{8}{C_{L_\alpha}}+\sqrt{\frac{\sigma}{2C_T/\sigma}}}$	Top	0.688	0.685	0.687
		Bottom	0.682	0.679	0.681
$a_{1_{s\mu}}$	$\frac{8}{3}\theta_0+2\theta_1-2\phi$	Top	0.684	0.686	0.685
		Bottom	0.698	0.699	0.698
$a_{1_{sq}}$	$-\frac{4}{\gamma\Omega(1-e/R)^2}\left(4+\frac{3e/R}{1-e/R}\right)$	Top	-0.142	-0.180	-0.241
		Bottom	-0.0803	-0.101	-0.136
$\mu_{\dot{x}}$, $\lambda_{\dot{z}}$	$\frac{2}{V_{tip}}$	Total	0.0143	0.0180	0.0242
$M_{a_{1_s}}$	$\frac{3e/R\rho A_b V_{tip}^2 R C_{L_\alpha}}{4\gamma}$	Top	24,000	15,100	8,410
		Bottom	11,628	7,310	4,070

Table 9.5: Intermediate helicopter derivatives

	Formula	Rotor	Start	Middle	End
$X_{\dot{x}}$	$-\rho A_b V_{tip}^2 C_H/\sigma_{a_{1_s}} a_{1_{s\mu}}\mu_{\dot{x}}$	Top	-149	-107	-85.2
		Bottom	-41.5	-25.9	-23.1
		Total	-191	-133	-108
X_q	$-\rho A_b V_{tip}^2 C_H/\sigma_{a_{1_s}} a_{1_{sq}}$	Top	2,190	1,560	1,240
		Bottom	334	208	186
		Total	2,520	1,770	1,430
$Z_{\dot{z}}$	$-\rho A_b V_{tip}^2 C_T/\sigma_{\lambda'}\lambda'_{\dot{z}}$	Top	$-1,920$	$-1,520$	$-1,140$
		Bottom	$-1,640$	$-1,290$	-967
		Total	$-3,560$	$-2,810$	$-2,100$
$M_{\dot{x}}$	$M_{a_{1_s}} a_{1_{s\mu}}\mu_{\dot{x}} - X_{\dot{x}} h_m$	Top	778	556	341
		Bottom	183	129	77.1
		Total	960	686	418
M_q	$M_{a_{1_s}} a_{1_{sq}} - X_{\dot{x}} h_m$	Top	$-11,300$	$-8,090$	$-4,970$
		Bottom	$-14,700$	$-1,040$	-621
		Total	$-12,800$	$-9,130$	$-5,590$

Table 9.6: Helicopter stability derivatives

Mission segment	Eigenvalue	$T_{\frac{1}{2}}$ or T_2	Period	Frequency
Start	-1.65	0.420 s	–	–
	-0.713	0.972 s	–	–
	$0.171 \pm 0.732\ i$	4.04 s	8.58 s	0.117 Hz
Middle	-1.39	0.498 s	–	–
	-0.926	0.749 s	–	–
	$0.186 \pm 0.695\ i$	3.73 s	9.04 s	0.111 Hz
End	-1.59	0.437 s	–	–
	-1.22	0.568 s	–	–
	$0.172 \pm 0.719\ i$	4.03 s	8.74 s	0.114 Hz

Table 9.7: Eigenvalues of the DREAM in hover

and topple over in the absence of inputs. Figures 9.5 and 9.6 illustrate typical time histories for z, x and Θ given an initial disturbance.

The helicopter's diverging eigenmode makes active stability control necessary. Section 9.4 discusses various aspects of active control, including active stabilisation.

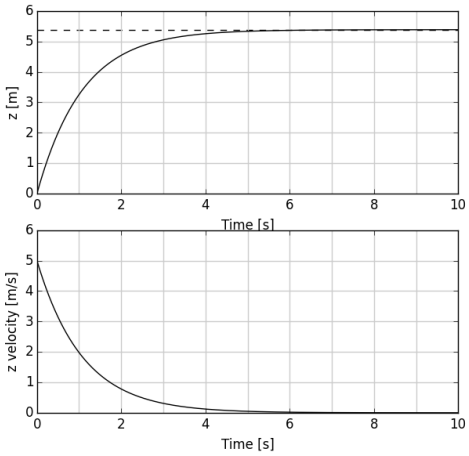

Figure 9.5: Time history of z and $\dot{z}$ from an initial speed of $\dot{z} = 5\ m/s$

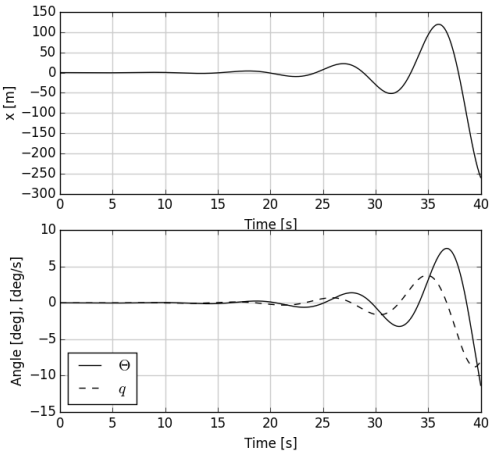

Figure 9.6: Time history of x, Θ and q from a small starting angle

9.3.5. Method Verification

The eigenvalues found in this section were computed using a custom written computer program. It is possible, and likely, to make mistakes when writing code. Method verification is a useful tool toward avoiding unnecessary errors.

The method used to calculate the stability eigenvalues is verified against an example helicopter from literature for which the inputs and eigenvalues are known. The input values of the example helicopter are provided to the eigenvalue calculation program, and the resultant eigenvalues are compared to those found in literature in Table 9.8.

From the table it is clear that the developed program properly follows the same general method as the literary source. Discrepancies are small, no larger than 4%, and may be caused by things like small input value differences and rounding errors.

Literature	Program	% Discrepancy
-0.89	-0.88	1%
-0.28	-0.29	4%
$-0.076 \pm 0.36i$	$-0.075 \pm 0.35i$	1% , 3%

Table 9.8: Eigenvalue comparison between literature and code

9.4. Active Control

It has been established in Section 9.3 that active stability control is needed to avoid rapidly amplifying divergent motion. Furthermore, the helicopter has to be able to perform simple manoeuvres like changing to a particular attitude or ascending to a certain altitude. This section explores the attainable control performance.

9.4.1. Assumptions

(7) *The analysis is based on the "Middle" flight segment described in Section 9.3.* The input and output values given in Tables 9.3 - 9.6, under the header *Middle*, are used. This segment is chosen because it has the least stable eigenmode, making it a worst-case scenario in this respect.

(8) *The maximum achievable control moment and thrust are assumed to be* $\frac{1}{10}WR$ *and* $\frac{1}{4}W$*, respectively.* This estimate is based off assumptions **(8.1)** - **(8.4)**. Combining these assumptions, the control force that can be generated is $Z_C = \frac{3}{5}\frac{5}{12}T = \frac{1}{4}W$. The maximum moment is $\frac{4}{10}R\frac{1}{4}W = \frac{1}{10}WR$.

(8.1) *The CTEFs span from* $0.7R$ *to* R *on every blade.* This is the approximate area where the lower rotor does not experience wake interference, and produces the most thrust.

(8.2) *The average* C_L *without CTEFs is* 1.2. This is based off the average tip twist of 0.168 and lift gradient of $C_{L_\alpha} = 7.38$ (see Table 9.2).

(8.3) *The CTEFs can change* C_L *by* 0.5[24]. Combining this with the previous assumption, the CTEFs can increase or decrease thrust near the tips by a factor of 5/12.

(8.4) *3/5 of the total thrust is produced in the CTEF region in a triangular distribution.* This means the maximum control moment arm is $0.8R$, and the average arm is $0.4R$ because of the rotating blade.

9.4.2. Method

To investigate the rotorcraft's response to controls, a numerical simulation is used. The helicopter's motion is modelled using the simplified equations of motion given in Equation 9.4, along with a vertical control force Z_C and control moment M_C (see Equations 9.6 to 9.8).

$$\ddot{x} = \frac{1}{m}(X_{\dot{x}}\dot{x} + X_q q - mg\Theta) \tag{9.6}$$

$$\ddot{z} = \frac{1}{m}(Z_{\dot{z}} + Z_C) \tag{9.7}$$

$$\dot{q} = \frac{1}{I_{yy}}(M_{\dot{x}}\dot{x} + M_q q + M_C) \tag{9.8}$$

The stability derivatives, mass and moment of inertia are used as inputs in the simulation. The state variables x, z and Θ and their derivatives are computed and incremented at discrete time steps. The time step Δt used is 1 ms.

9.4.3. Response to Disturbances

Active stablisation control is needed for the DREAM to fulfill its mission. Pitch and horizontal motion are inherently unstable. There are a number of ways to solve this problem. A simple control loop is enough to take care of the unstable motion. Simply adding a control moment input $M_C = M_\Theta\Theta$ allows for active stabilisation. M_Θ has to be less than $-6,890\ Nm/rad$ properly damp the helicopter's motion.

Figures 9.7 to 9.10 represent different damping intensities. Each graph is the response to a given initial pitch rate. It is possible to increase M_Θ even further to achieve stronger damping. The control moments exerted are not large enough to equal the maximum moment introduced in assumption **(8)**. In conclusion, the rotorcraft is capable of stabilising when subjected to pitch disturbances.

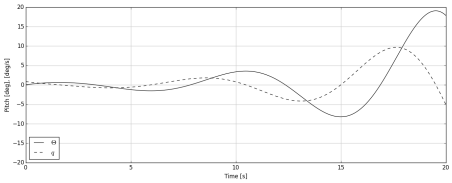

Figure 9.7: $M_\Theta = 0$, $q_0 = 0.015$. No damping, motion is unstable

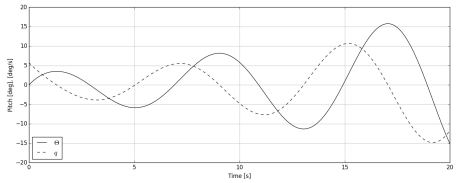

Figure 9.8: $M_\Theta = -4,000$, $q_0 = 0.1$. Insufficient damping, motion is unstable

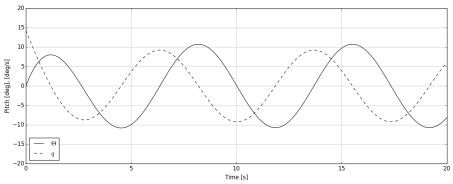

Figure 9.9: $M_\Theta = -6,890$, $q_0 = 0.25$. Neutral damping, motion is neutrally stable

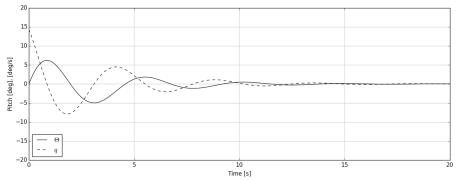

Figure 9.10: $M_\Theta = -20,000$, $q_0 = 0.25$. Sufficient damping, motion is stable

9.4.4. Attitude Quickness

The requirements related to attitude performance have remained partly undefined until this point in the design process. It has been decided that the helicopter's attitude performance should be judged based on the Aeronautical Design Standard (ADS-33) attitude quickness requirements. The ADS-33 defines attitude quickness as $q_{max}/\Delta\theta_{max}$, with q_{max} and $\Delta\theta_{max}$ being the maximum pitch rate and pitch angle attained during a pitch change manoeuvre.

To perform a pitch change manoeuvre (going from one steady pitch to another) the rotorcraft has to reach equilibrium conditions. In moment equilibrium $q = 0$, hence $X_q q = M_q q = 0$. For a given target angle Θ_t, the steady state velocity is $\dot{x} = mg\Theta/X_{\dot{x}}$. For moment equilibrium, it has to hold that $MC = -M_{\dot{x}}\dot{x} = M_{\dot{x}}mg\Theta_t/X_{\dot{x}}$. Furthermore, the control moment should be nonzero and of the same sign as Θ_t when $|\Theta| < |\Theta_t|$. Through experimentation it was found that the control function $M_C(\Theta) = (\Theta - 2\Theta_t)M_{\dot{x}}/mgX_{\dot{x}}$ achieves the desired effect.

Figure 9.11 shows the response to this control function for $\Theta_t = 6°$. The maximal pitch figures are $\Delta\Theta_{max} = 19.8°$ and $q_{max} = 39.2°/s$. Hence the attitude quickness is $39.2/19.8 = 1.98/s$. Furthermore, $\Delta\Theta_{min} = 5.69°$. The ADS-33 classifies an attitude quickness of $0.7/s$ or greater as "Level 1 handling quality", which is the best of the three levels. This suggests that the DREAM's attitude changing capabilities are more than acceptable [39].

9.4.5. Altitude Changes

Because the Z-axis is decoupled from M and X, changing altitude is relatively simple. While unforced, motion along Z is governed only by $Z_{\dot{z}}$, which acts like a damper. Given a starting position z_0 and target altitude z_t, it is possible to achieve critically damped motion between the two by introducing a control force which acts like a Hookean spring (see Figure 9.12). This hypothetical spring is given a spring constant of $Z_{\Delta z}$, where $\Delta z = z - z_t$. In other words, the control force $Z_C = Z_{\Delta z}\Delta z$.

Under this model, motion along Z can be described as $m\ddot{z} + Z_{\dot{z}}\dot{z} + Z_{\Delta z}\Delta z = 0$, which has a characteristic equation $ms^2 + Z_{\dot{z}}s + Z_{\Delta z} = 0$. The discriminant of this equation is set to zero to achieve critical damping. That is, $Z_{\dot{z}}^2 - 4mZ_{\Delta z} = 0$, or $Z_{\Delta z} = Z_{\dot{z}}^2/4m$. For the given inputs, $Z_{\Delta z} = 652N/m$. Figure 9.13 depicts a climb manoeuvre of 10 m. At the maximum control input, the rotorcraft can achieve a rate of climb of $\dot{z} = \frac{Z_{C_{max}}}{Z_{\dot{z}}} = 2.64\ m/s$. From simulation results, it takes 8.39 s to get within 10% of a given target altitude.

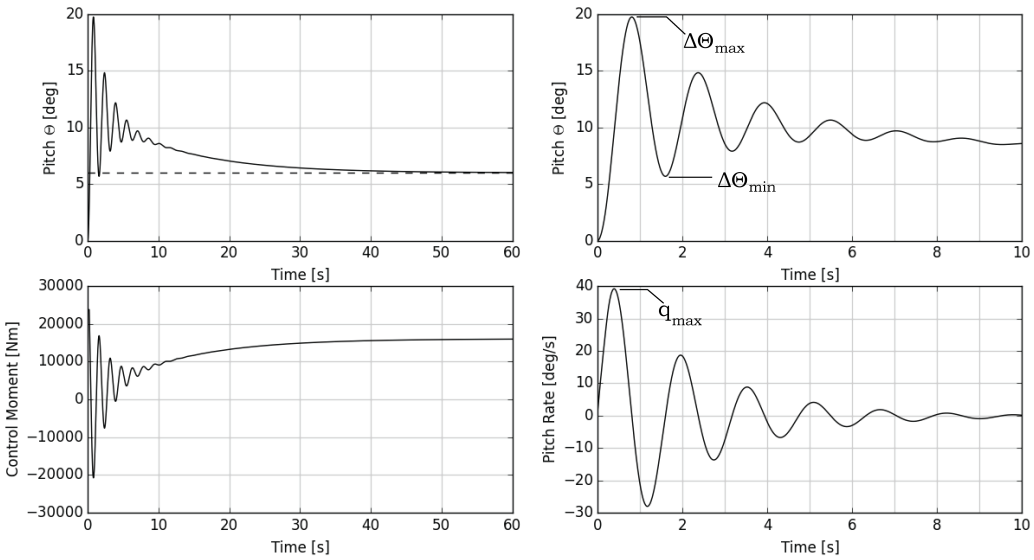

Figure 9.11: A six-degree pitch change manoeuvre

9.5. Control System Layout

This section shows the final layout of the control system

9.5.1. Continuous Trailing Edge Flaps

As stated in Subsection 9.4.1 the control surfaces will start at 70 % of the radius. This is done to make sure each flap on the lower blades would operate outside the wake contraction of the upper rotor, to ensure maximum performance. The end of the flaps will be at 97%, as shown in Figure 9.14. The flaps will be present on all ten blades to ensure full redundancy, and to ensure the DREAM can land safely in the case of multiple failures.

9.5.2. Data Handling and Electrical Diagram

The data handling diagram is shown in Figure 9.15. It shows the various information flows and sensors. These sensors and flows follow directly from the requirements statements.

The main brain of the rotorcraft is the MicroPilot[24], which consists of a triple redundant autopilot, a gyroscope, an accelerometer, an altitude sensor, a GPS and a wind speed sensor. Since the wind measurement was considered to require redundancy, a separate computer determines the difference in actual attitude and expected attitude from the flight settings. Having done this the influence the wind, and therefore the wind speed and direction can be determined.

The control surfaces require an input signal from the autopilot, which is transferred from the non-rotating to rotating parts by means of slip rings. One ring is present for each shaft, to ensure enough redundancy is present to still land in case of failure.

Besides that, the autopilot receives information on the fuel level from the sensor. From this the weight of

[24] URL https://www.micropilot.com/pdf/brochures/brochure-MP2x28.pdf [cited 24 January 2017]

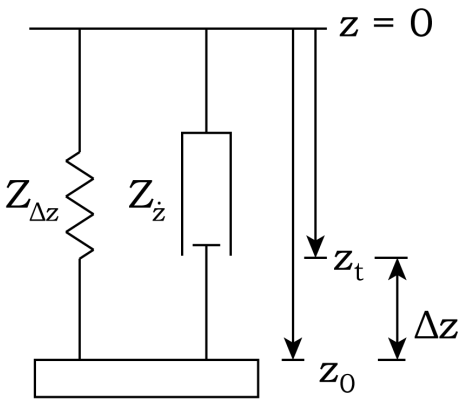

Figure 9.12: Vertical movement modelled as a spring-mass-damper system

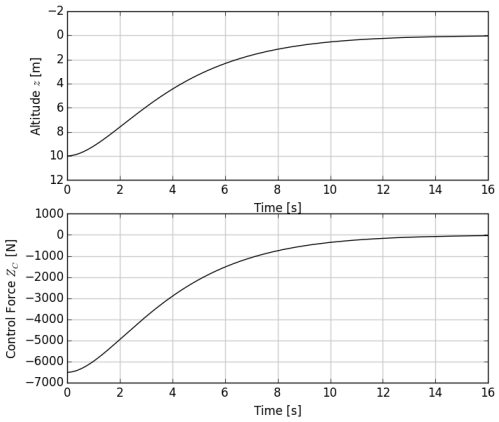

Figure 9.13: Movement between $z_0 = 10\ m$ and $z_t = 0\ m$ under the model described above

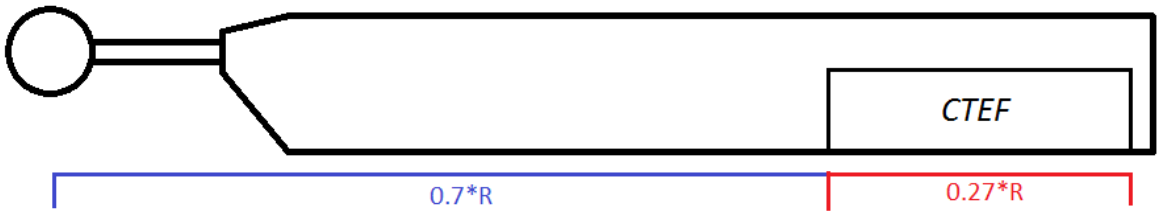

Figure 9.14: Location continuous trailing edge flaps

the rotorcraft can be determined to make sure the rotor RPM varies optimally. This is done by sending a signal to the PCVT and the fuel flow valve.

Lastly, antennas are present to communicate with GPS satellites, the CRP, the ground observers and a ground controller.

Figure 9.16 shows the electrical diagram, where the electrical connections, the power source and conversions for different systems can be seen. The power is generated by means of an auxiliary power unit. The DC output voltage is then either converted to a lower voltage to supply the engine, gearbox, communication systems and the computers with power. For the CTEFs the power is converted to a high voltage in order to operate the control surfaces.

9.6. Conclusions

The DREAM's control system is capable of changing the rotorcraft's vertical position and altitude. The rotor blades are equipped with continuous trailing edge flaps, which serve both as control surfaces and tools for blade noise reduction. The CTEFs can apply collective (force) and cyclic (moment) control inputs. They span from around 70% of the rotor radius to 97%. All devices are controlled by a triply redundant autopilot unit. This unit is equipped with various sensors and control software. Information about the helicopter is constantly communicated to the AHS's certified reference point, as well as a ground station. Because the helicopter is unstable in the absence of control inputs, the CTEFs provide active stabilisation. The control system is capable of stabilising the aircraft, as well as climbing/descending short distances, and applying attitude changes.

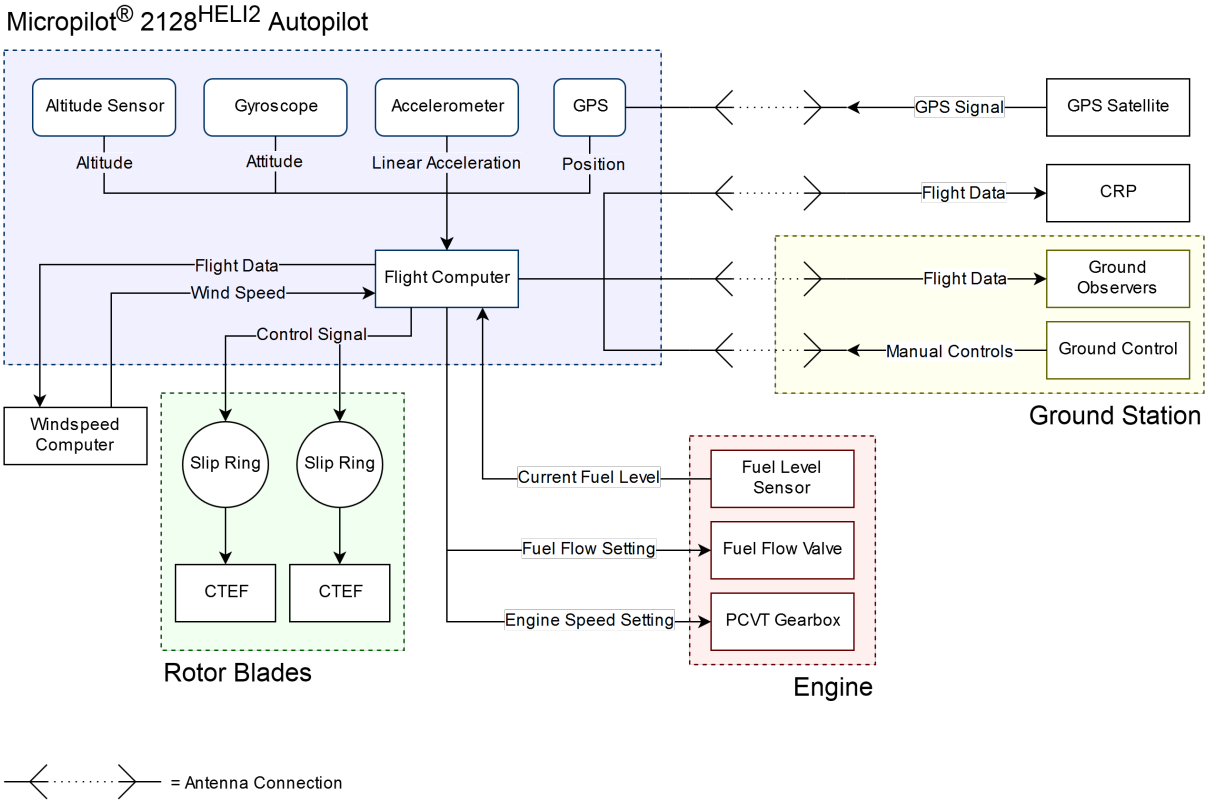

Figure 9.15: Data handling system and data flows

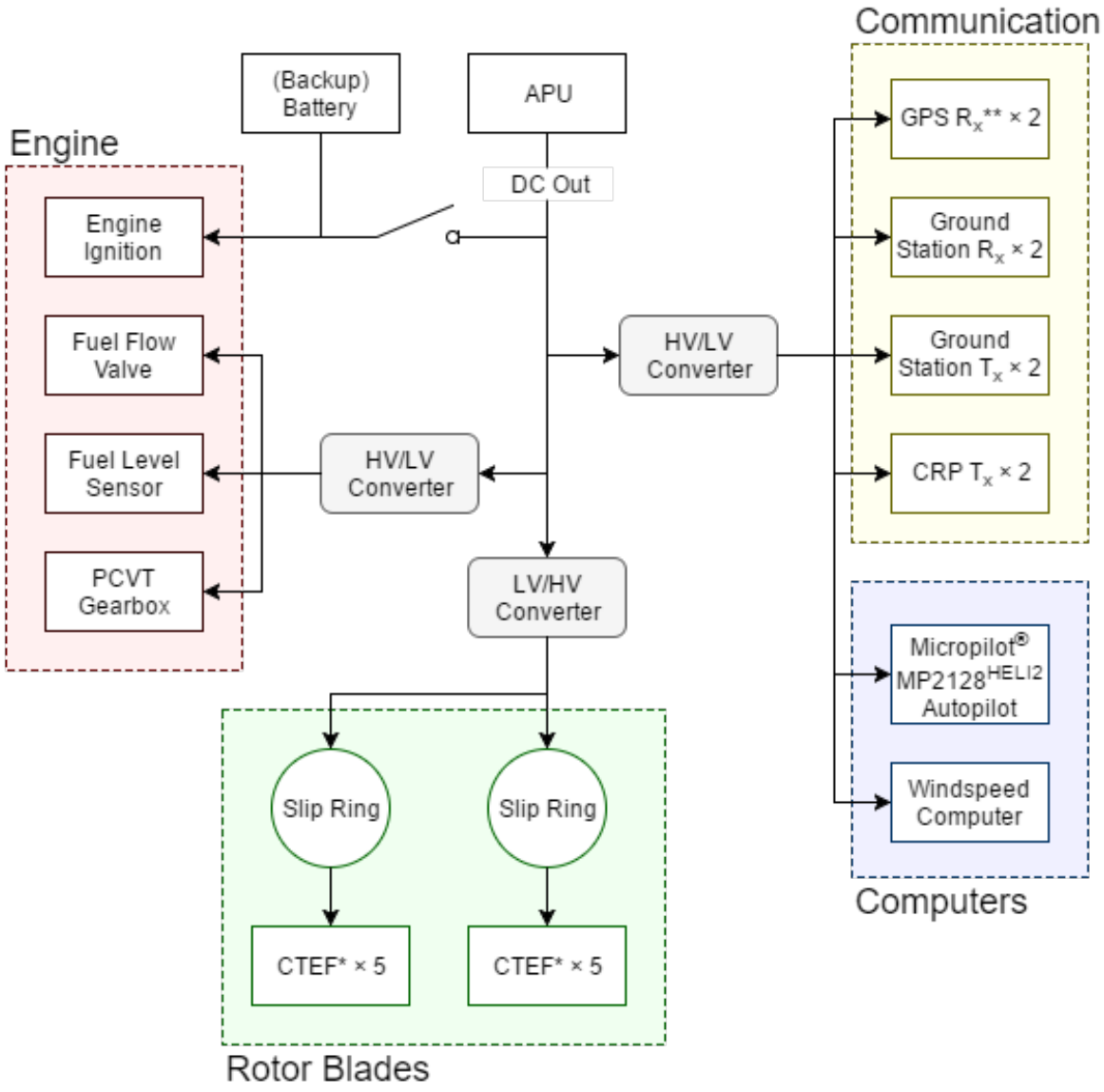

* Continous Trailing Edge Flaps

** R_x/T_x = Recieving/Transmitting Antenna

Figure 9.16: Electrical equipment and interactions

Final Design

10 Design Overview

This chapter serves as an overview of the rotorcraft and its subsystems. In Section 10.1, a short overview of the main characteristics of the subsystems are presented. Section 10.2 reviews the resouce allocation of the system: the power budget, energy budget and mass budget are discussed. The external and internal layout of the helicopter and its components are presented in Section 10.3. Lastly, a technical risk assessment is performed in Section 10.4.

10.1. Subsystem Overview

In Table 10.1, a short overview of subsystem characteristics of the helicopter is given.

Rotorcraft Characteristics		
Subsystem		Characteristics
Propulsion and Power		
	Engine	Rolls-Royce GEM 42-1 Mk.401
		Jet-A fuel
		Max. rated power: 746 kW
		Wave rotor integration
		Drive train & 1 Bevel gear, 2 Miter gears
		Gear ratio range: 3.6:1 - 23.9:1
	PCTV	Gear ratio range: 2:1 - 13:1
Rotor		
	General	2 rotor disks
		5 blades per disk
Blade		
	General	Boeing Vertol VR-12 airfoil
		8 m Radius
	Upper	Chord: 0.5 m - 0.1 m
		Twist: 45deg - 12deg
	Lower	Chord: 0.2 m
		Twist: 32.5deg - 12deg
Structure		
	Airframe	Composite lightweight frame
	Fuel tank	Composite monocoque structure
Control system		
	CTEF	70-97 % chord location
		Full controllability
		Vibration & noise reduction
	Autopilot	Triple redundancy
Payload		
	General	Non-productive and single unit of 80 kg mass

Table 10.1: Overview of rotorcraft characteristics

10.2. Resource Allocation

The rotorcraft concept that has been designed include a few technical resources that need to be monitored during future design phases. It is important to keep these resources in check, as violating the budgets for these resources can affect the performance of the rotorcraft.

Power Budget

The Power available is defined by the engine that is used. The Rolls Royce Gem manages to deliver up to 746 kW of power. However, the engine can only be operated at this power level for a maximum of ten minutes[9]. The maximum continuous power is estimated to be 690 kW. When including the transmission efficiencies, this continuous power is estimated to be 605 kW. With a contingency of 5 %, the power required should not exceed this value. The powertrain and the drivetrain system associated with this budget, is one of the heaviest components of the rotorcraft. It is essential to stay within the bounds of this budget so that the weight does not snowball out of control.

Energy Budget

The energy budget is crucial for the success of the mission. In order to ensure that the hover endurance criterion is satisfied, it is essential to know the budget for the energy required in the mission. The amount of fuel stored at the start of the mission is 3250 kg. Knowing that the specific energy of the fuel used is 42.8 MJ/Kg, the energy can be calculated[9]. This relates to an energy budget of 139.1 GJ of energy for the entire mission with a contingency of 5 % to account for fuel trapped and other losses.

Mass Budget

The rotorcraft is designed for a maximum takeoff mass of 5000 kg. The empty weight turned out to be 1752.4 kg, which is rounded off to 1750 kg in the rest of the report. How all the subsystem masses add up to this value is shown in Table 10.2.

Subsystem	**Mass** $[kg]$
Frame	30
Fuel tank	71.6
Upper rotor axis	62.1
Upper rotor blades	236.5
Upper rotor hub	54.7
Lower rotor axis	8.3
Lower rotor blades	118.5
Lower rotor hub	22.17
Engine	220.8
APU	65
Bevel gearbox	43.4
Main gearbox	584.4
Driveshafts	4.9
Electronics and equipment	75
Payload	80
Margin	75
Fuel	3247.6
Empty mass	1752.4
Take off mass	5000

Table 10.2: Overview of subsystem masses

The blade masses shown are per rotor, so the upper blades weigh 47.3 kg and the lower blades 23.7 kg each. Some of the masses presented in the table deviate from the ones mentioned in the specific subsystem explanation sections of the report. In order to make reasonable performance estimations, some masses were added or increased. Many of these mass estimation are somewhat arbitrary, the mass of for example

a gear housing is hard to estimate at this point. A reasoning is provided below.

The frame weight is rounded up from the original value of 21.3 kg. The reason for this is that the CAD model of the frame is quite simple at this stage, and in more detailed design features will be added like attachments, brackets and strengthening gussets. An extra 15 kg is estimated on top of the gears and PCVT to account for the housings/gearboxes. The electronics and equipment mass is grouped together into the 75 kg as shown in the table. This is done since very detailed values of for example (high-voltage) cables and a battery would not be reliable at this point in the project. Lastly, a margin of 75 kg is assumed to account for unforeseen mass increases and details that have not been taken into account yet.

10.3. Layout

This section covers the external and internal layout of the helicopter. A thin fairing is added to the fuselage assembly, since it was decided that this makes the design more aesthetically appealing without adding much weight. First the external layout is discussed, after which the internal layout or packaging is presented.

10.3.1. External layout

Figure 10.1 presents a schematic side view of the helicopter with the main outer dimensions. The dimensions are given in meters for clarity.

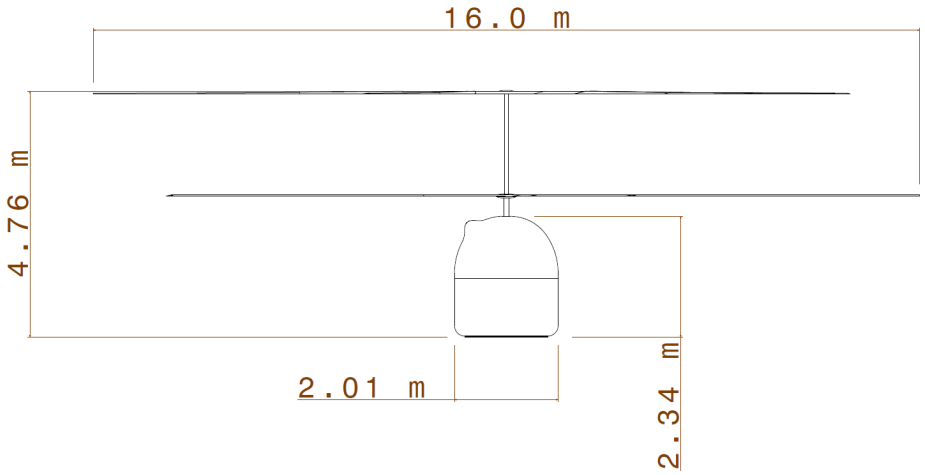

Figure 10.1: Schematic side view of the rotorcraft

Figures 10.2, 10.3 and 10.4 show renders of the rotorcraft from different perspectives. Figure 10.4 is a closeup of the upper hub assembly showing the hinge connections between the hub and blades. Note that the blades have a degree of freedom in the lead/lag and flapping direction, but are fixed around their feathering axis. The hub assembly of the lower rotor is very similar, an image is therefore left out.

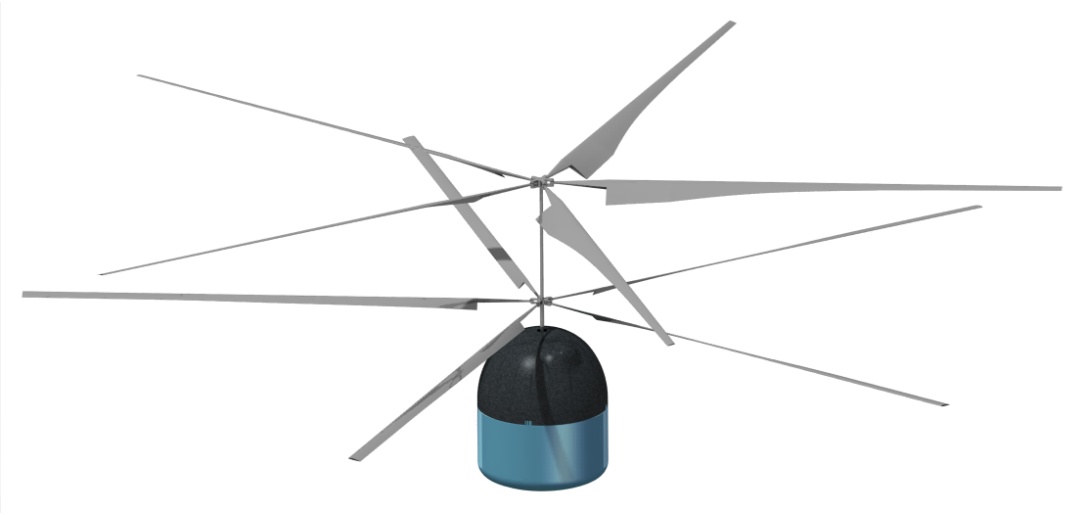

Figure 10.2: Overview of the helicopter

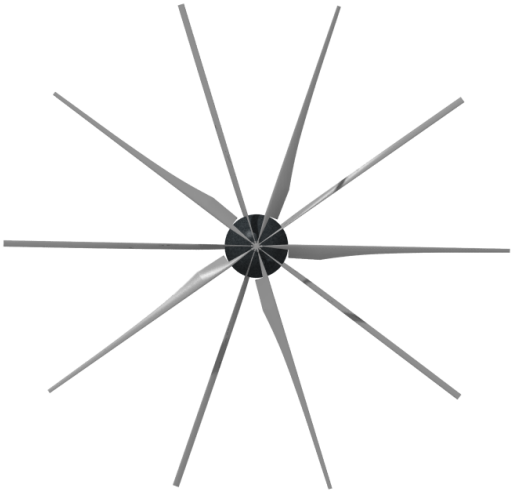

Figure 10.3: Top view

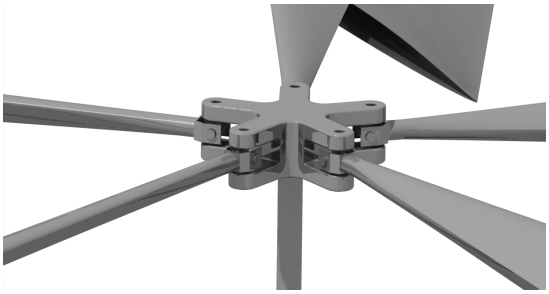

Figure 10.4: Upper hub assembly

10.3.2. Internal Layout

This section covers the basic packaging of the subsystems in the fuselage. Figure 10.5 shows the internal layout of the main components housed in the airframe. The rotors, hub and shaft assemblies are omitted here since their locations were shown in the previous section. The rotor shafts pass through the fairing and are attached to the top gearbox.

The subsystems represented in the image are simplified to basic shapes representing the maximum outer dimensions of the parts. The locations of the components are based on the resultant centre of gravity of the system. In order to have a balanced system, the centre of gravity needs to be in line with the rotor axes. Heavy components like the engine, gearbox, fuel tank and fuel are positioned so that their centre of gravities are as close as possible to this axis line. The other, somewhat smaller systems like the payload, APU and electronics unit are positioned in a way that they are in balance with each other. Certain components like cables and fuel pumps are omitted due to their relatively small size and the irrelevance of deciding on an exact position at this stage of the design. Since there is enough empty

space, these can be easily placed in a later design phase. Moreover, detailed attachments and brackets should be designed in later phases of the project and therefore are not represented in this image. The bulge on the side of the fairing is there in order to house the bevel gearbox without having a large unused space in the fuselage.

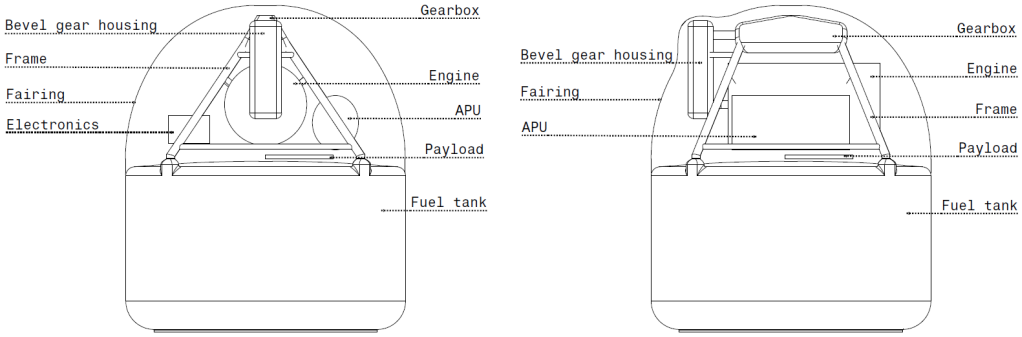

Figure 10.5: Sketches of the internal layout of the rotorcraft

10.4. Technical Risk Assessment

Designing a rotorcraft that should be capable of performing high endurance missions in hover implements various technical risks. The most important technical risks are discussed in this section. These risks can cause the hovering device not to meet its technical performance requirements. During the design process some risks were updated or removed because of alterations of the design. Also, new risks were identified during the lasts stages of the design phase.

Each technical risk is designated with a unique identifier. Furthermore, technical risks are plotted in a risk map, which is based on the probability of occurrence and severity of the risk. Based on the severity and probability of occurrence of the technical risk, a mitigation strategy could be developed. This strategy explains which counter measures should be taken in order to mitigate the technical risk. Then in Section 10.4.2 the risk mitigation is proposed, after which an updated risk map will be presented.

The risk severity of occurrence is divided in the following categories:

- **Negligible**: the effect of the risk is minimal and is very unlikely to have effect on the technical performance
- **Marginal**: performance of the design is only slightly affected
- **Critical**: there is a great reduction in technical performance of the design
- **Catastrophic**: the consequences are unforeseen and have disastrous effects on the design

The risk likelihood is also divided into several categories:

- **Feasible in Theory**: Major failure likelihood
- **Working Laboratory Model**: High likelihood of failure
- **Based on Existing Non-Flight Engineering**: Moderate likelihood of failure
- **Extrapolated from Existing Flight Design**: Unlikely to fail
- **Proven Flight Design**: Very unlikely to fail due to proof of working design

10.4.1. Technical Risks

Table 10.3: Technical risks

TR-1	The carbon fibre composite structure is very sensitive to impact damage. This damage may be poorly or absolutely not detectable by visual inspection, but detrimental to performance.
TR-2	The integrated vibrations of the structure due to the engine, the APU and the hub may lead to vibrational failures in the structure. This is hard to analyse due to the coupled vibrations from many sources.
TR-3	The actuators for the Continuous Trailing Edge Flaps (CTEF) control surfaces operate at a high frequency, while they are originally not designed for such a high frequency.Thereby reducing the reliability of the system.
TR-4	High wind speeds reduce the effectiveness of the CTEF control surfaces, and also reduce the controllability and flight speed of the rotorcraft.
TR-5	The slip rings, transmitting the CTEF signals from the non-rotating fuselage to the rotating hub, can break. This yields an uncontrollable rotorcraft.
TR-6	Wind gusts may occur which are not accounted for in the aerodynamic model or structural design. These loads may lead the system to fail.
TR-7	A shaft of the transmission system breaks. The connection to the rotors is then broken, and the rotorcraft will descend uncontrollably.
TR-8	A gear of the transmission system breaks or starts slipping. The connection to the rotors is then broken or insufficient, and the rotorcraft will descend uncontrollably.
TR-9	The Pericyclic Continuous Variable Transmission (PCVT) gearbox system has a low technology readiness level (TRL). This gives a risk that the gearbox is not ready to use within the set time range of three to five years.
TR-10	The hover time according to the competition rules only counts in wind conditions below 5 m/s. This reduces the hover time and thus reduces the chance of reaching the goal of 24 hours.
TR-11	If the power supply to the rotor is cut for any reason, the rotorcraft must go into autorotation. Due to the varying RPM the rotorcraft may will have a low RPM for some time. This will make autorotation difficult for the rotorcraft.
TR-12	The large amount of fuel in the fuel tank makes up a large part of the mass. If due to a disturbance this fuel flows to one side of the fuel tank, the unbalance of the rotorcraft will increase and the rotorcraft will become unstable.
TR-13	Resonance may occur in the rotor blades due to the varying RPM. This will lead to increasing response amplitude until failure.
TR-14	Fatigue of the structure due to vibrations may yield lower yield stresses for the structure, especially for the blades.
TR-15	The engine temperature increases to very high values. This may lead to a change of structural characteristics and consequently to a failure of the surrounding structure.

Table 10.4: Technical risks continued

TR-16	At the event of a failure and rotorcraft crash, the fuel tank is likely to be the first point of impact. It is a risk that in such an event, the fuel tank will rupture and fuel will leak into the environment, leading to a fire or explosion.
TR-17	In the event of failure and rotorcraft crash, the rotor blades may be subject to large impacts, leading them to detach from the rotorcraft. These large components are then flying projectiles imposing large threats on the surroundings and spectators.

In Table 10.5 the technical risks as described above are plotted in the risk map. The risks located in the top right corner are the ones with a high likelihood and probability and a proper mitigation should be proposed, which is performed in the next section.

Table 10.5: Risk Map

Incr. Probability →					
	Feasible in Theory			TR-2	TR-13
	Working Laboratory Model	TR-4	TR-3	TR-1, TR-9, TR-14	TR-12, TR-16, TR-17
	Based on Existing Non-Flight Engineering			TR-5, TR-10	TR-6, TR-15
	Extrapolated from Existing Flight Design			TR-11	
	Proven Flight Design				TR-7, TR-8
		Negligible	Marginal	Critical	Catastrophic
		Increasing Consequence →			

10.4.2. Risk Mitigation

For each of the risks, a mitigation is proposed to diminish the severity or likelihood of the risk.

Table 10.6: Technical risk mitigation

TR-1	Using non-destructive testing techniques, for example ultrasonic scanning of the structure can be used to check the structure. If any doubts about the structural integrity exist, these testing techniques should be implemented. Careful manufacturing, handling and transportation is required to prevent any such doubt from occurring.
TR-2	To avoid large vibratory stresses and resonance of the structure due to the engine, APU, hub, etc. the mount of these parts needs to be heavily damped. This increases the chance of over damping the system, however this also greatly reduces the chance of resonance.
TR-3	The CTEF control surfaces have many actuators to control it. The risk is present that one of them fails, however by adding sufficient amount of actuators, the impact will be small and the rotorcraft will remain controlable.
TR-4	Under high wind speed conditions the rotorcraft will lose some of its controllability. However, since the main mission objective is to hover, the limited controllability and limited forward flight speed under these conditions are taken for granted.
TR-5	The reliability of the slip ring can be increased by increasing the engineering effort into the slip ring, however the simple solution is to add redundancy.

Table 10.7: Technical risk mitigation, continued

TR-6	Wind gusts outside the scope of the design space may occur. However, the chances are deemed low since the weather is reasonably predictable. Furthermore, sufficient safety factors are taken into account to ensure this does not happen.
TR-7	The shaft of the transmission may break. However, this is a proven concept and the chances of happening are low. Because of this the risk is accepted and no redundancy is incorporated.
TR-8	The same applies as for the risk mitigation of TR-7. A gear may break, however the engineering concept is a proven concept and the chance of occurrence is low. Therefore, this risk is also accepted without redundancy.
TR-9	The gearbox system used is the PCVT, this system has a low TRL. This increases the risk of the rotorcraft being able to be built and tested within three to five years. However, this system is of great importance to the rotorcraft design, as it allows the varying of the RPM of the rotors. The risk is therefore accepted.
TR-10	The flight time when wind velocity is over 5 m/s does not count towards the total hover time counted for the competition. However, as said before, the weather is reasonably predictable, and so this situation could be avoided. Furthermore, taking into account the assumption that the other competitors will fly simultaneously, all competitors will experience the same conditions.
TR-11	When in hover, in the so called "Dead-Mans-Zone" a rotorcraft shall hover with maximum RPM, to have maximum kinetic energy in the rotor disk, so that if failure occurs the rotorcraft can perform safe autorotation. This is however not something The Hover Team can do. In order to achieve maximum endurance the RPM will need to be reduced over the flight time and thus the risk of failure in autorotation must be accepted. This is done more easily taking into account the fact that the rotorcraft does not occupy humans.
TR-12	The disturbance induced by the fuel slashing around in the fuel tank is very negative for the rotorcraft controllability. However, this is nicely solved by compartmentalising the fuel tank. The fuel will be able to move through small feed-through holes, however, the fuel will nog longer have the great slashing effect as before.
TR-13	The rotor blades are fully analyzed using Finite Element Analysis (FEA) software. The eigenfrequencies of the rotor blades are then taken under consideration of rotational speed and this is plotted against the RPM range of the rotorcraft. These plots are the so called "Campbell diagrams", using these to check the resonance RPM values and then making sure the rotorcraft does not operate at these frequencies will greatly reduce the risk of resonance and large vibration stresses.
TR-14	The rotorcraft has an intended lifetime of its mission length, so 24 hours. At first then, fatigue does not appear to be a problem. However, some further investigation is done. Because of the use of carbon fibre composites in many of the rotorcraft components, which has a high fatigue resistance, the fatigue of the rotorcraft is deemed not a large problem.
TR-15	Maximum operating temperatures of the engine and APU can be investigated. As a precaution, heat resistant materials can be used. For carbon fibre composites, the resin used is then of great importance. If needed, heat shielding of the critical components can be added to avoid critical temperatures.
TR-16	The fuel tank insides should be lined with a waterproof lining that can withstand high forces and sharp edges. For example a waterproof Kevlar or Cordura lining could prevent the event of fuel leaking.
TR-17	The hinge attaching the rotor blades needs to be designed for safe-life operation. As an extra precaution, the rotor blade needs to be designed so it does no disintegrate. The kinetic energy of the blade should be lost as fast as possible.

After the risk mitigation, the risk map is again updated. The risks have partially moved from the top right corner tot the bottom left corner, thus decreasing their likelihood and/or their severity of occurrence.

Table 10.8: Updated Risk Map

Incr. Probability →					
	Feasible in Theory				
	Working Laboratory Model	TR-4	TR-3	TR-9	
	Based on Existing Non-Flight Engineering	TR-5, TR-15	TR-10		
	Extrapolated from Existing Flight Design		TR-12, TR-13	TR-11, TR-14	TR-6, TR-16
	Proven Flight Design		TR-2	TR-1	TR-7, TR-8, TR-17
		Negligible	Marginal	Critical	Catastrophic
		Increasing Consequence →			

11 Performance Analysis

This chapter presents the performance analysis of the rotorcraft. First an analysis of hover and forward flight performance is presented in respectively Sections 11.1 and 11.2. This is followed by the determination of the endurance in Section 11.3 and a flight manual for optimal flight in Section 11.4. The noise performance of the rotorcraft is layed out in Section 11.5. Finally in Section 11.6 verification and validation measures for the performance calculations are discussed.

11.1. Hover Performance

As the main goal of the rotorcraft is to hover for 24 hours and performance calculations show the capabilities of the rotorcraft as a whole, the hover performance is an important way to indicate if the rotorcraft is able to meet its requirements. According to FAR 29, for transport rotorcraft, a full hover performance analysis covers comparisons over weight, altitude and temperature ranges in which the flight is scheduled to take place[40]. However, for this specific mission, sea level values can be assumed, therefore eliminating analysis over altitude and temperature[4]. For this analysis, hover power and rate of climb in OGE will be taken into account. The final hover endurance will be discussed in Section 11.3.

First of all the needed power to hover is computed, in Section 7.4.4 the computational method is explained. The needed power to hover reduces throughout the mission due to the lowering weight of the rotorcraft, as can be seen in Figure 11.1. By actively adjusting RPM throughout the flight to accommodate for the lower hover power and weight a more efficient flight can be attained. This changing hover power is one of the main variables used in the endurance calculations for Section 11.3.

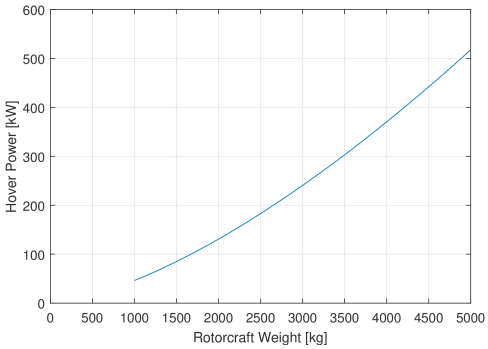

Figure 11.1: Hover power vs rotorcraft weight

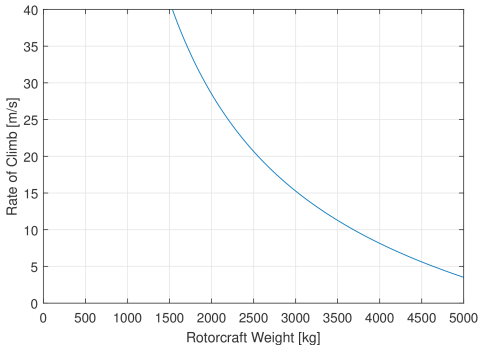

Figure 11.2: Climb rate vs rotorcraft weight

Another way of evaluating the hover performance is by determining the rotorcraft's rate of climb. The climb rate, V_c for hover conditions is defined by available excess power, which is the difference between the needed power for hover (P_h) and the engine power (P_e) divided over the aircraft weight W, as shown in Equation 11.1. The reduction of rotorcraft weight during the mission leads to a higher rate of climb, as can be seen in Figure 11.2. The FAR 29 regulations state that the rotorcraft's steady OGE rate of climb must be above 0.5 m/s at all weights, which is achieved by our rotorcraft[40].

$$V_c = \frac{P_e - P_{hov}}{W} \tag{11.1}$$

One of the rotorcraft's requirements states that the rotorcraft should be able to ascend to OGE altitude. The out of ground effect altitude is defined as 3 times the largest rotor diameter, for this specific rotorcraft that would result in an altitude of 48 m[4]. Since the density at an altitude of approximately 50 m is equal to 1.219 $\frac{kg}{m^3}$ which is almost equal to the density at sea level, the power needed to power can be assumed to equal the previously calculated hover power at sea level. From Figure 11.2 it can be seen that at this power setting, there is excess power, therefore it can be concluded that the rotorcraft is able to hover at OGE altitude.

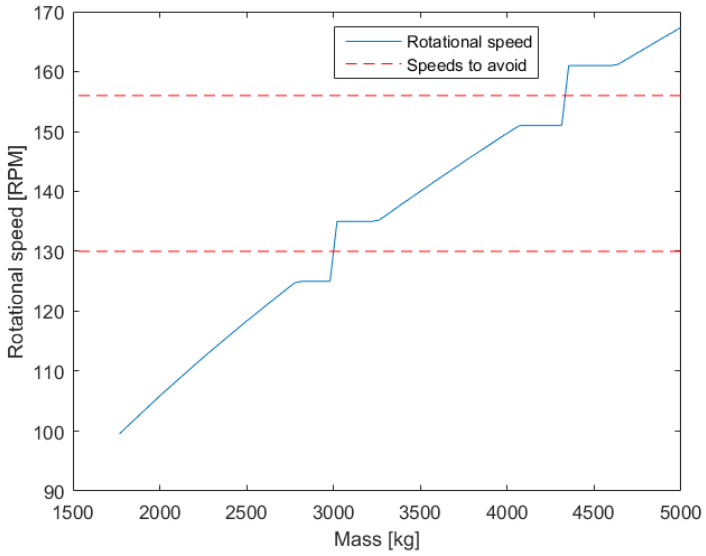

Figure 11.3: Rotor RPM vs rotorcraft weight

Due to the large change in mass during the mission, the decision to reduce the rotational speed of the rotors in order to keep the blades at an efficient L/D 7.5. Figure 11.3 shows the range of speeds over the range of the weight of the rotorcraft. Two values have to be skipped because they are eigenfrequencies of the blades. This would cause heavy, potentially destructive, vibrations. Pitch control of the blades will be used to bridge these speeds.

11.2. Forward Flight Performance

Even though the forward flight section is only a minor part of the mission, a performance analysis needs to be done. The forward flight capabilities are best shown in a breakdown of the total power needed as a function of flight speed, the power curve. The needed power for optimal forward flight is calculated in Section 7.6.7, however for a preliminary performance calculation and visualisation of the power curve simplified formulae can be used[14].

For preliminary calculations, the total power (P_{tot}) can be divided in to the sum of induced power (P_i), determined by rotor lift, profile power (P_0), which is dependent on blade section drag, and parasite power (P_p), dependent on area drag. These are all related to forward flight speed and shown in respectively Equations 11.2 to 11.5. These are then plotted against the forward flight speed to create the power curve, shown in Figure 11.4. For the values for rotorcraft weight, thrust, induced velocity and tip speed the initial values are used since the forward flight segment is performed at the beginning of the mission.

$$P_{tot} = P_i + P_o + P_p \qquad (11.2) \qquad\qquad P_i = \kappa v_i T \qquad (11.3)$$

$$P_o = \frac{1}{8} C_{D_0} \rho A_b V_T^3 \left[1 + k_o \left(\frac{V}{V_T} \right)^2 \right] \quad (11.4)$$

$$P_p = \frac{1}{2} \rho V^3 f \quad (11.5)$$

For the induced power calculation in Equation 11.3 an empirical correction factor κ is introduced in order to account for non-uniformity in v_i and typically has a value of 1.15. In Equation 11.4 for the profile power a correction factor k_o equalling 4.5 is used in order to correct the neglection of the spanwise drag component, the reversed flow region on the retreating blade and a yaw effect for azimuth angles away from 90^o and 270^o. The parasite power in Equation 11.5 f is the equivalent flat plate area defined by Equation 11.6, where A_r equals the rotor disk area and k_p is a predefined parasite drag factor based on empirical data, which equals 0.016[14].

$$f = k_p A_r \quad (11.6)$$

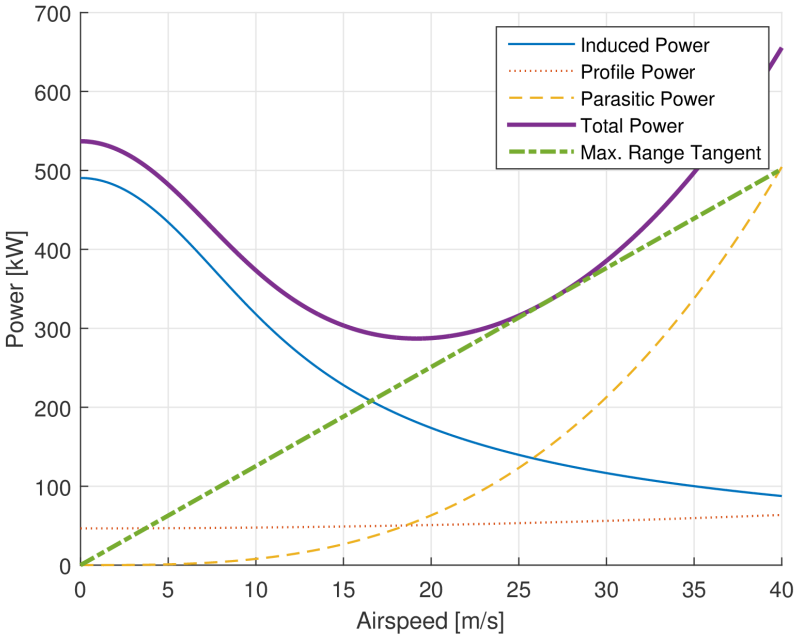

Figure 11.4: Power breakdown for forward level flight

As can be seen from the power curve, the hover power is dominated by induced power while for higher forward flight speeds parasitic power is the main contribution to the total power. This results in the typical bucket shape and shows that forward flight with moderate speed is more efficient than hover.

For the highest total endurance, the optimal flight speed must be determined so the least amount of fuel is used in the forward flight segment of the mission. For this the rotorcraft must fly at the airspeed and power for optimal range, so the largest distance is covered with the lowest fuel burn. This value can be found by drawing a tangent to the total power, shown in Figure 11.4. The optimal flight speed and corresponding power are respectively 26.7 m/s and 335 kW.

The values for hover power and maximum range power do slightly differ from those calculated in Section 7.6.7. This is due to formulae simplification and the introduction of constants to counter the effects of the assumptions made. For further endurance calculations the values calculated in Section 7.6.7 will be used.

11.3. Endurance

The total endurance of the rotorcraft is dependent on both the hover and forward flight performance. For the most optimal flight and highest endurance, it was chosen to first complete the forward flight segments of the mission, flying between the three hover stations, followed by hovering in the last station. This was chosen since forward flight is more efficient than hover, as shown in Section 11.2, so the least amount of fuel will be burned.

With Equations 11.7 and 11.8 the fuel consumption for forward flight and climb is calculated. These are simplified equations and do not give a completely accurate value. However, since the amount of fuel needed to complete these mission segments is minor as compared to the endurance part, simplified formulae are deemed to be sufficient.

$$M_f = P \cdot t \cdot SFP \qquad (11.7) \qquad\qquad t = \frac{d}{V} \qquad (11.8)$$

For the forward flight segment with an optimal flight speed of 25.1 m/s, corresponding needed power of 360 kW, a distance of 3000 m and a specific fuel consumption of 0.298 $\frac{kg}{kW\ hr}$, 3.6 kg of fuel is used. This is subtracted from the total fuel mass for the calculation of the total hover endurance.

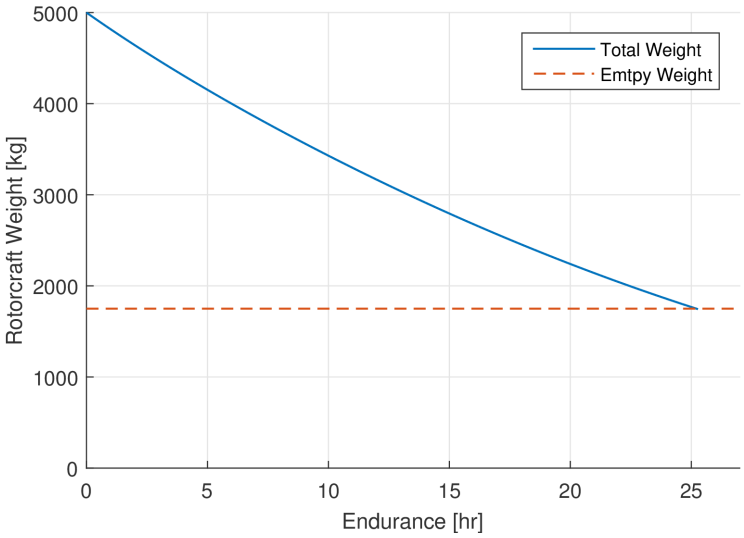

Figure 11.5: Rotorcraft endurance

The same goes for the fuel needed to climb towards an altitude of 48 m with an initial rate of climb of 3.52 m/s correlating to a maximum engine power of 690 kW and a specific fuel consumption of 0.298 $\frac{kg}{kW\ hr}$. This results in 0.78 kg of fuel is used while performing the climb. These values confirm that the climb and forward flight segments are only a minor part of the complete mission and hover defines the final endurance.

The endurance calculation for hover is an iterative process. For each time step the fuel used is calculated with the hover power for its weight at that specific moment and the current specific fuel consumption. This weight is then subtracted from the total weight and a new required power to hover is calculated. This process is repeated until the weight reaches the empty weight of the rotorcraft, shown in Figure 11.5. The iteration results in a final endurance of 25.3 hr.

11.4. Flight Manual

In order to achieve maximum endurance the rotorcraft and pilot need to know which RPM settings correspond to certain rotorcraft weight and required power to hover during the flight. A clear way of showing this relation is with the carpet plot presented in Figure 11.6. From a given power and rotorcraft weight, the needed RPM can be quickly derived from this plot.

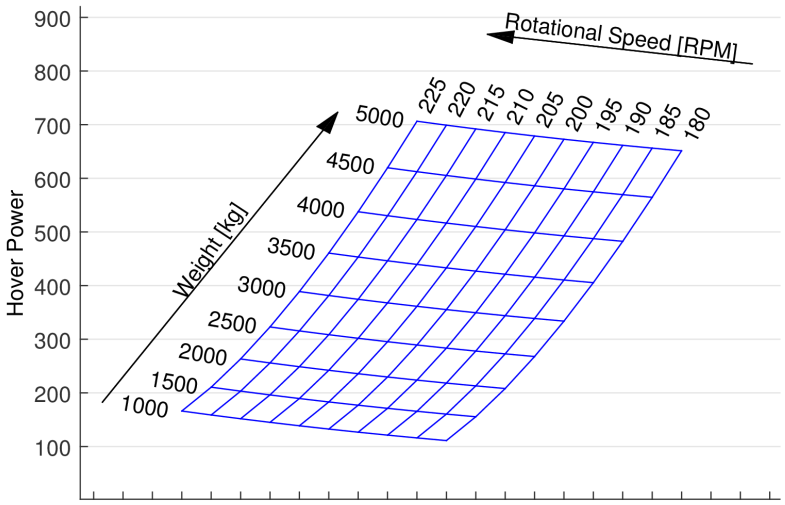

Figure 11.6: Power carpet for rotorcraft weight and RPM

11.5. Noise

When designing a helicopter its effects on the environment must be taken into account, with the acoustic signature being one of the main environmental design aspects. The produced noise can be divided into engine and main rotor noise, however, the projection of engine noise is such that further away from the rotorcraft the rotor produces the main acoustic signature.

The noise spectrum generated by typical rotorcraft is presented in Figure 11.7. Typical rotors produce blade passing, rotational, impulsive and broadband noise. The blade passing noise frequency is usually low, however, in this case the high number of blades result in a frequency of around 30 Hz. Still, it is the least important source of the total acoustic signature.

Rotational noise is the harmonic noise as a result of periodic forces exerted by the blade on the air and also includes thickness noise generated by the displacement of the air by the blade. The higher harmonics are often due to variations in load with the azimuth position of the blade, thus, they occur especially in forward flight. Therefore, the rotational noise also has a lesser importance to this mission.

Impulsive noise, also known as blade slap, is created by a blade passing through the slipstream of a preceding blade or another form of turbulent air. The two main aspects of impulsive noise include blade/vortex interaction (BVI) at lower speeds and shock waves in transonic and supersonic operation called *high-speed impulsive noise*, which will not be discussed since the rotorcraft will fly at relatively low speeds. When it occurs, BVI is the main source of vibrations and noise emission, due to its high sound pressure level (SPL) and impulsive character.

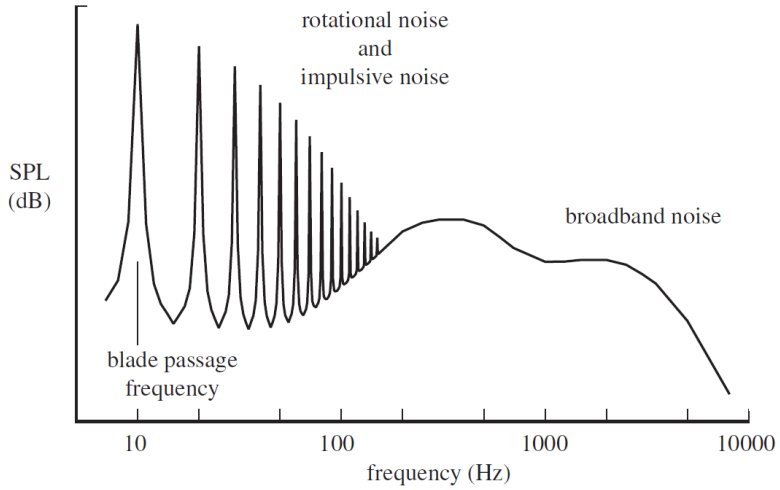

Figure 11.7: Helicopter rotor sound spectrum[28]

The last and, for this rotorcraft, important source of noise emission is broadband noise. It is generated by random changes of the forces on the blades caused by turbulence and its frequency is the most important in terms of subjective annoyance. One of the broadband noise's main origins is blade-wake interaction (BWI), which is produced by lift changes due to operation in a wake flow field and interaction of two main rotors, as in the coaxial configuration[28, 41].

It can be seen that some sources of noise are significantly reduced by the specific mission of the rotorcraft, eliminating noise generated by high velocities and complex manoeuvres. Further acoustic signature reduction is achieved by the use of CTEFs as the main control system, as discussed in Chapter 9. Testing has shown that the introduction of CTEFs can lead to a noise reduction varying from 2 dB to 7 dB for BVI[42].

11.6. Verification and Validation

As each model needs to be verified and validated to show its compliance with real data, this section will discuss the verification and validation of the calculations done for forward flight and endurance. The original hover and forward flight power equations have already been verified in Sections 7.4.4 and 7.6.7 and will be validated by NDARC in Section 15.3.

Forward Flight Performance

For verification of the forward flight equations, two methods are used. First, hand calculations with random variables check if the equations are entered correctly. Secondly, with the help of data sets and calculation examples found for different helicopters the output of the model is checked[14].

As for validation, the hover power and power for maximum range taken from the power curve are checked against those generated the rotor design model explained in Sections 7.4.4 and 7.6.7. As mentioned in Section 11.2, the values shown in the power curve differ slightly from those calculated in Sections 7.4.4 and 7.6.7. This is due to the simplification of the formulae and the introduction of constants to counter the effects of the assumptions made. The hover and forward flight power and forward flight airspeed have a deviation of respectively 2.7 % 7.5 % and 6.4 % from the original, thus are within bounds.

Endurance

The endurance equations are relatively simple and highly dependent on previously calculated values, which have been pre-verified. The calculations are verified by hand calculations. The validation is done with data generated by NDARC and is presented in Section 15.3.

Flight Manual

The power carpet plot generated for the flight manual in Section 11.4 is based on the power curve equations presented in Section 11.2. As stated before, these are verified with sample data from literature and validated with values calculated in Sections 7.4.4 and 7.6.7.

12 Sensitivity Analysis

In this chapter the sensitivity of the design is analysed with respect to some input parameters. Since the model is quite complex and includes a lot of manual subinputs and designs, which can not be automated, a complete analysis is outside the scope of this assignment. However, some parameters that are either considered important or can be automated, are investigated for the sensitivity analysis. Section 12.1 discusses the design point of the rotorcraft. This is followed by presenting the hover model in Section 12.2. Section 12.3 and Section 12.4 present and discuss the obtained results.

12.1. Design Point

The design point is the set of variables $\bar{x}$ that determine the model characteristics of the helicopter. The aim is find an optimal design point $\bar{y}$ in the design space D such that the endurance is maximised, Equation 12.1.

$$E(\bar{y}) \geq E(\bar{x}) \quad \forall \bar{x} \in D \tag{12.1}$$

In general, the design point will depend on variables that can be influenced and can not. For example the density of air is not in our direct control, a mission can be planned at days with higher air density, however, complete unbounded control is obviously impossible. On the other hand, the rotor radius, which is a design parameter, is an example of a variable that can be controlled. Sensitivity analysis of both type of variables is important to determine the stability of the endurance around the design point. The current design point, reached after several iterations, has the properties as presented in the following table.

Parameter	Value	Unit	Description
R	8	$[m]$	Rotor radius
b	5	$[-]$	Number of rotor blades
ρ	1.225	$[kg/m^3]$	Density air
W_e	17113	$[N]$	Empty weight
g	9.80665	$[m/s^2]$	Gravitational acceleration
W_d	40000	$[N]$	Design weight
Ω_d	15	$[rad/s]$	Design rotational velocity
η	0.8778	$[-]$	drivetrain efficiency

12.2. Model

The endurance can be seen as a function of n variables in vector x_i $i \in [1, 2, 3...n]$. The set of variables that are analysed are $\bar{u}$, Equation 12.2.

$$E(\bar{x}) = E(\bar{u}, \bar{v}) = E(W_d, W_e(R, b), R, b, \eta_i, \bar{v}) \tag{12.2}$$

Where $\bar{u} \subset \bar{x}$ & $\bar{v} \subset \bar{x}$ such that $\bar{u}$ contains the variables that are analysed and $\bar{v}$ the others. The relevant derivatives that have to be determined are then given by 12.3.

$$\frac{\partial E}{\partial u_i} \quad i \in [1, 2, 3..k] \; k < n \tag{12.3}$$

Due to the large complexity of the model, which is semi-analytical and non-linear, the partial derivatives are evaluated using finite difference approach of first order to keep computational effort low, Equation 12.4. Where Δu_i is chosen sufficiently small, justified by convergence for decreasing Δu_i.

$$\frac{\partial E}{\partial u_i} \approx \frac{E(\bar{x} + \Delta u_i) - E(\bar{x})}{\Delta u_i} \tag{12.4}$$

The employed analysis consists of finding the partial derivatives on the design point. Then the endurance is linearised at the design point. From this point on, two analyses are performed. Firstly, the deviation in endurance around the design point can be estimated for the lower and upper bound of the different parameters. The maximum possible deviation can be estimated by the linearised endurance Equation 12.5.

$$\Delta E|_{max} = \sum_{i=1}^{k} \left| \frac{\partial E}{\partial u_i} \Delta u_i \right| \tag{12.5}$$

The second analysis checks if the design point is in a local optimum. In general, the partial derivatives of the endurance should then be zero. Assuming local maximums do not exist this location is then a local minimum. During iteration, the design point has changed a lot, however, a pure optimum is not yet reached.

12.3. Evaluated Derivatives

Radius

The radius is an important parameter to investigate. The aerodynamic efficiency increases significantly when the radius increases. This can be easily shown using only momentum theory, since it results in an increase in disk area. However, increasing the rotor radius will yield an increase in structural empty weight, leading to the well known "snowball effect". An increase in blade weight will result in an increase in the hub weight, which needs to support higher loads. The increase in drive shaft torque will also yield an increase in drivetrain weight and perhaps even the engine weight, which varies discretely. An increase in the empty weight will yield an increase in the supporting structure weight.

Since the model has a lot of manual factors not all contributions can be considered. The increase in both blade and hub weight due to an increase in rotor size is considered. Since the empty weight is a function of the rotor radius, a partial derivative of endurance as a function of radius only without considering the empty weight, is has no physical meaning. Increasing the radius will always increase the endurance, when the effects of the empty weight increase are not considered. The endurance increase due to an increase in rotor radius should be equal and opposite to the endurance decrease due to an increase in empty weight, as can be seen from Equation 12.6.

$$\frac{dE(R, W_e(R))}{dR} = \frac{\partial E}{\partial R} + \frac{\partial E}{\partial W_e} \frac{dW_e}{dR} = 0 \tag{12.6}$$

The derivative found for the radius is provided by Equation 12.7.

$$\frac{\partial E}{\partial R} = 1.34 \ \frac{h}{m} \tag{12.7}$$

The derivative found for the empty weight is expressed by Equation 12.8.

$$\frac{\partial E}{\partial W_e} = -0.00119 \ \frac{h}{N} \tag{12.8}$$

The change in empty weight with a change in radius, as explained above, is estimated only including the major structures parts, which are the rotor blades. The derivative found was Equation 12.9.

$$\frac{dW_e}{dR} = 173.3 \ \frac{h}{N} \tag{12.9}$$

Clearly, only considering the rotor blades, condition 12.6 is not yet met.

Empty weight

The partial derivative of empty weight on its own is only relevant when a weight decrease can be obtained without compromises. That is a decrease due to more efficient engineering. A decrease in empty weight in general will be due to a decrease in rotor radius, as discussed above, or other compromises.

Amount of Blades

The amount of blades is an important design parameter, as the derivatives can only be evaluated in discrete steps of a single blade. Both an increase and a decrease in the amount of blades is considered. The decrease from the current five blades to four blades leads to derivative 12.10.

$$\frac{\partial E}{\partial b} = -0.2194 \ \frac{h}{b} \tag{12.10}$$

The increase from the current five blades to six blades leads to derivative 12.11.

$$\frac{\partial E}{\partial b} = 0.06111 \ \frac{h}{b} \tag{12.11}$$

The empty weight change due to decreasing the number of blades is not easy to model, since the structure of the blades and the hub will change and the weights of these are determined using FEA analysis, separate from the model run in MATLAB. Analysing these changes is beyond the scope of this assignment. However, quantitatively one may notice that a change in blades only changes the endurance at the current design point. Thus, assuming the rotor hub and blades total mass will not change significantly when less blades have to carry more forces or the other way around, the current design point is near optimum for this parameter.

Design weight

The design weight is the weight for which the blades are designed, as described in Section 7.4.3. The design weight of the blades is independent of the other variables, implying that it should be chosen such that the corresponding derivative is zero. The corresponding derivative is given by Equation 12.12.

$$\frac{\partial E}{\partial W_d} = -0.0000111 \ \frac{h}{N} \tag{12.12}$$

As can be seen, this derivative is close to zero, and hence optimised for the current design point.

Root cutout

The root cutout is a compromise in the design based on several important interactions. Firstly, a root all the way to location $r = 0$ is, from an aerodynamic point of view, the most efficient. However, from structural point of view, this is impossible for more than two blades. In that view the size of the hub is neglected. Since there is both a hub and the finite chord at the root, in the presence of more than two bladed, there has to be a root cutout. The aerodynamic efficiency of blade sections directly spaced next to each other is quite low, however a quantitative analysis is beyond the scope of this assignment. The root cut out decreases the airflow around the body, hence decreases the parasitic drag and power loss in hover. The change in endurance for an increasing root cutout is obviously negative, meaning that increasing the blade area, by decreasing the root cutout will yield an increase in endurance from an aerodynamic point of view, Equation 12.13.

$$\frac{\partial E}{\partial R_0} = -0.1944 \ \frac{h}{m} \tag{12.13}$$

Efficiency

The efficiency of the drivetrain is studied. However, similar analysis would yield similar results for other efficiencies. Since the efficiency of the subsystems is optimised an increase should always result in a change in other variables. For example, an increase in drivetrain efficiency due to more efficient gears will increase the weight of the gear box. However, the sensitivity to variations in the efficiency is important to take in to account. The derivative is given in Equation 12.14. For an increase in efficiency, the increase in endurance is significant. However, the magnitude of increase realistically achievable is very small.

$$\frac{\partial E}{\partial \eta} = 13.6 \ h \tag{12.14}$$

Density

The density is obviously not directly controllable, however it may alter due to weather conditions. Those should be chosen such that the density is as high as possible, as can be seen in Equation 12.15.

$$\frac{\partial E}{\partial \rho} = 4.388 \ \frac{h \cdot m^3}{kg} \tag{12.15}$$

Gravitational acceleration

Similar to the density, a change in gravitational acceleration is not achievable, unless the mission is chosen on other geographical locations. As it can be seen from the high value of the derivative of endurance with respect to the gravitational acceleration, Equation 12.16, the influence of gravity to the mission is significant. Clearly when the gravitational acceleration decreases the endurance increases.

$$\frac{\partial E}{\partial g} = -2.69 \ \frac{h \cdot s^2}{kg \cdot m} \tag{12.16}$$

Rotational design velocity

The rotational velocity is a parameter that can be optimised. Note that the helicopter uses rpm-control, and will fly over a range of rotational velocities. The design rotational velocity however, similar to the design weight, can be optimised. A change only in rotational velocity will, in general, not be possible.

When the rotational velocity increases the torque required for the same amount of power decreases, hence, the drivetrain can be designed lighter. From that point on the snowball effect can be reasoned again. This analysis is however beyond the scope of this assignment. An increase in Ω_d increases the required power from an aerodynamic point of view, thus an optimum is to be expected. In the current analysis a decrease in the design rotational velocity will always increase the endurance since modelling structural weight increase is outside the scope of this assignment. The derivative is given in Equation 12.17.

$$\frac{\partial E}{\partial \Omega_d} = -0.045 \, \frac{h \cdot s}{rad} \tag{12.17}$$

12.4. Results

Firstly, a deviation of input values, due to an error in the precision in the known value, may result in significant changes of the endurance. An estimate for the deviation in the input parameters is performed and the maximal influence on endurance, as discussed in Equation 12.5, is done here. The parameters Ω_d and W_d will not fluctuate, since they are chosen parameters for the design model. The amount of design weight will obviously not have an error in its precision known. The radius, empty weight, root cutout, efficiency, density and gravitational acceleration do however pose an uncertainty. Since the flight can be performed at a chosen geographical location,the atmospheric conditions can be chosen in such a way that they benefit to the hover performance of the rotorcraft. Hence, relevant variables that were not fixed and there uncertainty is given below.

The variables left are the radius, empty weight, root cutout, efficiency. The uncertainty in these parameters is estimated for the current design. It was found that manufacturing of composite blades with a radius of 8 m can be done with large precision. The empty weight is still an estimated parameter and can therefore still change a lot. The root cutout is a machining precision similar to the total radius. The efficiency was given by the gear manufacturer at a certain decimal number, where the uncertainty is taken at the lowest decimal.

1. $\Delta R = 1 \; cm$
2. $\Delta W_e = 50 \; kg$
3. $\Delta R_0 = 1 \; cm$
4. $\Delta \eta = 0.001$

Using Equation 12.5, the maximum error in endurance is estimated to be 0.61 $hours$. The empty weight change contributes the most to this. Thus is due to the fact that, when the empty weigh varies a lot the fuel weight changes significantly and therefore the endurance. Thus, stating that the maximum deviation in endurance is only 0.61 $hours$ seems unrealistic. However, this is based on the linearised sensitivity analysis. The uncertainty in endurance would have been higher when the $\bar{v}$ variables were analysed. This, however, was considered outside the scope of this assignment. The main discrepancies in endurance will probably be due to unforeseen efficiencies or other design considerations that are not taken into account. These considerations are discussed in the recommendations section.

13 Requirements Compliance Matrix

In the current chapter the requirements compliance matrix is going to be presented. Please note that the full list of the requirements is provided in Appendix A.

Code	Complied	Explanation
Technical Requirements		
[REQ-TL]	✓	See Section 9.4.5and Section 8.3.2
[REQ-TL-1]	✓	See Section 9.4.5
[REQ-TL-1.2]	✓	See Section 9.3
[REQ-TL-2]	✓	See Section 11.1
[AC-3]	✓	See Section 9.5.2
[AC-3.1]	✓	See Section 9.5.2
[AC-4.2]	✓	See Section 9.5.2
[AC-4.3]	✓	See Section 9.5.2
[REQ-TL-3]	✓	See Chapter 8.3.2
[REQ-HOV-1]	✓	See Chapter 11
[MS-5]	✓	See Chapter 11
[MS-5.1]	✓	See Section 9.5.2
[MS-5.1.1]	✓	See Section 9.5.2
[REQ-HOV-2]	✓	See Chapter 11
[REQ-HOV-2.1]	✓	See Chapter 9
[AC-3.2]	✓	See Chapter 11
[AC-1]	✓	See Chapter 10
[AC-1.1]	✓	See Chapter 10
[AC-1.2]	✓	See Chapter 10
[AC-1.2.1]	✓	See Chapter 10
[AC-1.2.2]	✓	See Chapter 10
[AC-1.2.3]	✓	See Chapter 10
[AC-1.3]	✓	See Chapter 10
[AC-5]	✓	See Section 9.5.2
[AC-5.1]	✓	See Section 9.5.2
[AC-5.2]	✓	See Section 9.5.2
[REQ-OP-2]	✓	See Section 8.2
[REQ-TBS]	✓	See Chapter 11
[MS-3]	✓	See Chapter 11
[REQ-TBS-2]	✓	See Section 9.5.2
[REQ-TBS-2.2.1]	✓	See Section 9.5.2
[REQ-TBS-2.2.2]	✓	See Section 9.5.2
[REQ-TBS-2.2.3]	✓	See Section 9.5.2
[REQ-TBS-2.3.1]	✓	See Section 9.5.2
[REQ-TBS-2.2.2]	✓	See Section 9.5.2
[REQ-TBS-2.2.3]	✓	See Section 9.5.2
Constraints		
[REQ-SS]	✓	See Chapters 6 and 9

[**REQ-SS.1**]	✓	See Chapters 6
[**REQ-HA**]	✓	See Chapter 10
[**AC-7**]	✓	See Chapter 10
[**AC-8**]	✓	See Chapter 10
[**AC-2**]	✓	See Section 16.3
[**AC-2.1**]	✓	See Section 16.3
[**AC-2.2**]	✓	See Section 16.3
[**AC-2.3**]	✓	
[**AC-2.4**]	✓	
[**AC-9**]	✓	

[**AC-2.3**] Each of the used technologies is either already developed or is expected to be developed within the next 5 years.

[**AC-2.4**] The production plan of the design is much shorter than this period.

[**AC-9**] All parts and systems of the rotorcraft are connected.

14 Reliability, Availability, Maintainability and Safety

The current chapter focuses on analysing the reliability, availability, maintainability and safety of the design. The reliability of the design is discussed in Section 14.1. It should be noted that availability and maintainability have been discussed in Sections 14.2 and 14.3, but they are not considered relevant for the present concept. Lastly, more elaborate discussion on the safety of the design is present in Section 14.4.

14.1. Reliability

Reliability is the ability of a product to perform its intended mission without failure. It is usually expressed in mean time between failures (MTBF). However, since the specific product is not designed to have a long lifetime, but just to perform one mission, the a long term detailed analysis is not achievable. The reliability of the helicopter is assumed to have a direct dependence on the the one of the different subsystems. For each of them several critical failure modes and the redundancy policy to increase reliability is discussed. Critical failure modes are defined with the help of empirical analyses and the risk analysis[43, 44].

14.1.1. Propulsion and Power

- **Engine compressor failure:** Leakage and structural misalignment can lead to decrease in available power and ultimately to mission failure.
- **Wave rotor malfunction:** Since the wave rotor is designed for a different engine, incorrect installation can affect output power and fuel consumption.
- **Engine stall at low rpm:** At low turbine speeds, turboshafts have a tendency to experience compressor stall.
- **Gear failure:** Unexpected high torque or misalignment in assembly can lead to scuffing of gears and ultimately structural failure.
- **PCVT failure:** Again unexpected high torque or misalignment in assembly can lead to scuffing of gears and ultimately structural failure.
- **Fuel system failure:** Fuel pump, level sensor and pressure devices might lead to a drop in fuel flow and consequently the possibility that the engine is unable to provide enough power.
- **Electrical system failure:** Failure to generate electrical energy for the subsystems might lead to failure.

Both the gears and PCVT have been designed with a redundancy factor on the maximum torque occurring in the system. The engine compressor is a flight proven system. Redundancy in the system is too hard to design, therefore the engine will continue to be a critical failure point. The same goes for the fuel system. When the propulsion and power system should fail, a fail safe system for decoupling the drivetrain is implemented in order to allow for autorotation and safe landing. As for the electrical systems, an APU is implemented for backup.

14.1.2. Rotor

- **Blade failure:** In the occasion that the frequency of the rotor blades coincides with the one of the engine, resonance will occur, which will lead to failure of the blades.
- **Shaft bending failure:** A possible failure can occur due to bending in case that the centre of gravity of the hub is not corrected from the current one, .
- **Shaft frequency failure:** If the natural frequency of the shaft coincides with the natural frequency of any the rest of the systems, failure will occur.
- **Hub hinge failure:** Excess flapping loading could leads to failure.

Due to the fact that a Campbell diagram, with all the frequencies that should be avoided, is created, it is not expected that failure due to resonance will occur. Next to this, a simple balancing weight can provide with full stability of the hub, which will completely resolve the issue of failure due to excess stress. Furthermore, a full frequency analysis of the rotorcraft's systems needs to be performed and it should be made sure that none of the natural frequencies coincide with another one. Based on the performed analysis, overload due to excessive flapping is not expected. However, if higher loads are expected, the hinge can be designed in a way that it can cope with them.

14.1.3. Structure

- **Fuel tank material failure:** Due to the fact that the fuel tank is produced of CFRP, some porosity of the material can occur, which will lead to a leak and consequently, lower endurance performance.
- **Fuel tank strength failure:** Not all possible landing modes have been studied. Thus, in case the landing is not perfectly controlled, a buckling failure mode can occur.
- **Airframe failure:** If the natural frequency of the frame coincides with the natural frequency of any the rest of the systems, failure will occur.

In case that leakage of fuel occurs, it is possible that the interior of the tank is covered with a very thin metal layer, which will not increase the weight significantly, but at the same time will prevent from fuel losses. As mentioned before, the fuel tank is designed with a high safety factor, thus, it is not expected that full failure will occur during landing. Furthermore, the current control system shows good performance and it is expected to be able to provide with sufficient stability and control during the studied flight condition.

14.1.4. Control

- **Control surface failure:** In case of high unexpected loads, the loading on the control surfaces can exceed the maximum limit and local failure can occur.
- **Autopilot failure:** Electrical systems are typically prone to internal failure, bad connections can ultimately lead to, for example, short circuit.
- **Sensor failure:** Sensors can be wrongly calibrated or provide wrong information to the autopilot.

The chosen off-the-shelf autopilot has built in triple redundancy system for the system itself and the sensors it uses and is therefore expected to be failsafe[25]. The control surfaces are able to provide full control even when the CTEF of one blade fails, its redundancy is in the use of a CTEF on each rotor blade.

[25] URL https://www.micropilot.com/pdf/brochures/brochure-MP2x28.pdf [cited 24 January 2017]

14.2. Availability

Availability is the ability of an asset to be available when it is needed. This is a very useful concept for reusable assets. However, as this design will only be used for one specific mission, availability is not applicable to DREAM.

14.3. Maintainability

Maintainability is a characteristic of a design which determines the probability that a failed asset can be restored to its normal operable state within a given time frame. This is a very useful characteristic for assets that are used for a long time, because the maintenance strategy can be based on this characteristic. However, as DREAM is only used once, maintainability is not applicable.

14.4. Safety

Safety of an asset refers to it being protected from harm or other non-desirable outcomes. Since DREAM is autonomous, safety of humans on board is not relevant issue. Therefore, the safety analysis will be focused on the surrounding environment and spectators.

The best way to ensure the safety is quite obviously to design in such a way that failure is avoided. This is done by introduced sufficient safety factors in the design, and identifying critical failure modes with respect to the safety of the environment and spectators. One of these critical failure modes, in the event the rotorcraft fails or crashes, is the leaking of fuel from the fuel tank and a subsequent fire or explosion. This needs to be avoided at all costs, and so in the design some mitigation must be done.

Another failure mode could be that, upon impact, the rotor blades detache from the rotorblade and become flying projectiles. The failure mode of the rotor blades and hinges must be designed in such a way that the failure of these components is controlled, thus ensuring the rotor blade will dissipate its kinetic energy as fast as possible.

Furthermore, to ensure the safety with respect to its surroundings, appropriate surroundings must be chosen. The mission trajectory must be chosen such that it is safest for the surroundings and the mission success. Finally, it is very important to get permission for performing the mission from the authorities, such that they can make sure that the area is cleared.

15 NDARC Comparison

This chapter elaborates on the weight and endurance estimations done using NDARC, and comparing it to the DREAM's estimations. Firstly, the mission implemented in NDARC is defined in Section 15.1. In Section 15.2 the assumptions made in NDARC for the various subsystems are explained, along with the effects they are expected to have on the results. The results of the comparison are shown and elaborated on in Section 15.3. Lastly, conclusions and recommendations are listed in 15.4, such that a future model represents the design more accurately.

15.1. Mission analysis

The main mission modelled in NDARC consists of four phases, which are shown in Table 15.1. The first phase consists of a climb, in which the rotorcraft will ascend to the required altitude to get out of ground effect. The second phase will be the three km travel through the hover stations to the final station, where the third phase will commence: the burn, or hover, phase. Lastly, the descent is modelled in the fourth phase. The last idle is added to make sure the descent is up to the ground.

The first column in Table 15.1 represents the input variable names, which are used as a basis for iterating. As can be seen, $Vkts$ is an input, this is the speed in m/s rather than the speed in kn. Besides that, the power and fuel consumption is modelled from the Maximum Rated Power (MRP) of the engine in the climbing phase, and from the Maximum Continuous Power (MCP) for the other mission phases. This model is extended and split into more phases to deal with the proposed variable RPM. The goal was to assume continuous transmission, but since no options seem to be present to model this accurately, the hover phase is split into five parts. Each of these hover phases consumes 20% of the fuel, after which the RPM is updated for the next phase.

Table 15.1: Primary mission statement NDARC

kind	'climb'	'dist'	'burn'	'climb'	'idle'
dist	0	3	0	0	0
Vkts	0	28	0	0	0
altitude	0	50	50	50	0
rating	'MRP'	'MCP'	'MCP'	'MCP'	'idle'
set_max	2	1	0	2	0
max_quant	'Pmarg'	'range'	' '	'Pmarg'	' '
max_var	'ROC'	'speed'	' '	'ROC'	' '
max_quant(1,2)	'climb'	' '	' '	'climb'	' '
max_var(1,2)	'speed'	' '	' '	'speed'	' '
SET_tank	0	0	1	0	0
fTank	1	1	0.01	0.1	0.1
coll	1	1	1	-1	2
pitch	0	1	0	0	0
STATE_trim	'thrust'	'symm'	'free'	'thrust'	'none'

Apart from modelling the primary mission, several point operating conditions have been defined. The three main ones, which need to be validated, are the range, endurance and minimum power cruise speed.

These operating conditions are determined by stating which quantity should be maximised by iterating over which variables. For the range this means maximising the range by varying the forward flight speed, and finding the maximum flight speed over the fuel flow. The endurance is determined by trying to maximise endurance, or equivalently, $1/\dot{m}_{fuel}$. Lastly, the minimum power required is determined by determining the minimum power setting by varying the forward flight speed.

15.2. Assumptions

In this section the assumptions used in modeling the various subsystems in NDARC are stated. Most parts are modelled with parameters as explained in their respective sections. However, some additional assumptions were required for NDARC. This is done in order to make sure NDARC can compute the various parts properly, or to better determine the difference between expectations and reality.

Propulsion

Several assumptions have been made to model the engine and drive train properly. The most important assumption done is for the modelling of the wave rotor in conjunction with the input to output relation of the SFCs in NDARC. Due to an unknown problem in the SCF model, using an input SFC of 0.58 $kg/kW-hr$ results in the required output of 0.27 $kg/kW-hr$. This is about 10% more efficient than the engine would be without wave rotor. The next assumption is that the zero power loss is 20 kW, which was estimated from the NDARC example helicopters. Furthermore, it was assumed that the drive train power limit is 800 kW. This estimation is somewhat low to conserve weight, but enough to deal with the power generated by the engine. The last assumption, which is for both the propulsion and for the rotor, entails the continuous RPM control. As stated previously, it is assumed that this can be modelled by taking discrete steps. Making this more continuous is expected to result in a higher efficiency and therefore endurance.

Rotor

In order to model the rotors, the chord and twist were assumed to be linear. The root and tip chord and angle were taken as determined by the aerodynamics department. The next assumption introduces the largest possible source of error: The rotors are assumed to have the same shape and size. This is done because modelling the bottom rotor properly with a jump in the twist the was found to result in torque issues. The drivetrain did not scale properly to take torque differences into account, and using a pedal input to counteract the torque difference is unrealistic. The rotor is also modelled with a generic hub, which is heavier than our hub design, without swashplates.

Fuselage and Fuel Tank

The fuselage and fuel tank are modelled as a single volume for lift, drag and moment coefficients. The shape modelled is similar to the designed fuselage, with a difference in the tail. NDARC seems to model at least two tail surfaces, even without a tail boom being present. This was solved by modelling the main structure, the top pyramid, with those tail surfaces. This could result in a slight overestimation of the weight, due to the fact that NDARC models a weight for the load carrying structure separately, and this introduces extra material on top of that.

15.3. Results Comparison

The results of the comparison are presented in Table 15.2. It can be seen that the weights estimated with NDARC are generally higher than the ones calculated with the model. Besides that, NDARC estimates both the hover power and power for maximum range to be 20% higher than our model. As can be expected, the endurance is therefore estimated to be lower.

Table 15.2: Results NDARC compared to own estimations

Component	NDARC	Own	% Discrepancy
Weight Components			
Electrical systems and equipment	234 kg	75 kg	68%
Hubs + Hinges rotors	286.1 kg	100 kg	65%
Fuselage + fuel tank	221 kg	102 kg	54%
Engine	484 kg	286 kg	41%
Rotorblades	330 kg	355 kg	−8%
Fuel	2858 kg	3250 kg	−14%
Drive system	534 kg	613 kg	−15%
Power			
Hover	647 kW	517 kW	20%
Max range	453 kW	361 kW	20%
Endurance	21.6 hr	25.2 hr	−17%

Weights

It can be seen that a relatively large weight offset is present in various systems. Going from positive to negative differences: The electrical systems and equipment has got the largest offset, this can mainly be attributed to the controls. From NDARC the flight controls are estimated to be 147 kg, whereas in our design the weight for the conventional control mechanisms, such as collective and pedals, is zero. This is replaced by some weight for the continuous trailing edge flaps and an electrical generator.

Next up are the hubs and hinges. NDARC uses swashplates for the hubs, but since it was decided to not use swashplates, part of the weight difference can be explained. The estimated difference because of this is estimated to be about 100 kg. The remainder of the difference can be explained by the connections in the assembly.

The difference in estimations of the fuselage and fuel tanks can be attributed to two parts. Firstly, our structure is designed as lightweight as possible, not taking into account safety factors one would require with a pilot on board. Secondly, it is assumed the fuselage can be attached with weightless glue, whereas in real life bolts, rivets and similar connections would need to be used, yielding an increased weight.

The engine in our design takes into account the engine with minimal supports, attachments and accessories. From NDARC, on the other hand, a weighty engine cowling is added. This cowling is estimated to be around 245 kg. This is not designed in our case due to the lack of required protection, and already having a fuselage with a similar function.

The weights of the drive system and rotor blades are estimated fairly accurately. For the rotor blades a note is required: the blades in our design are weighted at the tips to decrease the tip deflection, whereas the NDARC model uses continuous weight of the blades along the radius.

Lastly the weight of the fuel is deduced from the initial weight and the weight of all systems. Therefore the offset in fuel represents the offset in weight estimations for the various systems.

Power and Endurance

As stated, Table 15.2 shows that the hover and maximum range powers are estimated to be higher than the ones in our calculations. A possible explanation for this would be the higher level of rotor optimisation present in our design. NDARC assumes a collective to deal with the way the trailing edge flaps operate, this results in an overestimation of the drag, and therefore power needed from the blades. The endurance is estimated to be 17% lower mainly because of those power differences. The difference in weight of the various subsystems also has an influence on the endurance. For the same initial weight, about 1.5 $hours$ worth of extra fuel is available in our design.

15.4. NDARC Conclusion and Recommendations

Firstly the conclusions of the comparison is shown, after which recommendations are provided to improve the accuracy of the comparison with NDARC

Conclusion

The NDARC model used consists mainly of components used in current rotorcraft. Therefore the comparison presented mainly represents the difference between current state-of-the-art and the DREAM. It can be seen that the expected decrease in power usage is in the order of 20%, and similarly, that the increase in endurance is in the order of 20%.

Recommendations

Since there was too little prior knowledge of NDARC present to model the DREAM accurately, some recommendations can be made on how to improve the model. Most of these recommendations come from the fact that NDARC expects certain inputs, like for example a tail, which are not present in our design.

Firstly, the two rotors should be modelled separately with non-linear twist and chord distributions, rather than having them be identical. The tail surfaces, tail and landing gear should be fully removed. The landing gear did not have any weight in the current model, but it is still coded in. Since the SFC of the engine is currently changed from input to output, a further analysis on this issue is required. This might be improved by increasing the accuracy of the air intake, and the RPM ratios for various power settings. Also, the collective, pitch and pedal inputs should be replaced by a model of the CTEFs. This would result in obtaining more accurate weights of the control system. Lastly, the model should incorporate the continuously variable transmission, instead of having step changes in the RPM of the rotor, resulting in a more accurate representation of power required during the entirety of the hover phase.

16 Design and Development

During the last nine weeks, the Hover Team has designed a coaxial rotorcraft that can hover for 25 *hours*. However, in order to be able to participate in the challenge, the rotorcraft has to be designed in further detail on the subsystem and part level. Furthermore, the rotorcraft has to be tested and certified, and the subsystems have to be produced and assembled. This chapter gives an overview of the parts and planning of these post-DSE activities.

Section 16.1 discussed the project design and development logic, which is followed by the production plan, presented in Section 16.2. The Gantt chart for the processes after the end of the DSE is illustrated in Section 16.3. Lastly, the cost of the complete design is estimated and discussed in Section 16.4.

16.1. Design and Development Logic

The project design and development logic displays the order of the activities in the post-DSE phase and can be seen in Figure 16.1. A more detailed planning of the post-DSE activities can be found in Section 16.3.

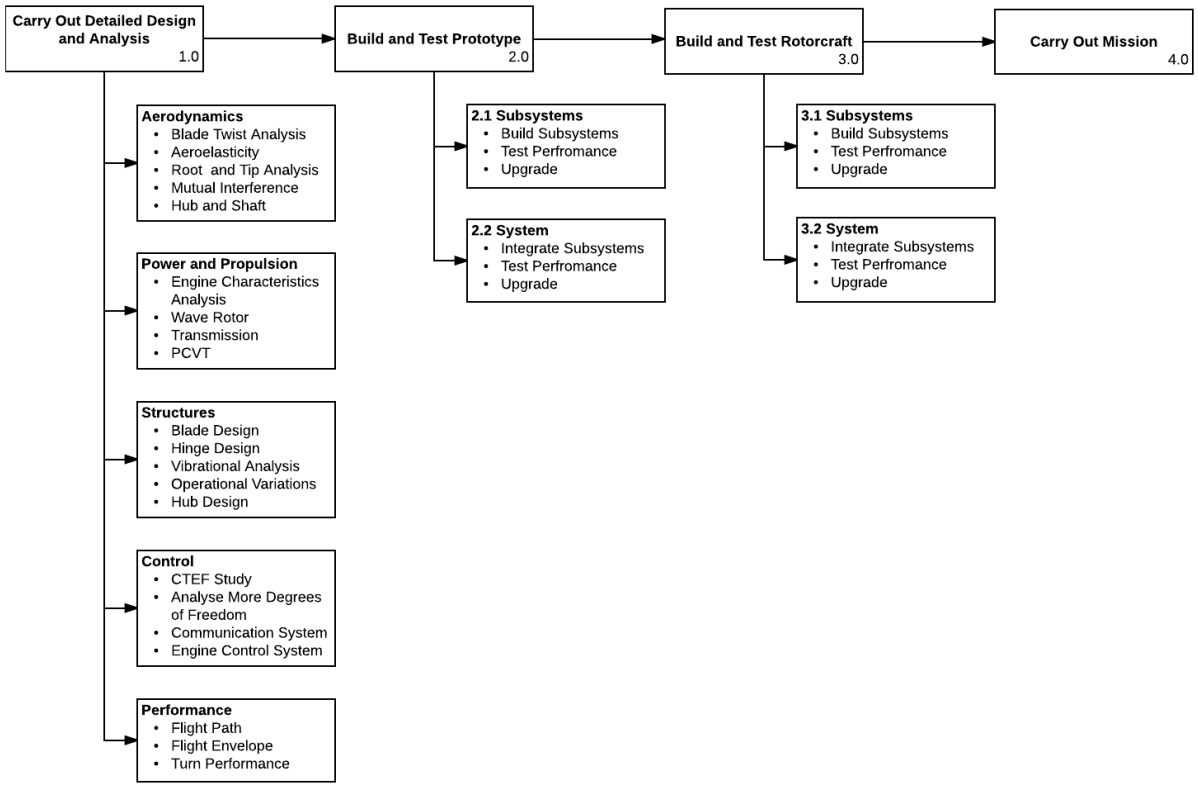

Figure 16.1: Project design and development logic

Detailed design and analysis
The first step is to carry out the detailed design and analysis of the rotorcraft. It can be noted that each of the subsystems need further more in-depth analysis. Those can be performed simultaneously, thus no numbering of the sublevel process has been given. More specific guidance to the detailed design are given in the recommendations of each system as well as the final recommendations, which can be found in Chapter 19.

Build and test prototype
In the current case, prototype is meant as a small scale model of the actual rotorcraft. It should be noted that, due to the fact that there are very few if any aircraft like the designed one, a prototype is considered a very valuable feature, which will allow for on-time and cheaper modifications, if those are needed. Firstly, based on the detailed design, the subsystems of this prototype need to be build and tested. If required, they can be upgraded in order to meet the specific technical requirements. This is followed by building and testing the complete prototype system, which will help in determining whether the different components are compatible or any adjustment in dimensions and functions is required. Testing it will provide with a relevant performance estimate. If needed, the design can be upgraded before moving to the following stage.

Build and test rotorcraft
This stage is very similar to the one of the prototype. However, this time the machine itself is build and tested in full scale. Final upgrading might be required before the last stage.

Carry out mission The specific mission is presented by the AHS and is discussed in Section 4.2. As the rotorcraft is expected to fly only once for the competition, no follow-up processes are scheduled. However, if the project is extended, further design and optimisation can be carried out, which will contribute to better performance.

16.2. Production Plan

In the current section the production plan of the complete design is going to be discussed.

Firstly, as discussed in Section 8.5, the different parts of the structure are produced from specific materials and using the corresponding methods, which would result in the best performance of the element. Due to the simplicity of the components of the airframe and the shaft and drive system, they can be bought off-the-shelf, keeping in mind the recommended production techniques, as already discussed. For example, there are pultruded carbon fiber tubes with an adequate diameter and length existent, with an expected delivery time of a week[26]. Furthermore, the steel shafts can be also ordered and the delivery time is the same[27]. Furthermore, for the top and bottom hubs a schedule for the casting needs to be taken into consideration. A period of about a week is the expected required time. However, due to the highly specific geometry and properties requirements for the blades and fuel tank, they will need to be produced specifically for the mission. Based on engineering experience, the duration of this is expected to be two to three months, which would include preparing the moulds and the actual manufacturing.

For the production of the transmission shafts, the same production procedures count as for the rotor shaft. However, due to the large size of the bevel gears, that they cannot be bought off-the-shelf, they have to be custom made. For the production of the gears, the following steps are taken. First, the materials are cut to size. Then, the cut workpiece is shaped into a gear blank, after which the gears are cut with a Coniflex generator. Finally, the gears are deburred and finished[28]. This process will take not more than two days. The PCVT components are simple face gears that are machined to its dimensions and geometry. The teeth on the face gears are produced with the process of hobbing. The

[26] URL https://goodwinds.com/carbon/pultruded-tubes.html [cited 24 January 17]
[27] URL http://www.steeltubedirect.co.uk/product_selector.aspx?category=100002&shape=150 [cited 24 January 17]
[28] URL http://khkgears.net/gear-knowledge/introduction-to-gears/production-processes-bevel-gear/ [cited 24 January 2017]

ball bearings however can be more complex and time consuming, where the metals are heat treated first. The ball bearings consist of an inner and outer race and a cage to support the balls[29]. These components are assembled in a discrete manner, to produce the PCVT which is then set into a housing unit. The estimated production time would be between one and two months.

Regarding the control system, as the technology is currently in development, but is expected to be available within 5 years, as discussed in Chapter 9, it is difficult to make an estimation on the production plan and required manufacturing time. However, as this can be done simultaneously with the blades production and only a few days for the installation are expected to be needed, a period of one additional week might be required.

In conclusion, in total half an year to an year would be required for the production of the rotorcraft, which will include the preparation, manufacturing of the components and their assembly. Based on engineering experience, it has been observed that a certain time margin for logistics issues, such as delivery delays, mismatching sizes and others, is required. Thus, even though the longest estimated duration is three months, which is required for the blades and fuel tank production, and most of the processes can be done simultaneously, a period of at least half an year would be required.

16.3. Project Gantt Chart

In Section 16.1, the project design and development logic was displayed. In this section, that logic is going to be made more profound in the project Gantt chart. In this Gantt chart, the different post-DSE activities are scheduled. These activities are divided in four phases.

The first phase is the final design phase, in which more detailed design of DREAM is completed. The second phase is called the prototype phase, in which the final design is evaluated and the prototype is built and tested. In the production and testing phase, the real DREAM is built and tested. In the final phase the mission trajectory is chosen and certified and the mission is performed. This phase ends with the analysis of the mission, which ends the post-DSE phase.

The post-DSE Gantt chart is displayed in two parts. The first includes the detailed design phase and the prototype phase, where the prototype will be a small scale model of DREAM, and is displayed in Figure 16.2. The second part includes the production and testing phase and the mission phase. This part is given in Figure 16.3.

Name	Begin date	End date
Detailed Design Phase	1/24/17	4/4/17
Detailed Structural Design	1/24/17	3/1/17
Detailed Blade Design	1/24/17	3/1/17
Detailed Control System Design	1/24/17	3/1/17
Detailed Propulsion System Design	1/24/17	3/1/17
Part Design	2/21/17	3/21/17
Analyse Final Design	3/22/17	4/4/17
Prototype Phase	4/5/17	4/19/17
Produce Prototype	4/5/17	4/7/17
Test Prototype	4/10/17	4/19/17
Windtunnel Testing	4/10/17	4/14/17
Structural Testing	4/17/17	4/19/17

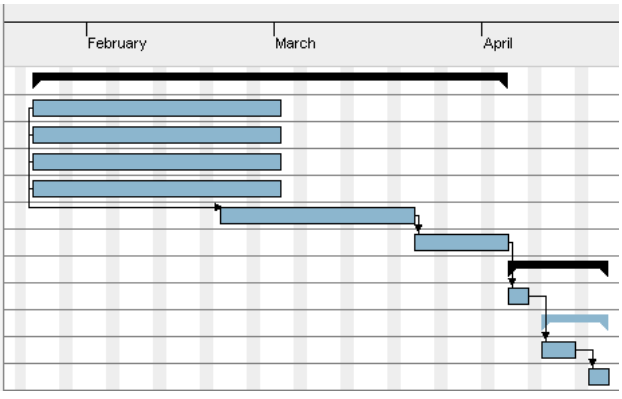

Figure 16.2: Project Gantt chart of final design phase and prototype

[29] URL http://www.madehow.com/Volume-1/Ball-Bearing.html [cited 24 January 2017]

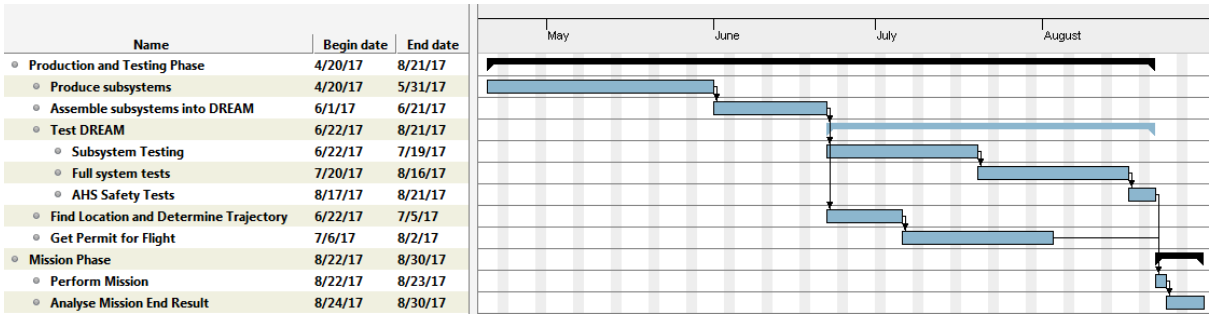

Figure 16.3: Project Gantt chart of production, testing and mission

16.4. Cost Breakdown Structure

In the current section, the overall cost of the design will be discussed. The breakdown of the complete budget is presented in Figure 16.4.

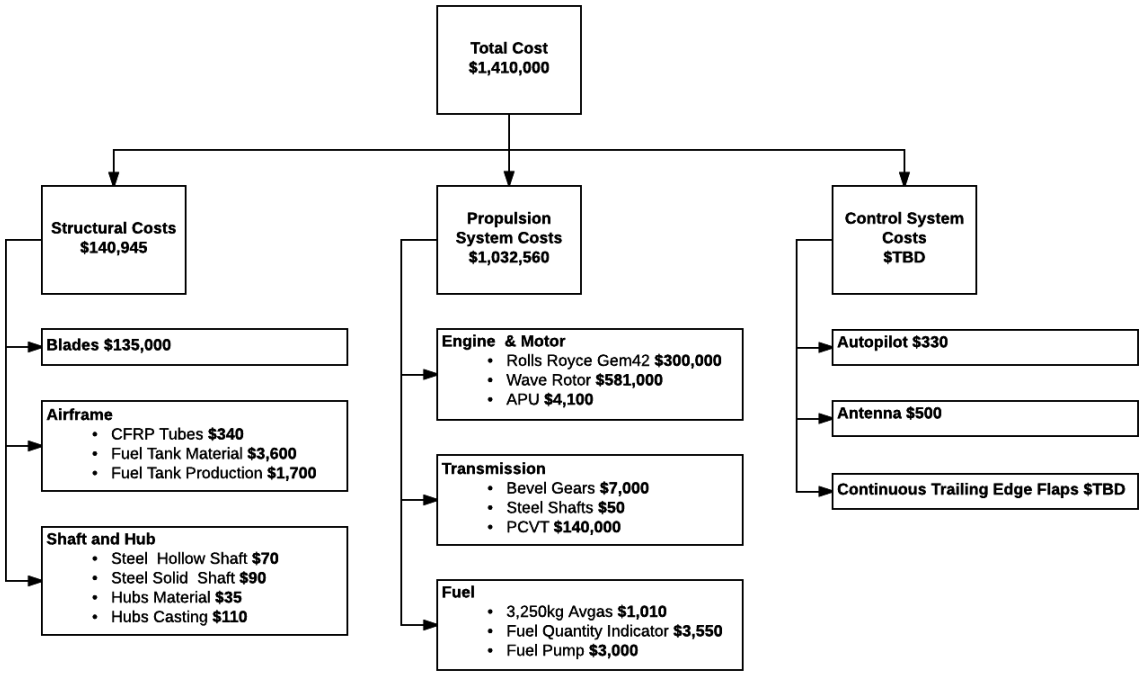

Figure 16.4: Cost breakdown

The budget is divided in three main groups: the ones of the structure, the propulsion system and the control system.

The structural costs account for the production and manufacturing of the blades. The exact price is estimated by the help of the spare parts price list provided by Enstrom[45]. A blade price of $\$13,500$ was provided. For the ten blades present, this resulted in a total cost of $\$135,000$. Next to this, the airframe cost consists of the CFRP tubes and the cost of the fuel tank material and manufacturing. Accurate CFRP tubes for the airframe were found and can be bought of the shelf[30]. A total amount of 8 is needed,

[30] URL https://www.rockwestcomposites.com/round-tubing/round-carbon-fiber-tubing [cited 24 January 17]

thus their total price sums up to \$340. Additionally, a prediction on the carbon fiber reinforced polymer material and its production for 2020 was found which lead to the estimated total cost of the fuel tank to be $\$5,300$. Furthermore, the price of the steel shafts has also been estimated as the one of steel tubes found on the market[31]. The price of the hubs' material and manufacturing has also been estimated using methods explained by producers[32].

The cost of the propulsion system include the engine price, which is taken of the shelf. However, it should be noted that, due to the fact that the implemented engine is meant for military services, the price of a similar engine has been taken into account[33]. The wave rotor is the most expensive system and its cost is provided in the report by Philip Snyder[6]. Bevel gears' price was based on their sizes and material[34]. Their total price is estimated to be $\$7,000$. The fuel quantity indicator and APU systems are also taken from the spare price list mentioned before[45]. The price of steel shafts for the transmission is estimated the same manner as the ones for the shaft. Last but not least, the fuel price per liter was provided by IATA[35].

The control system cost was hard to be determined due to the fact that the continuous trailing edge flaps technology is currently in development and, even though it is expected to be developed within the time mentioned, no cost information is present yet.

Together with the autopilot and antenna price, the total budget was calculated to be $\$1,178,485$. However, due to high uncertainty, a 20% margin was implemented, which leads to the final budget of $\$1,410,000$. It can be noted that this is much higher than the one presented in the Midterm report[5]. This is due to the low detail of the past estimation and of the uncertainty of the design at that design point. However, as cost is not considered an issue in the current design, the budget is evaluated as acceptable for the high technical improvements that are demonstrated.

[31] URL https://www.alibaba.com/showroom/aisi-1045-steel-price.html [cited 24 January 17]
[32] URL http://www.iron-foundry.com/cast-steel-prices-lb-kg-ton.html [cited 24 January 2017]
[33] URL http://www.fi-powerweb.com/Engine/Rolls-Royce-M250.html [cited 24 January 2017]
[34] URL http://khkgears.net/product-category/bevel-gears/ [cited 24 January 17]
[35] URL http://www.iata.org/publications/economics/fuel-monitor/Pages/price-analysis.aspx [cited 24 January 2017]

17 Sustainability

This chapter summarises the sustainability of the various parts design and will divide the separate aspects in either energy efficiency or acoustic signature reduction. Those are the main sustainable aspects achieved in the design of the rotorcraft.

Energy Efficiency

Energy efficiency is one of the main focus points and design drivers since the predominant mission requirement is the hovering for 24 hours. In other words, an improvement in endurance and the current state of the art technology needs to be achieved. One way to significantly improve endurance is to increase rotorcraft efficiency, especially with an efficient use of energy, which can be scaled under sustainable design aspects.

It is realised that burning fossil fuels to stay in one place in the air is hardly sustainable. Therefore, pushing the boundaries of energy efficiency for helicopters will be necessary for it to be considered even slightly sustainable. Since an increased efficiency of multiple systems is required to meet the endurance requirement, several options have been explored and discussed.

Firstly the propulsion group: As stated in Section 6.1.1, the engine uses a wave rotor to improve the specific fuel consumption. Besides that, a pericyclic continuously variable transmission is used for RPM control, as explained in Subsection 6.2.2 and Section 7.5. The aerodynamics group designed efficient blades to deal with hover for varying RPM, as elaborated on in Section 7.4. Lastly, the control system implements the continuous trailing edge flaps as shown in Section 9.5.1. These flaps are able to reduce the generated vibrations and noise, thus preventing energy loss and increasing the rotor efficiency.

Acoustic Signature Reduction

Another means of improving the sustainability of the design is taking into account the acoustic signature. Helicopters are prone to a high noise production and can have a huge impact on the environment.

As mentioned in Section 11.5 the rotorcraft achieves a significant reduction in acoustic signature. First of all the innovative control system, CTEFs, as presented in Section 9.5.1 are able to provide full controllability with as main advantage a reduction in produced vibration and noise. Furthermore the specific flight mission eliminated the need for certain more complex manoeuvres that are known to generate the most annoying frequencies and highest amplitudes.

18 Conclusion

The current report presented the overall layout of the rotorcraft designed for the challenge posed by the AHS for a 24 hour hovering device. In order to achieve this, the team has aimed for an optimal design of each subsystem.

The propulsion subsystem consists of two parts: the engine, which is a Rolls-Royce GEM 42-1 Mk.204, and the drivetrain, which transfers power and rotation from the engine to the rotors. The engine provides enough power to sustain hover and extra power to accommodate take-off. To this engine, the novel concept of a wave rotor is added, which decreases the specific fuel consumption of the engine. The transmission consists of miter gears and the novel concept of a Pericyclic Continuously Variable Transmission, or PCVT, which makes sure that DREAM's rotors can operate at a variable RPM range.

The rotor configuration and blade design are optimal for high endurance hovering. Being able to focus on hovering, without having to compromise for forward flight capabilities, allowed for specific rotor characteristics. These include a high rotor radius, nearly ideal taper for the upper rotor and nearly ideal twist for both rotors. The amount of five blades per disk was chosen in order to be able to approximate this ideal geometry as closely as possible.

In order to optimise the weight and at the same time to be able to carry the loads, the airframe was decided to be represented by simple truss structure, which is attached to the fuel tank. The latter is designed in such a way that it can support the landing loading, thus no dedicated landing gear is required. Next to this, the design of the hub and shaft have been performed in such a way that they can carry the maximum produced torque of the engine and the weight and centrifugal forces of the blades.

The DREAM's control system is capable of changing the rotorcraft's vertical postion and altitude. The rotor blades are equipped with continuous trailing edge flaps, which serve both as control surfaces and tools for blade noise reduction. The CTEFs can apply collective (force) and cyclic (moment) control inputs. They span from around 70% of the rotor radius to 97%. All devices are controlled by a triply redundant autopilot unit. This unit is equipped with various sensors and control software. Information about the helicopter is constantly communicated to the AHS's certified reference point, as well as a ground station. Because the helicopter is unstable in the absence of control inputs, the CTEFs provide active stabilisation. The control system is capable of stabilising the aircraft, as well as climbing/descending short distances, and applying attitude changes.

The performance of the rotorcraft is divided into hover and forward flight. It was shown that with an optimal flight speed derived from the power curve the forward flight mission segment is significantly small when compared to the hover section. With a decreasing required power to hover during the mission and optimal RPM settings for the rotorcraft weight the final hover endurance was calculated to be 25.3 hr.

19 Recommendations

The current chapter presents the recommendations for further analysis and improvement of the design. Each subsystem will be discussed, starting with recommendations on the power and propulsion system discussed in Section 19.1. This is followed by recommendations on further aerodynamic and structural analysis, discussed in Sections 19.2 and 19.3, respectively. Finally, the stability and control recommendations are listed in Section 19.4

19.1. Power and Propulsion

There are a few recommendations for the powertrain design.

Engine Characteristics

The characteristics of the engine were modelled numerically where results were verified with another program. However, the simulation results can significantly vary from the actual scenario. It would be ideal to have experimental data from the chosen engine to model its characteristics better. It would also provide the valuable information of when the engine stalls.

Wave Rotor Redesign

The current wave rotor is optimised for a different engine. With more time and an understanding of CFD modelling, it would be possible to redesign and optimise the wave rotor for any given engine. This would provide better information on the actual effects of the addition of the wave rotor.

Engine Type

The current power system uses a single turboshaft engine. It could be beneficial if a hybrid power unit using a piston engine and electric motors are implemented. Due to the lower specific fuel consumption of piston engines at lower powers, the endurance could be improved. Unfortunately the power to weight ratios of current piston engines are not feasible enough for it to be implemented in this design.

Fuel Choice

Hydrogen is a promising fuel source for the future. Until major advancements are made on the storage capabilities of hydrogen, conventional fuel sources provide the best choice for the current requirements. Hydrogen has high specific energy and only water is produced as emmissions, which can provide a sustainable option.

Transmission Design

The transmission is currently designed using steel. The use of titanium alloys were considered, but were deemed to have a poor rating for wear and tear. If titanium is used however, this could further reduce the transmission weight of the system and improve performance.

PCVT

The PCVT is an innovative design for continuously variable transmission. The feasibility and application of this technology is yet to be realised on rotorcraft. Extensive testing and data gained from these tests can provide information on the limitations and will aid the overall design of the PCVT.

Bevel Gear Design

Straight bevel gears are used for the transmission system currently. This was done for the sake of simplified calculations and a lack of time. It would be ideal to use spiral or zero bevel gears as they can be less noisy and more efficient.

Bevel Gear Mass

The mass of the bevel gears was calculated using a simplified volume equation. However, the real volume of a bevel gear would be smaller. By using a more extensive equation for gear volume would lead to a more realistic gear mass.

19.2. Aerodynamics

The aerodynamic design done is still preliminary. Models used are greatly simplified and many aerodynamic effects are not yet taken into account. A list of recommended analyses is covered here.

Blade Twist

The upper and lower rotor blade have a unconventional blade twist. The lower rotor has a blade twist that significantly changes at $R = 5.66\ m$, this is due to a rapid change in induced velocity. A better analysis should be performed on the effects of sudden blade twist. Little is known about such rapid changes in blade geometry.

Aeroelasticity

The interference between structural deformation due to aerodynamic forces, which may lead to oscillatory motion, should be researched. The first harmonics in blade flapping were determined, however a complete analysis for higher harmonics and other modes should be researched. Other modes may be lead/lag and torsional motion. These aerodynamic oscillations may lead to loss in aerodynamic thrust or gain in power required due to increasing drag. Also variation in pressure distribution due to aeroelasticity might lead to pitch or rolling moment. Advanced structure fluid interaction models should be used to analyse these effects, this is outside the scope of this research however strongly recommended.

Root Loss

Similar to the tip of the rotor blade, at the root the lift distribution will tend to zero since there will not be a pressure difference achievable. More advanced analysis methods should be done to cover this effect, as explained below. Since at the root in general velocity is low, the thrust there is lower such that this effect is not too relevant for the preliminary design.

Root Cutout

The size of the root cutout for aerodynamic purpose is quite arbitrarily. More advanced models should be used to analyse the effects of larger or smaller root cutouts. Effects of rotor blades close to each other, i.e. a locally high solidity ratio, is assumed to lead to lower aerodynamic efficiency. To find an optimal root cutout these sizing parameters should be taken into account.

Tip Design

The rotor blade tip loss is taken into account using the Prandtl tip loss factor. However, a more extensive analysis on the tip design should be done. For example, different high mach number airfoils might be used. Also the British Experimental Rotor Program (BERP) blade design may be looked into[17].

Mutual Interference

The spacing between the two rotor disks was assumed to be such that the lower rotor is in the developed wake of the upper rotor. This was however, based on visualisation experiments. It is recommended to perform a better wake analysis of the contra-rotating rotors. The interference effects of the upper rotor disk on the lower disk are taken into account with a simplified model, however the reverse is not modelled. It is recommended that this effect is taken into account, using the more advanced models discussed below. From this a better vertical separation distance between the two rotors can be determined.

Hub Aerodynamics

The rotor hub will have a small hover power contribution due to the drag of the rotating mechanism. The aerodynamic power loss of this subsystem should be further analysed.

Shaft Aerodynamics
The rather large rotor shaft may have a high drag in forward flight which should be analysed. Also the shaft may create a side force and moment due to the Magnus effect. This is however assumed quite small since the low rotational velocity.

Advanced Models
To model several discussed aerodynamic properties of a rotor, more advanced models are necessary. root cutout losses, separation distance, wake velocity, mutual rotor interference and more extended tip loss analysis can not be modelled with the current employed blade element momentum theory. A more advanced mathematical framework to approximate the fluid flow such as Lifting Line method, Panel method and Control Volume Finite Element method is recommended. Lifting line is thought to be the first choice still for preliminary design considerations. Leads to relative fast computations and is more accurate then BEMT[14]. Secondly, the Panel method is recommended to get a more accurate model of the fluid modelled as potential flow. Were CVFEM is recommended as a final theoretical analysis tool to model non potential flows, with turbulence and compressibility effects.

2D Airfoil Characteristics
To simplify the analysis the 2d lift and drag coefficient needed are taken for an average operational Reynolds and Mach number. In further analysis with BEMT it is recommended to use data varying for Reynolds an Mach number. The aerodynamic data used is created with Xfoil which uses the Panel method to solve a potential flow problem using discretized 2D airfoil as boundary condition. Since this is a numerical method it is recommended to experimentally verify this.

19.3. Structures

For the structural design, several design recommendations regarding the blade design as well as the airframe, the hub and the shaft can be made.

Blade Design
For the blade structural design, the blade dimensions were taken from the aerodynamics department and simplified for the MATLAB model. This MATLAB model therefore has some uncertainty. Because the blade model could not be recreated in the Fusion360 software, this uncertainty could not be determined. For further design steps, this uncertainty needs to be determined, and the design adapted accordingly.

Blade Twist
For the structural design of the blade, at first, the assumption was made that small twist would not affect the structural capabilities of the structural member. However, the blade twist increased to a maximum of 45^o. This blade twist could no longer be implemented into the structural design at that stage of the DSE. For a more accurate design of the blade structure this twist should be taken into account and adjust the structure accordingly.

Hinge Design
The hinges for the blade attachment to the root were only conceptually designed to allow flapping and lead/lag motion. The further hinge design should encompass the rotational spring incorporated into the hinge to dampen the flapping motion, and the downwards deflection limit for the rotor blades when stationary on the ground. Also, it is understood that a lead/lag damper is necessary to dampen the lead/lag vibrations. The RPMs at which these resonance vibrations occur are avoided. However, further investigation to this damping coefficient would provide useful information. Last, but definitely not least, the hinges thicknesses should be further designed to withstand the lift and centrifugal forces transferred through the blade to the hub.

Vibration Analysis of Complete System
Besides the vibration modes of the structure depend on many different factor, such as the varying engine RPM, the APU, RPM and the vibrations transferred from the hub, the coupled analysis for these

vibrations is complicated and was considered outside the scope of the DSE. The current approach is to insert heavy damping coefficient attachments, to avoid resonance. This approach could benefit from further research, to obtain good results and thus a more reliable result.

Ground Effect

When the rotorcraft operates while still on the ground, unbalance in the rotor disk could induce tilting motion in the rotorcraft. When the the lower part of the fuselage touches the ground, the loads induced by this could worsen the unbalance in the rotor disk and increase this vibration. For the current design, this principle is understood, but not yet investigated. Since the start-up phase of the mission might take some time, further investigation could benefit the mission success to avoid such situations.

Landing under an Angle

For the current fuel tank and landing system combination, the design was based on landing at zero incidence angle with the ground. It was realised that this approach is not very realistic, and so high safety factor were taken into account. However, time did permit the hover team to go into further detail. The design would obtain higher reliability values if this part of the design is further researched.

Hub Design

In order to optimise the hub design and at the same time accommodate all the five blades of the each rotors, it was decided that a star cross section would be optimal. However, due to asymmetry, a small offset of the centre of gravity is present. Even though it has been shown that the design can cope with the highest expected loads, it is highly recommended that a balancing weight is added to the design in order to reduce the additional imposed stress.

Hub and Shaft Vibrations

Due to the limited available time and the complexity of the problem, a vibrational analysis of the hub and shaft has not been performed. For further development, it is recommended that such is performed in detail.

19.4. Control

For the control system, two recommendations regarding the CTEFs and overall control analysis are made.

CTEF Study

Continuous trailing edge flaps are a new technology which has not yet matured. It is recommended that these devices are carefully studied and developed in the future. It may be necessary to redesign the rotorblade's airfoil such that it can produce sufficient lift.

More Comprehensive Analysis

The stability and control analyses should be extended to a system with more degrees of freedom, as well as applied to forward flight conditions. Furthermore, the communication- and engine control systems have to be designed in detail.

19.5. Performance

The performance analysis is still relatively preliminary and does not cover the full scope that can be covered, the following recommendations are made.

Efficient Flight Path

First of all, even though the forward flight section of the mission is significantly smaller than the hover segment, it can still be optimised. Further investigation in an optimal flight path, for example flying in

ground effect, could increase overall endurance.

More Extensive Analysis

The performance analysis has been focused on the specific mission and is in a sense quite limited. A more comprehensive analysis could be done, including the rotorcraft's flight envelope and turn performance. This might help in defining other missions where the innovative technology and design can be used.

A Mission Requirements

Code	Description
Technical Requirements	
[**REQ-TL**]	The rotorcraft shall be able to take off and land.
[**REQ-TL-1**]	The rotorcraft shall be able to change its lift by at least $< tbd >$ N/s.
[**REQ-TL-1.1**]	The rotorcraft shall be able to adjust the blade pitch by $< tbd >$ rad/ s.
[**REQ-TL-1.2**]	The rotorcraft shall be able to manage the rotational speed of the blades by $< tbd >$ rad/s.
[**REQ-TL-2**]	The rotorcraft shall be able to ascend to hover at an altitude of at least $< tbd >$ m.
[**AC-3**]	The rotorcraft shall be able to determine its position in three dimensions.
[**AC-3.1**]	The rotorcraft shall have a Position Sensor with an accuracy of less than 1 m.
[**AC-4.2**]	The rotorcraft shall have an Airspeed Sensor calibrated with a range of 0 to 20 m/s.
[**AC-4.3**]	The rotorcraft shall have an Airspeed Sensor with an accuracy of less than 1 m/s.
[**REQ-TL-3**]	The rotorcraft shall be able to handle acceleration forces of at most $1.5g$
[**REQ-HOV-1**]	The rotorcraft shall hover for at least $< tbd >$ hours.
[**MS-5**]	During hover, the rotorcraft shall operate out of ground effect.
[**MS-5.1**]	The rotorcraft shall hover at an altitude of at least 3 times its largest dimension.
[**MS-5.1.1**]	The rotorcraft shall be able to determine its altitude with an accuracy of 1 m.
[**MS-5.1.2**]	The rotorcraft shall be able to adjust altitude by a change in lift force of $< tbd >$ N.
[**REQ-HOV-2**]	The rotorcraft shall hover inside the defined hover stations.
[**REQ-HOV-2.1**]	The hover station volume shall be a 20 m radius sphere.
[**AC-3.2**]	The rotorcraft shall have a live telemetry system with latency of less than 1s.
[**AC-1**]	The rotorcraft shall be able to carry a payload.
[**AC-1.1**]	The payload shall not be lighter than 80 kg.
[**AC-1.2**]	The payload shall be non-productive.
[**AC-1.2.1**]	The payload shall not create lift.
[**AC-1.2.2**]	The payload shall not control the aircraft.
[**AC-1.2.3**]	The payload shall not provide any structural support.
[**AC-1.3**]	The payload shall be contained within a single, simple and continuous volume of space within the aircraft.
[**AC-5**]	The aircraft shall be unoccupied.
[**AC-5.1**]	The machine shall be able to fly autonomous.
[**AC-5.2**]	The machine shall be controllable from a ground station.
[**REQ-OP-2**]	The structure shall be able to sustain the $< tbd >$ [Hz] frequency oscillations induced by the rotor(s)'s motion.
[**REQ-TBS**]	The rotorcraft shall be able to travel between the three hover stations.
[**MS-3**]	The three hover stations shall be no less than 1 km apart.
[**REQ-TBS-2**]	The rotorcraft shall be controllable around its three body axes.
[**REQ-TBS-2.2.1**]	The rotorcraft shall measure pitch attitude with an accuracy of $< tbd >$ degrees.
[**REQ-TBS-2.2.2**]	The rotorcraft shall measure roll attitude with an accuracy of $< tbd >$ degrees.
[**REQ-TBS-2.2.3**]	The rotorcraft shall measure yaw attitude with an accuracy of $< tbd >$ degrees.
[**REQ-TBS-2.3.1**]	The rotorcraft shall be able to change pitch attitude with $< tbd >$ rad/s.
[**REQ-TBS-2.2.2**]	The rotorcraft shall be able to change roll attitude with $< tbd >$ rad/s.
[**REQ-TBS-2.2.3**]	The rotorcraft shall be able to change yaw attitude with $< tbd >$ rad/s.
Constraints	
[**REQ-SS**]	The rotorcraft shall be self-sustaining.
[**REQ-SS.1**]	The rotorcraft shall not collect energy from an external man-made source.
[**REQ-HA**]	The rotorcraft shall be heavier than air.

[**AC-7**]	The aircraft shall not trap gasses that have a density lower than ambient air.
[**AC-8**]	Aircraft's cavities shall be vented to the atmosphere.
[**AC-2**]	The rotorcraft shall be developed within 3-5 years.
[**AC-2.1**]	The rotorcraft shall be designed within 10 weeks.
[**AC-2.2**]	The rotorcraft shall be designed by 11 students.
[**AC-2.3**]	The design shall be able to be built within 3-5 years.
[**AC-2.4**]	The design shall be able to be tested within 3-5 years.
[**AC-9**]	No parts of the aircraft shall be jettisoned during the flight.

It should be noted that some of the requirements need some clarification.

[**REQ-TL-1**] has been changed. Instead, a minimum climb rate has been determined. In accordance with ADS33[39] this needs to be at least 0.5 rad/s.

[**REQ-TL-1.1**] has been removed. Due to the presence of continuous trailing edges flaps, no blade pitch is required in order to achieve the rotorcraft's control.

[**REQ-TL-2**] has been defined. The corresponding hover altitude is 48 m.

[**REQ-TL-3**] has been changed in order to account for accelerations during landing. The correct formulation is: "The rotorcraft shall be able to handle acceleration forces of at least $1.5g$".

[**REQ-HOV-1**] has been defined. The corresponding duration is 24 $hours$.

[**MS-5.1.2**] has been removed due to the fact that it is already covered in [**REQ-TL-1**].

[**REQ-OP-2**] contains number of specific frequencies.

[**MS-3**] is not requirement on the design, thus it is removed. The corresponding requirement is contained in [**REQ-TBS**].

Bibliography

[1] DSE Group 04, *DSE - baseline report, documenting the preliminary design process,* (2016).

[2] MD Helicopters, *Spare parts, tools and publications md helicopters,* http://www.mdhelicopters.com/publications/pdf/pricelist/2003Pricebook_i2003RevA.pdf (2003).

[3] L. M. Changa, C. *et al.*, *Development of a multicopter-carried whole air sampling apparatus and its applications in environmental studies,* Chemosphere **144**, 484 (2016).

[4] American Helicopter Society, *AHS International's 24 Hour Hover Challenge,* http://www.vtol.org/challenge (2016).

[5] DSE Group 04, *DSE - midterm report, concept generation and trade-off analysis,* (2016).

[6] P. H. Snyder, *Wave Rotor Demonstrator Engine Assessment* (NASA, Indianapolis, Indiana, 1996).

[7] S. M. Jones, *Performance benefits for wave rotor-topped gas turbine engines,* 41st Turbo Expo '96 (1996).

[8] R. Kurz, *Gas turbine performance,* Proceedings of the Thirty-Fourth Turbomachinery Symposium (2005).

[9] W. Johnson, *NDARC - NASA Design and Analysis of Rotorcraft, Theoretical Basis and Architecture* (2010), https://ntrs.nasa.gov/archive/nasa/casi.ntrs.nasa.gov/20100021986.pdf.

[10] Boston Gear, *Open gearing,* https://www.bostongear.com/pdf/gear_theory.pdf [cited 20 January 2017] (2004).

[11] Z. Saribay, *Analytical Investigation of the Pericyclic Variable Speed Transmission System for Helicopter Main Gearbox*, Master's thesis, Pennsylvania State University (2009).

[12] C. Kassapoglou, *AE2135-I Structural Analysis and Design lecture slides* (2015).

[13] S.Hameer, *A Comparative Study and Application of Continuously Variable Transmission to a Single Main Rotor Heavy Lift Helicopter*, Master's thesis, Georgia Institute of Technology (2009).

[14] J. Seddon and S. Newman, *Basic Helicopter Aerodynamics*, 3rd ed. (Wiley, The Atrium, Southern Gate, Chichester, West Sussex, PO19 8SQ, United Kingdom, 2011).

[15] M. Taylor, *A balda-dust technique for air-flow visualization and its application to flow through model helicopter rotors in static thrust,* National Advisory Committee for Aeronautics (1950).

[16] J. G. Leishman and S. Ananthan, *Aerodynamic Optimization of a Coaxial Proprotor*, Phoenix, Arizona (2006).

[17] R. W. Prouty, *Helicopter Performance, Stability, and Control*, reprint ed. (Krieger Publishing Company, Malabar, Florida, 1989).

[18] J. William D. Callister, *Materials Science and Engineering*, 7th ed. (John Wiley & Sons, Inc., 1940) appendix B.

[19] G. Saunders-Smits, *Aerospace Mechanics of Materials (AE1108-II)* (2013).

[20] L. Leihon, *Structural Design of Composite Rotor Blades*, Master's thesis, Georgia Institute of Technology (2008).

[21] A. R. Bramwell, D. Balmford, and G. Done, *Bramwell's helicopter dynamics* (Butterworth-Heinemann, 2001).

[22] T. Megson, *Aircraft Structures for engineering Students*, fourth edition ed. (Elsevier, 2007) chapter 10.

[23] J. Shen, R. Thornburg, A. Kreshock, and M. Wilbur, *Design and optimisation of an aerofoil with active continuous trailing-edge flap,* The Aeronautical Journal **120**, 1468 (2016).

[24] R. P. Thornburgh, A. R. Kreshock, M. L. Wilbur, M. K. Sekula, and J. Shen, *Continuous Trailing-Edge Flaps for Primary Flight Control of a Helicopter Main Rotor*, Hampton, Virginia (2014).

[25] K. Uusitalo, *Designing in Carbon Fibre Composites*, Master's thesis, Chalmers University of Technology (2013).

[26] S. Turteltaub, *AE2135-II Vibrations lecture slides* (Faculty of Aerospace Engineering Delft University of Technology, 2015).

[27] M. F. Ashby, *Materials Selection in Mechanical Design*, third edition ed. (Elsevier, 1992) chapter 6.

[28] W. Johnson, *Rotorcraft Aeromechanics* (Cambridge University Press, New York, USA, 2013) ISBN: 978-1-107-02807-4.

[29] *Assessment of Research Needs for wind Turbine Rotor Materials Technology* (National Academies Press, 1991) p.84, Chapter 5.

[30] P. L. F. T. Henning Mainz, Berend G. van der Wall *et al.*, *Abc rotor blades: Design, manufacturing and testing,* 31th European Rotorcraft Forum (2005).

[31] J. Sinke, *Production of Aerospace Systems (AE3321-II)* (2016).

[32] T. H. van Holten and J. A. Melkert, *Helicopter Performance, Stability and Control* (2002).

[33] U. Arnold and A. Hausberg, *Development and testing of an electrical swashplate,* (ZF Luftfahrttechnik GmbH (Germany), 2013).

[34] U. Arnold, D. Fürst, T. Neuheuser, and R. Bartels, *Development of an integrated electrical swashplateless primary and individual blade control system,* in *32nd European Rotorcraft Forum (ERF 2006)*, Vol. 2 (European Rotorcraft Forum, 2006).

[35] U. Arnold, m. Müller, and P. Richter, *Theoretical and experimental prediction of individual blade control benefits,* in *23rd European Rotorcraft Forum, Dresden* (European Rotorcraft Forum, 1997).

[36] F. Wei and A. Gates, *Improvement of servo-flap rotor design parameters for helicopter performance,* in *52nd AIAA/ASME/ASCE/AHS/ASC Structures, Structural Dynamics and Materials Conference* (AIAA, 2011).

[37] A. Lemnios and R. Jones, *The servo flap - an advanced rotor control system,* in *Proceedings of AHS and NASA Ames Research Center Vertical Lift Aircraft Design Conference* (European Rotorcraft Forum, 1990).

[38] P. Jänker, F. Hermle, S. Friedl, and K. Lentner, *Advanced Piezoelectric Servo Flap System for Rotor Active Control* (Eurocopter Deutshland GmbH, 2006).

[39] B. J. Baskett, *Aeronautical Design Standard Performance Specification* (U.S. Army Aviation and Missile Command, Redstone Arsenal, Alabama, 2000).

[40] Federal Aviation Administration, Department of Transportation, *Airworthiness standards: Transport category rotorcraft, FAR29,* http://www.ecfr.gov/cgi-bin/text-idx?gp=&SID=ec35f4ea8a03be5924de59b4c02bac36&mc=true&tpl=/ecfrbrowse/Title14/14tab_02.tpl (last update 2017).

[41] A. Filippone, *Flight Performance of Fixed and Rotary Wing Aircraft*, first edition ed. (Elsevier, 2006).

[42] C. K. R.D. Janakiram, B.W. sim and F. Straub, *Blade-vortex interaction noise characteristics of a full-scale active flap rotor,* in *American Helicopter Society 65th Annual Forum, Grapevine, Texas* (American Helicopter Society, 2009).

[43] K. Waters, *Research Requirements To Improve Safety of Civil Helicopters* (NASA, 1977).

[44] J. Dougherty and L. Barret, *Research Requirements To Improve Reliability of Civil Helicopters* (NASA, 1978).

[45] Enstrom Helicopter Corporation, *Turbine Spare Parts Price List* (Enstrom, 2012).